UNIVERSITÀ DI PISA

Scuola di Dottorato in Ingegneria “Leonardo da Vinci”

Corso di Dottorato di Ricerca in
INGENERIA DELL’INFORMAZIONE

Tesi di Dottorato di Ricerca

Design and characterization of MEMS resonant structures for sensing applications

Luca Luschi

Anno 2014

UNIVERSITÀ DI PISA

Scuola di Dottorato in Ingegneria "Leonardo da Vinci"

Corso di Dottorato di Ricerca in
INGENERIA DELL'INFORMAZIONE

Tesi di Dottorato di Ricerca

Design and characterization of MEMS resonant structures for sensing applications

Autore:

Luca Luschi _______________

SSD ING-INF/01

Relatori:

Prof. Francesco Pieri __________________

Prof. Paolo Bruschi __________________

Prof. Andrea Nannini __________________

Anno 2014

Sommario

Il lavoro presentato in questa tesi riguarda il progetto e la caratterizzazione di sensori risonanti MEMS per applicazioni di tipo biomedicale, interfacciati con l'elettronica di condizionamento per mezzo di una tecnica capacitiva. I biosensori risonanti sono strutture micromeccaniche la cui frequenza di risonanza cambia in seguito all'immobilizzazione della specie biochimica d'interesse sulla loro superficie. Queste strutture stanno riscuotendo un interesse crescente negli ultimi anni, poiché lo sviluppo di dispositivi diagnostici si sta sempre più orientando verso sistemi poco costosi, portabili e semplici da usare. La caratteristica innovativa dei sensori risonanti che verranno presentati in questo lavoro è l'impiego di un pattern di fori al fine di ottenere un'elevata sensibilità. Verranno presentati due differenti tipi di risonatori: travi incastrate ad entrambi gli estremi e risonatori quadrati operanti sul modo di Lamé. Per entrambi verranno sviluppati modelli analitici per stimare l'effetto dei fori sulla frequenza di risonanza, verrà inoltre presentata una verifica di questi modelli attraverso un confronto con simulazioni ad elementi finiti. Tali modelli verranno quindi impiegati per stimare le prestazioni dei sensori, evidenziando così l'effetto migliorativo del pattern di fori. Un confronto fra i due tipi proposti mostrerà inoltre una netta superiorità dei risonatori operanti sul modo di Lamé. Per il caso dei sensori risonanti a trave, verranno inoltre presentate alcune misure preliminari sulle frequenze di risonanza, le quali sono in buon accordo sia con i modelli e le simulazioni ad elementi finiti. Infine verrà presentata una nuova struttura risonante basata su cristalli fononici, le cui caratteristiche sono promettenti in ottica di un futuro impiego come biosensore. Come primo passo verso lo sviluppo di tale dispositivo, verrà sviluppato un modello a linea di trasmissione acustica che ne descrive il comportamento.

Abstract

The work presented in this thesis concerns the design and characterization of MEMS resonant sensors for biomedical applications, interfaced with the conditioning electronics by means of a capacitive technique. Resonant biosensors are micromechanical structures whose resonance frequency changes upon immobilization of the biochemical species of interest on their surface. Such structures are earning a growing interest in the last years, as the development of diagnostic devices is moving towards affordable, portable and easy to use systems. The innovative characteristic of the resonance sensors that will be presented in this work is the use of a pattern of holes in order to obtain an high sensitivity. Two different types of resonators will be presented: clamped-clamped beams and square Lamé mode resonators. For both of them, an analytical model for the estimation of the effect of holes over the resonance frequencies will be developed, validation of these models through comparison with finite element simulations will be performed too. These models will be then employed in the estimation of the resonance sensors performances, therefore showing the beneficial effect of the holes pattern. A comparison between the two proposed types will show the clear superiority of the Lamé resonators. For the beam resonant sensors, preliminary measures of the resonance frequencies, which are in good accordance with both models and finite element simulations, will be also shown. Finally, a new resonant structure based on phononic crystals, whose characteristics are promising for a future application as a biosensor, will be presented as well. As a first step toward the development of such a device, an acoustic transmission line model, capable of describing its behavior, will be developed.

Contents

1 BioMEMS for diagnostic applications 3
1.1 BioMEMS summary 3
1.2 BioMEMS for diagnostic applications 4
1.2.1 Optical detection 4
1.2.2 Electrical detection 6
1.2.3 Mechanical detection 9
1.2.4 Comparison 12

2 Resonant biosensors: a design approach 15
2.1 Sensitivity of a perforated resonant sensors 16
2.1.1 Optimal holes design 21
2.2 Electrostatic actuation 25
2.2.1 Lumped parameters 26
2.2.2 Distributed parameters 34
2.3 Limit of detection 39
2.4 Air damping limited quality factor 47
2.4.1 Slide film damping 50
2.4.2 Squeeze film damping 51
2.4.3 Effect of holes 52

3 Resonant beam sensor 55
3.1 Analytical model for the resonance frequencies 55
3.1.1 Perforated beam equivalent parameters 58
3.1.2 Expression for the resonance frequencies 64
3.1.3 FEM validation 67
3.2 Technological processes 74
3.2.1 TRONICS 74
3.2.2 SiGe 74
3.3 Estimated resonance sensor performances 76
3.4 Measurements 80

4 Resonant Lamé sensor 87
4.1 Analytical model for the resonance frequencies 89
4.1.1 Perforated material equivalent parameters 89
4.1.2 Expression for the resonance frequencies 99
4.1.3 FEM validation 100
4.2 Designed structures 103
4.3 Estimated resonance sensor performances 105

5 Phononic crystals for sensing applications 111
5.1 Acoustic transmission line model 113
5.2 Designed structures 121
5.3 FEM validation 122

6 Conclusions 127

References 129

Introduction

In the last years considerable efforts have been spent toward the realization of medical devices for diagnostic and therapeutic applications, with special focus on affordable, portable and easy to use systems. Diagnostic and therapeutic systems that are normally available in hospitals are very effective but bulky, expensive and time-consuming. Furthermore, skilled personal is required for their use. For these reasons, they are not suited for facing the rising request of healthcare services that the growth of earth population and the aging of developed countries will demand in the next decades. The possibility of miniaturizing such devices with a bulk and low cost fabrication process, along with the development of fast and easy assay procedures, are expected to improve the life quality of many people, while avoiding health costs explosion.

Among the microfabrication technologies used toward these achievements, MEMS micromachining is surely one of the most suited and explored, thanks to its strong miniaturization, bulk fabrication and low costs. Furthermore there is the very attractive possibility of monolithic integration of sensing and therapeutic structures with dedicated electronics capable of interacting with them. This solution allows, besides miniaturization, low power consumption, high sensitivity and the possibility of multiplexing, i. e. managing various structures through the time sharing of a single electrical part. Such a synergy between biomedical applications and MEMS technologies is testified by an extraordinary explosion of research works on this topic in the last years, which have been regrouped under the acronym of BioMEMS.

In this work, the design and characterization of high-sensitive BioMEMS for diagnostic applications is investigated, with focus on resonant sensors coupled with the conditioning electronics through capacitive readout. The sensing paradigm based on the resonance frequency shift upon immobilization of the entities to be sensed onto the resonator surface, is a commonly used technique in macroscopic structures such as Quartz Crystal Microbalances (QCM), and has been successfully transferred in the BioMEMS world, where is one of the most explored sensing strategies. Due to its fabrication simplicity and straightforward modeling, the sensor coupling through capacitive gaps (also called capacitive or electrostatic actuation) is a well established and extensively used technique.

The innovative part guiding all this thesis regards the development of a design strategy capable of raising the device sensitivity, based on drawing a pattern of holes on the structure. These holes are expected to provide an higher surface for analyte binding, thus increasing the quantity of captured analyte. The strong point of this approach is the unnecessariness of any ad-hoc technological steps, allowing its application to the design of high-sensitive resonant structures using commercially available MEMS processes. To proof this concept, perforated resonant sensors, fabricated using two commercial MEMS technologies, available through the multi project wafers of the EUROPRACTICE consortium, will be presented. This thesis is structured as follows:

- In **chapter 1** an overview of the stated of the art in BioMEMS for diagnostical applications will be presented. The chapter is aimed at highlighting advantages and drawbacks of the various sensing strategies present in BioMEMS. A more detailed treatise will be reserved to devices exploiting the resonant sensing strategy.

- In **chapter 2** the original approach based on drawing a pattern of holes on the resonator will be introduced and motivated by making a comparison with the standard "holes-free" approaches used to design high-sensitivity resonant devices. Thereafter, in order to estimate the overall resonant sensor performances, established models for electrostatic actuation, limit of detection and quality factor, will be presented.

- In **chapter 3** the overall project of a perforated beam resonant sensor will be presented. An original analytical model for the estimation of the resonance frequency in presence of perforations will be developed and thus used, in conjunction with the models presented in chapter 2, to estimate the sensor performances. Preliminary measurements will be also shown.

- **Chapter 4** will be dedicated to the project of a perforated resonant sensor based on the Lamé resonant mode. Following the same approach of the previous chapter, an original analytical model will be developed to estimate the effect of perforations over the resonance frequency. Thereafter, the sensor performances will be estimated, highlighting advantages and drawbacks of the Lamé topology with respect to the beam one.

- In **chapter 5** a new resonant structure, based on a phononic crystal, will be introduced. It will be shown that the peculiar characteristics of this structure are suited for sensing applications. The preliminary work presented in this chapter is aimed at developing a fast and simple analysis and synthesis tool for such structures.

1

BioMEMS for diagnostic applications

1.1 BioMEMS summary

In the 1980s the acronym MEMS (Micro Electro Mechanical Systems) was for the first time introduced to describe miniaturized systems where mechanical and electrical parts were interfaced together on the same silicon substrate [1]. These systems were aimed at realizing sensing and/or actuation functions with the surrounding environment. Following the success of integrated electronics, which exploded in the ICs revolution from the 1960s to the 1980s, MEMS market, applications and research areas have been growing constantly in the last 20 years. As a result the MEMS acronym has gone well beyond the initial electro-mechanical meaning. Nowadays it includes devices exploiting principles from different physical worlds such as thermo and fluid dynamics, electromagnetism, optics, chemistry and biochemistry. A very important class of MEMS is the one designed for biomedical applications, also called BioMEMS. In [2] Bashir gives a more rigorous definition, claiming that BioMEMS are “devices or systems, constructed using techniques inspired from micro/nano-scale fabrication, that are used for processing, delivery, manipulation, analysis, or construction of biological and chemical entities”. BioMEMS are expected to be the most important class in the future. One can find at least two main reasons for the success of such devices: on the market point of view, MEMS have met the request of affordable, effective and noninvasive healthcare systems, arisen with the growing of heart population and aging of developed countries. From the research and development point of view MEMS approach improved performances, raising sensitivities due to their sizes comparable to the analyte to be detected and saving time and reagent volumes [2]. Moreover, the possibility of having diagnostical and therapeutical devices (as well as conditioning electronics capable of making them communicate) on the same chip, is one of the most attractive and researched scenarios. BioMEMS have also opened new technological issues related to the exposition of the device to the biological sample: the biological application for which the device is meant should be compatible with MEMS (and CMOS, if electronics is present) substrate [3]. These problems have also pushed toward the employment of new materials others than microelectronics related ones. Among them, particular attention is fucused on polymers, due to their biocompatibility and ease

of fabrication [4]. The use of microfabrication techniques for the syntesis and construction of biological structures have also been explored [5].
MEMS applications in the biological world can be divided into three main fields: diagnostic,therapeutics and tissue engineering. A full dissertation on the whole BioMEMS world is beyond the purpose of this work, a short introduction on therapeutics and tissue engineering will be given in the following, thereafter attention will be focused on diagnostic, with special attention on resonant mechanical sensors which are the subjects of the following chapters. Therapeutic applications mainly involve implantable devices that somehow interact with the human body. Examples of such devices are: microneedles, micropumps and microreservoirs for drug delivery [3, 6], nanoparticles coated with proteins able to damage unwanted cells and tissue [7]. Tissue engineering deals with "the possibility to replace damaged or diseased organs with artificial tissues engineered from a combination of living cells and biocompatible scaffolds" [8].

1.2 BioMEMS for diagnostic applications

Diagnostics represents the largest and most researched BioMEMS segment. BioMEMS for diagnostic purposes are basically transducers converting quantities of biological interest into some output signal, typically electrical, which can be read by the conditioning electronics or laboratory instrumentation. The most part of diagnostic BioMEMS deal with biorecognition, i. e. the detection of target biochemical entities such as molecules, proteins, DNA, cells, viruses, bacteria. Typical application areas are clinical diagnosis, environmental control, food safety, explosives and drugs detection. In order to recognize the target biochemical entity (also called analyte) among the others contained in the analyzed environment or biological sample, BioMEMS have bioreceptors immobilized on their surface (also called functionalized suface). Bioreceptors are complementary biochemical entities that selectively bind to the target through a chemical reaction. Examples of bioreceptors are antigens with their specific antibody or single DNA chains with their complementary strands. Signal change takes place upon binding of the target to its bioreceptor. Depending on the nature of this signal, BioMEMS can be divided into three categories: optical, electrical and mechanical. In the following, a short presentation of the main characteristics of these categories will be given, highlighting strong and weak points of each one.

1.2.1 Optical detection

Nowadays optical detection techniques based on a fluorescence or chemiluminescence labelling technique are the most frequently used [9, 10]. Before binding on the device surface, target molecules are marked (labelled) with a fluorescent (or chemiluminescent) molecule. Upon binding, biochemical entities other than the target are washed out. Thereafter, quantitative measurement of the target presence on the device surface is obtained by reading the emitted light intensity. The labelling process is the key step of this tech-

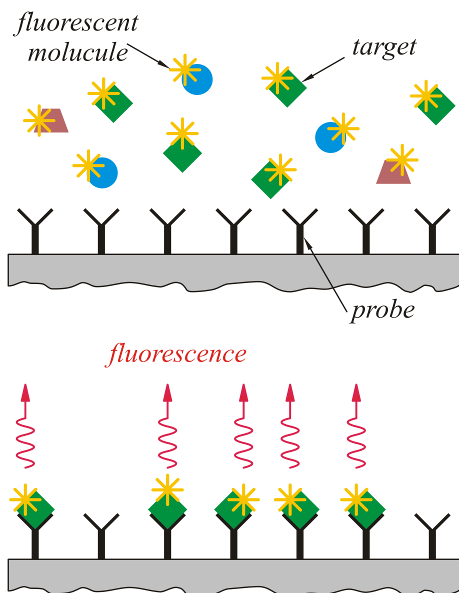

Figure 1.1: Schematic of the optical detection technique using labelling with a fluorescent molecule.

nique of detection, but is also its main limit, since it is labor-intensive, time-consuming and thus cost-raising. Labelling can also have detrimental effects on the target-analyte interaction [11] and cause steric hindrance with resulting reduction of the produced light intensity [12, 13]. For these reasons, a great effort of the research community has been pointed toward the development of detection techniques not exploiting the labelling step. In order to stress this key improvement, these techniques are often called label-free techniques. Concerning optical detection, an emerging label-free technique is *Surface Plasmon Resoncance* (SPR) [13, 14, 15]: probes are immobilized on a thin metal film (usually 10-100 nm thick gold) deposited on a glass substrate through which a reflectance measure is performed (see figure 1.2). By varying the incidence angle, it is observed that, for a very narrow range of angles, the reflectance is weak or even zero. The incident photons, instead of being reflected, are absorbed by the metal, whose electrons are exited and begin to resonate, creating the so-called plasmon resonance. When the analyte binds in the immediate vicinity of the refraction surface, the incidence angle for which plasmon resonance occurs changes too. This effect is exploited to detect analyte adsorption.

The other limit of optical detection is its lack of integrability, with particular emphasis on the readout systems. The readout of optical detection devices needs precisely arranged and aligned microscopes, lasers, spectrophotometers, lenses and filters. While these facilities and technologies are quite straightforward in a laboratory environment, they are difficult to miniaturize into a low-cost, portable and robust system. Furthermore, fluorescence techniques suffer of a reduced sensitivity due the shortening of the optical

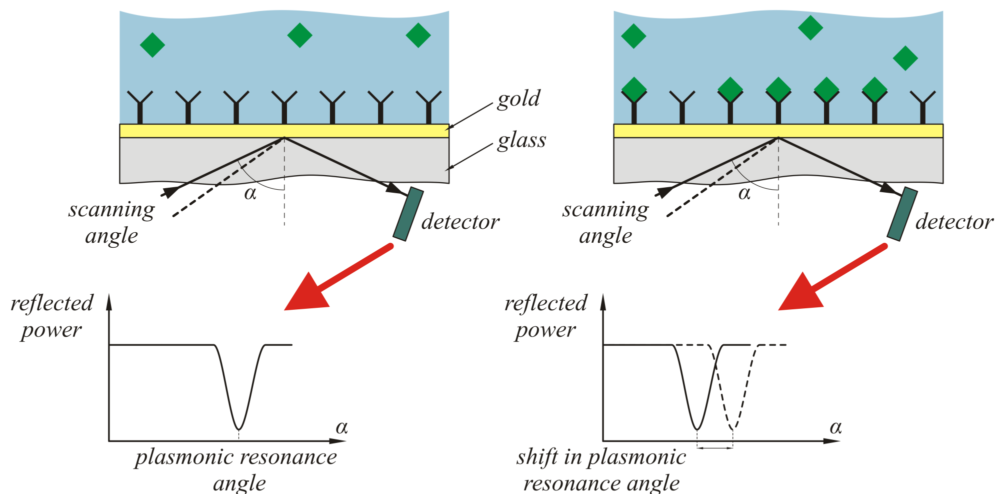

Figure 1.2: Schematic of the *Surface Plasmon Resonance* detection technique. Adapted form [13].

path length through the sample, and to an increased noise due to non-specific binding to the chamber walls when miniaturized [16]. To address these issues, several attempts of monolithic integration of optical and optoelectronic devices, together with the functionalized surface have been made. Among them we can cite: CCD and CMOS optical sensors [17], filters and LEDS [18], Lasers [19]. In conjunction with these on-chip integrated components, there is an alternative approach of incorporating low-cost laser diodes, LEDs, CCD cameras, photodiodes and phototransistors into portable diagnostic platforms [20, 21]. Following the latter approach, several portable SPR devices have been realized [16], among them, also a pair of commercially available devices can be found [13, 22].

1.2.2 Electrical detection

Electrical detection techniques can be in turn divided into three subcategories: amperometric, potentiometric and conductometric detection.

- In amperometric detection target entities bind to their bioreceptors through a redox reaction taking place onto an electrode. The current generated from the reaction is collected and measured from the same electrode. The most common application is the detection of glucose: an enzyme named *glucose oxidase* is immobilized on the electrode and works as a catalyst for the reaction that produces gluconic acid and hydrogen peroxide in presence of oxygen, glucose and water. The hydrogen peroxide is then reduced on a reference electrode and the current between these two electrodes is measured [13, 23].

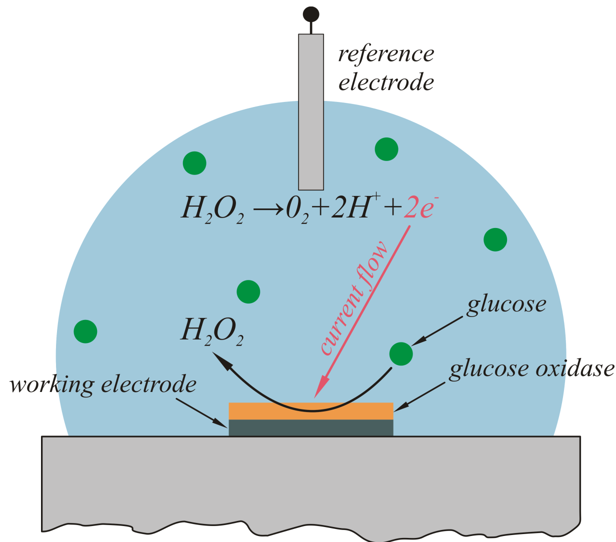

Figure 1.3: Schematic of the glucose detection using amperometric technique.

- The standard approach in potentiometric detection entails the direct measure of the potential between an ion-sensitive electrode (ISE) and a reference electrode. This method is widely used and commercially available for ion detection [24]. An alternative approach involves Ion Sensitive Field Effect Transitor [25] (ISFET or also Chem-FET). ISFETs are MOS structures where the gate metal is replaced by an electrolytic solution and a reference electrode (see figure 1.4). Different effects can result in an increase (or decrease) of immobilized charges at the interface between the solution and the gate oxide, these changes affect the threshold voltage and thus the drain current.

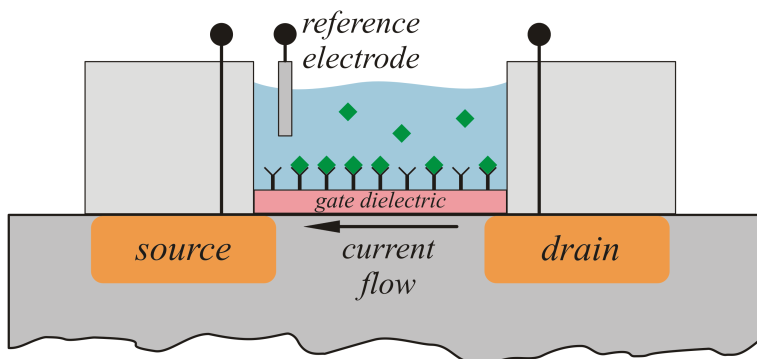

Figure 1.4: Schematic of the potentiometric detection employing an ISFET.

- In conductometric detection the impedance shift between two electrodes immersed in the solution is measured (see figure 1.5). Impedance change can happen at the interface between the solution and the electrodes or in the bulk of the solution itself. Many cellular and microbial activities involve a change in ionic species, implying an associated change in the reaction solution. DNA [26] and *E. Coli* [27] detection by means of a conductivity sensor have been demonstrated.

An interesting example of a commercially available electrochemical sensor exploiting all the three described techniques is the *i-STAT* chemistry analyzer [28]. This is a portable device with disposable cartridges capable of rapidly analyzing 25 blood parameters.
As it will be clear after the discussion above, all these techniques request an electroactive analyte to be performed. If the considered analyte does not fulfill this request, the problem can be circumvented by labelling the target with either an electroactive species or an enzyme that converts an electrochemically silent species into electroactive one [29]. Other issues related to electrochemical detection are the heavy influence of temperature variations, pH and ionic concentrations. Background interference of the label with non-specific redox species present in the sample is also a concern. Electrochemical detection devices are very attractive since the nature of their output signal fits perfectly with the monolithic integration of readout electronics. Sensing structures are also amenable of miniaturization, potentiometric sensors exploiting the ISFET configuration have been downscaled to the nanometers scale using silicon nanowires [30] and carbon nanotubes [31]. Due to their high surface to volume ratio binding events result in a more significant change in the electrical properties of the circuit, and thus in an increased sensitivity, even down to the single analyte level. Despite these great advantages the integration of these structures

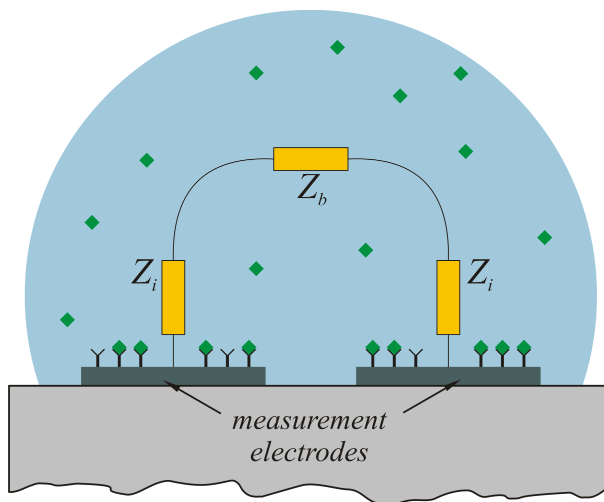

Figure 1.5: Schematic of the conductometric detection.

with modern semiconductor manufacturing techniques and their large scale integration is still a challenge [2, 32].

1.2.3 Mechanical detection

If optical detection is the most used nowadays, mechanical detection is the most researched area among the three described in this chapter. Mechanical detection techniques are based on the change of a mechanical property of the sensing structure upon binding of the target analyte. They can be divided into two subcategories: static and dynamic.

- In the static detection mode the upper surface of a cantilever is funcionalized. Analyte binding results in surface stress change, which leads to deflection of the cantilever. Deflection is usually measured at the tip (where it is maximum) by means of an optical setup, but piezoresistive readout, using resistors integrated at the cantilever joint, has also been demonstrated [33, 34]. A simple model for the cantilever bending, working only when the functionalized layer is very thin in comparison with the cantilever thickness t, is the Stoney's formula [35]:

$$\frac{1}{R} = \frac{6(1-\nu)}{Et^2}\sigma \tag{1.1}$$

  where R is the radius of curvature of the cantilever, σ the induced surface stress, ν the Poisson's ratio and E the Young's modulus of the cantilever material. Using (1.1) the output deflection can be determined:

$$\Delta z = \frac{3(1-\nu)l^2}{Et^2}\sigma \tag{1.2}$$

  where l is the cantilever length. This model shows that,in order to increase sensitivity, the cantilever has to be made as long an thin as possible. With the same purpose of raising the sensitivity, polymer-based cantilevers, with a very low Young's modulus have been proven as sensors [12, 36]. The drawback of these approaches is dealing with suspended fragile structures. Unfortunately, not all the static detection devices can be studied with this straightforward approach, and more complex models have to be used [35]. Moreover, the origin of surface stress due to analyte binding has been much debated but it is still not completely understood [12, 36]. This makes difficult to connect the cantilever deflection to the amount of bound analyte on the functionalized surface, i.e. to estimate the device sensitivity. Other documented issues with static detection are the long time instability of the stress, and its need of a uniform coverage of the surface to take place [37]. For all these reasons static detection has been gradually overtaken by the second mechanical detection principle, i.e. dynamic detection.
- In the dynamic detection mode the resonance frequency f_0 of a mechanical structure is measured before and after exposition of the structure to the target biochemical

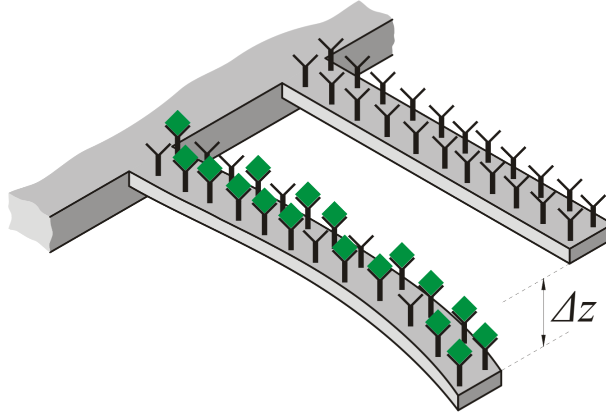

Figure 1.6: Schematic of the static mechanical detection.

entity. The increase in mass due to binding of the target analyte results in a down frequency shift of f_0. In literature it is common to refer at this type of devices with the name of *resonant sensors*. The resonance frequency shift can be qualitatively described with few mathematical expressions. In the neighborhood of the resonance frequency of a generic mechanical resonator, linearization leads to lumped-model expression:

$$f_0 = \frac{1}{2\pi}\sqrt{\frac{k}{m}} \tag{1.3}$$

where k and m are the dynamic stiffness and mass respectively (see 2.2.2). The added mass Δm and the resonance frequency shift Δf_0 are related by:

$$\Delta m = \frac{k}{4\pi^2}\left[\frac{1}{(f_0 + \Delta f_0)^2} - \frac{1}{f_0^2}\right] \tag{1.4}$$

since $\Delta f_0 \ll f_0$, equation (1.4) can be linearized too:

$$\Delta f_0 = -\frac{1}{2}\frac{f_0}{m}\Delta m \tag{1.5}$$

A remarkable difference of dynamic mechanical detection compared to the previously treated detection principles, is that it allows mass detection, enabling new applications such as mass spectroscopy [38]. On the other hand, if the analyte mass and the number of binding sites per unit surfaces are known, the added mass can be converted into a surface occupancy, comparable with the information obtained with optical methods. As it is claimed in Craighead's review [12], considering the added mass as the meaningful quantity to be detected is the natural way of work when detecting single small entities such as bacteria, viruses, nanoparticles and individual molecules. In this case, using (1.5), the mass sensitivity S_m of the resonator can be defined as:

$$S_m = \frac{y_0}{\Delta m} = -\frac{1}{2m} \quad [\mathrm{kg}^{-1}] \tag{1.6}$$

where the normalized frequency shift $y_0 = \Delta f_0/f_0$ has been introduced. Equation (1.6) shows that, for these applications, resonators have to be made small in order to increase the resonance frequency shift and thus the sensitivity. Following this approach, resonators with dimensions scaled to the nanometric scale (also called NEMS), have been extensively researched and tested, with the aim of detecting smaller and smaller masses [39]. Considering the minimum detectable mass, i. e. the limit of detection of the sensor, it is important to point out that the mass sensitivity S_m is not the only parameter affecting this quantity, other ones, like resonator losses and amplitude of vibration does. This subject will be quantitatively discussed in section 2.3. Scaling the dimensions to the nanometric scale is not an issue-free process: nonlinearity, increased damping due to surface losses and surface stress effects are unwanted effects documented in literature [40, 41, 39]. The most common unwanted effect in NEMS resonators is the surface stress effect. As we already discussed, binding of analytes of the functionalized surface involves not only a mass increase, but also a surface stress. While the mass increase is not a factor in static detection, surface stress can modify the resonance frequency. This effect is modelled with a change Δk in the resonator elastic stiffness:

$$\frac{\Delta f_0}{f_0} = \frac{1}{2}\left(\frac{\Delta k}{k} - \frac{\Delta m}{m}\right) \tag{1.7}$$

If Δk is big enough, this surface stress effect can completely cover the added mass effect. This effect is not always considered as unwanted, since it can increase the resonance frequency shift and thus allowing a sensitivity raise. The drawback in using the stress effect to increase Δf_0 lies, as in the case of static detection, in the complex relationship between surface occupation, stress and resonance frequency change. For this reason the mass addiction effect is usually considered preferable, as it can be handled with a very straightforward model. Another problem often encountered in single analyte detection, is the dependence of the resonance frequency shift from the position of the analyte binding [42, 43]. If the binding takes place onto a zone of maximum displacement the effect of the resonance frequency will be maximum too. Conversely, if the binding takes place onto a nodal point (i. e. a point with zero displacement) of the resonance mode, the mass addiction will have no effect over the resonance frequency. In order to address this issue, resonant structures with a resonance mode where the funcionalized surface moves rigidly, have been tested [42].
Other types of applications are the ones where the concentration of the target analyte in a solution/environment is the meaningful quantity to be detected. As an example, Prostate Specific Antigen (PSA) is currently used as a biomarker for prostate cancer at concentrations in the range of 0.1 to 10 $\mathrm{ng/ml}$ [44]. In this case the meaningful quantity is the concentration of added mass over the functionalized surface:

$$\mu = \frac{\Delta m}{Surf} \quad [\mathrm{kg/m^2}] \tag{1.8}$$

It is not straightforward to find a relationship between μ and the concentration of the target analyte in the analyzed environment, whether it is a fluid or gas. An interesting example can be found in [45], where Baltes describes a polymer-coated resonant cantilever able of detecting volatile organic compounds. In order to write the resonance frequency shift, a partition coefficient K_c, defined as the ratio of the analyte concentration in the gas phase C_{env} [μg/l] and in the polymeric phase C_{poly} [μg/l], is used:

$$K_c = \frac{C_{poly}}{C_{env}} \tag{1.9}$$

Measure performed on n-octane and toluene where found to be in good accordance with this model. In many practical cases [44] a calibration curve is performed in order to answer this question.
The sensitivity to the added mass concentration (also concentration sensitivity) can be obtained modifying equation (1.6):

$$S_c = \frac{y_0}{\mu} = -\frac{Surf}{2m} \quad [\mathrm{m^2/kg}] \tag{1.10}$$

The relationship between S_c and the design parameters will be extensively discussed in chapter 2, however, equation (1.10) clearly states that strong miniaturization is no more a factor in raising the sensitivity. Despite that, miniaturization is still a strong point of the MEMS approach. For this reason, even if not strongly miniaturized as in the case of NEMS, concentration sensors showing resonance frequency shifts attributable to stiffness effects are widely reported in literature [46]. A problem that may arise with miniaturization regards the position of the analyte binding, which is typically flyweight in concentration sensors. When the structure is exposed to the analyzed environment/sample, the binding of the target entities can be considered uniform over the surface, making the resonance frequency shift independent form the position binding. This assumption holds true if the binding site is much smaller than the area of the functionalized surface and thus may become unverified with strong miniaturization. Finally, another often underestimated drawback of scaling resonator dimensions is the increase of the resonance frequency, which negatively impacts the readout electronic complexity and, in a more general way, the complexity of the resonance frequency measure.

1.2.4 Comparison

In this section a short comparison of the above described detection techniques is performed. As it can be seen from figure 1.7), optical detection is still the state of the art in terms of limit of detection. The considerable effort in developing alternative detection techniques is motivated by the growing request of device for Point-Of-Care (POC) diagnostics [29]. An ideal POC device has to be affordable, portable, robust and easy to use as it has to be accessible to non-specialists, has to accept samples with little or no pre-preparation and give reliable results in a few minutes or even seconds. Despite all

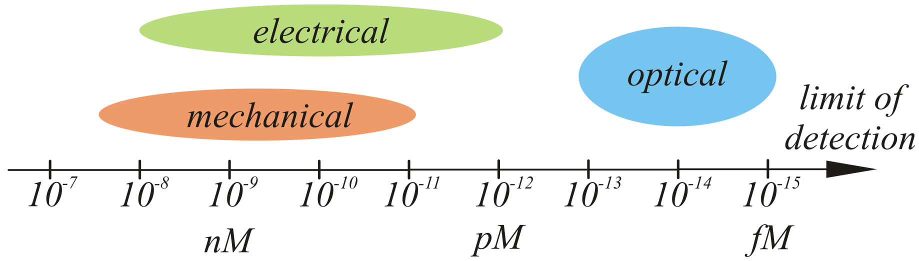

Figure 1.7: Range of the limit of detection in molar concentration of the three detection techniques. Adapted from [13].

the research efforts described in section 1.2.1, a POC optical device is still an ongoing challenge. Toward this vision, electrical and mechanical techniques seems to offer better scenarios, since they are label-free techniques and more amenable to integration. These advantages are summarized in figure 1.8 where the techniques are compared in terms of complexity of the sample preparation and portability. Electrical detection cannot be considered a totally label-free technique since it sometimes exploits label with enzymes electroactive species. Mechanical methods are the most promising in terms of complexity of sample preparation, but still much work have to done in order to reach limits of detection comparable with optical techniques. Finally, it is important to point out that all the treated detection approaches have a common limit imposed by the specificity of the bioreceptor layer. Analytes are often in low concentrations with respect to other

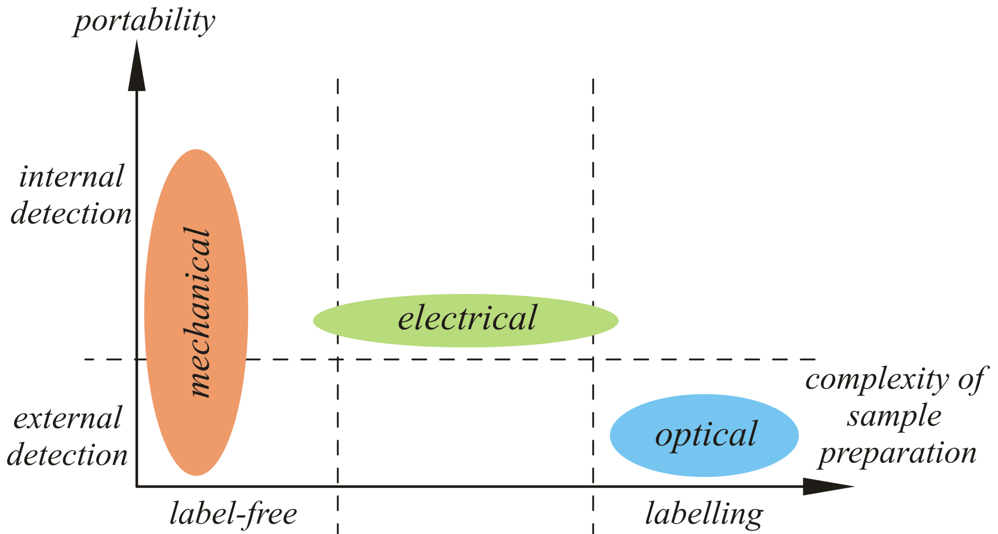

Figure 1.8: Complexity of the sample preparation and portability of the various detection techniques. Adapted from [13].

entities present in the analyzed environment. These entities can non-specifically bind to bioreceptor molecules or non-functionalized device surfaces and deteriorate the system performance, if not causing false positives or negatives. In order to test this important limitation, in several works the sensor is exopsed to non-specific entities [47]. Fluid dynamics, diffusion and transport to the bioreceptor layer, as well as the kinetics of the analyte binding are also important factors to be aware of.

2

Resonant biosensors: a design approach

In this chapter the overall project of a MEMS resonant biosensor will be described. The discussion will be limited to the case where the mass concentration is the meaningful quantity. The relationships between merit parameters such as sensitivity and limit of detection, and the design degrees of freedom will be highlighted, with the aim of finding optimized design guidelines. Moreover, an original design approach, based on drawing a pattern of holes on the sensor, will be discussed and motivated. Recalling the considerations about the possible issues with concentration sensors made in section 1.2.3, in the following of this work, the assumptions below will be considered true:

- Surface stress effects are negligible. Analyte binding results only in a mass addiction.
- The functionalized surface is much larger than the binding site. Therefore the effect of position binding is negligible, the mass addiction can be considered uniform over the resonator and thus modeled with an increase of the material mass density.

This chapter is organized as follows: in section 2.1 the concentration sensitivity S_c of a generic resonant sensor subjected to perforations will be discussed. This perforation approach is aimed at raising S_c and will underlie all the designed structures presented in chapters 3 and 4. As it has already briefly outlined in the mechanical detection section 1.2.3, S_c is not the only merit parameter of the resonant sensor, the limit of detection (LOD), i. e. the minimum mass concentration μ_{min} detectable by the sensor, allows a more fair comparison with the other types of biosensors (see figure 1.7) described in chaper 1. This topic is discussed in section 2.3 where the resonator parameters affecting the limit of detection of a resonant sensors are investigated. After some general considerations, a quantitative treatise of LOD in MEMS resonant sensors read by means of an electronic oscillator (also called MEMS oscillator), which is the most interesting case from an application point of view, will be carried out. In order to adequately present the latter argument, an equivalent electrical circuit for the MEMS resonator is needed. For this reason, the LOD section is preceded by section 2.2, where the electrostatic actuation and detection method, which leads to an equivalent circuit for the resonator, is presented. The electrostatic method is also the one used in reading the devices presented in the follow-

ing chapters. A preliminary characterization based on this technique will be presented in section 3.4 of the following chapter, where the resonance of beam-based sensors will be measured. The resonator quality factor will emerge as a key parameter in both the electrostatic actuation and limit of detection sections, therefore the final section 2.4 of this chapter will be dedicated to the quality factors of MEMS resonators limited by the viscous losses in the surrounding air. As it will be argued, the operation in air (instead of the operation under vacuum) is the most interesting case concerning practical applications of resonant sensors.

2.1 Sensitivity of a perforated resonant sensors

In this section the concentration sensitivity S_c of a generic resonant sensor subjected to perforations will be discussed. As a first step the “standard” full resonator case will be discussed and the relationship between resonator geometry and S_c will be highlighted. Some important drawbacks of raising the sensitivity by acting on these geometrical parameters will be exposed, thereafter the proposed approach of drawing a pattern of holes on the resonator will be introduced. This approach will be motivated by showing that the holes geometry can increase the sensitivity. Finally, once that holes beneficial effect over the sensitivity has been clarified, a numerical optimization example, aimed at finding the optimal holes design in order to maximize S_c, will be presented.
In the last years MEMS resonators have been designed with several different shapes, resonant modes and boundary conditions: in and out-of-plane beams with clamped-clamped, clamped-free [48] and free-free [49] boundary conditions, rods [50], square resonators vibrating in their Lamé [51] and extensional mode [52], disks [53, 54] and others non conventional shapes such as IBARs [55], SiBARs [56] and many others. For

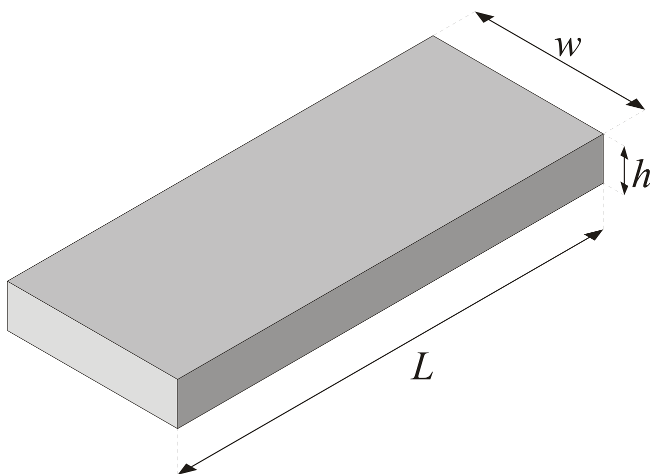

Figure 2.1: Dimensions of a generic resonator.

the purpose of this section, generality can be retained by studying the parallelepiped of figure 2.1. Almost all the above examples geometries (with the only exception of disks) can be described by changing the dimensions L, w and h, which are the parallelepiped length, width and thickness respectively, therefore the treatise will be limited to this case in the following. Assuming that all the surfaces are functionalized, the concentration sensitivity (1.10) can be rewritten as:

$$S_c = -\frac{Surf}{2m} = -\frac{Lw + wh + Lh}{\rho Lwh} \quad [\mathrm{m}^2/\mathrm{kg}] \tag{2.1}$$

where ρ is the material density. A feasible way to increase $\mathbf{S_c}$ is to scale down one of the three dimensions. When this objective needs to be reached, it is customary to scale down the out-of-plane dimension h by using a surface micromachining technology where a very accurate (nanometer scale) control of the structural layer thickness can be achieved by monitoring the deposition process. The in-plane dimensions L, w have instead their minimum sizes limited by the lithography, and are thus not typically suited for strong miniaturization. Scaling down to the lithographic limit also one of the two in-plane dimensions is possible, as in the case of very slender beams, but it does not produce any substantial improvement on the concentration sensitivity. Assuming $h \ll L,w$, equation (2.1) can be approximated as:

$$S_c \simeq -\frac{1}{\rho h} \quad [\mathrm{m}^2/\mathrm{kg}] \tag{2.2}$$

Craighead [44], Lavrick [35] and Baltes [45] found the same result while working on concentration sensitivity of resonant thin cantilevers. Equation (2.2) shows that another possible way to increase the sensitivity is to use a lightweight material. Both the reduction of material density and thickness requires laboratory facilities and may result in an important technological effort. Conversely if the structure is fabricated using a commercial MEMS process accessible through a multi-project wafer, the material is typically silicon or a composite based on silicon (SiGe, SiC) and does not give much room on the choice of ρ. The sensitivity-aimed design optimization is thus reduced the choice of the process with the smallest structural layer thickness. Furthermore, lowering the structural thickness has two important drawbacks that will be discussed in the following. Suspended thin structures placed few micrometers near the substrate, has in the case of structures realized through surface micromachining [57], may become prone to sticking [58]. Sticking has a particularly detrimental effect on BioMEMS, since it affects them twice: firstly during the release step of the technological process (release sticking) and secondly when the biosensor is exposed to the biological sample (in-work sticking). In the case of release sticking design rules defining maximum in-plane dimensions are usually present in order to avoid this phenomenon. In some cases, when sticking affects the technology in a very detrimental way, ad-hoc release steps, such as supercritical drying on vapor etching may be available. In the case of in-work sticking instead, the situation is more coumbersome, since there is no help from the technological process. Moreover, the fluid properties, which are key parameters in the arise of sticking, are not exactly known and may vary

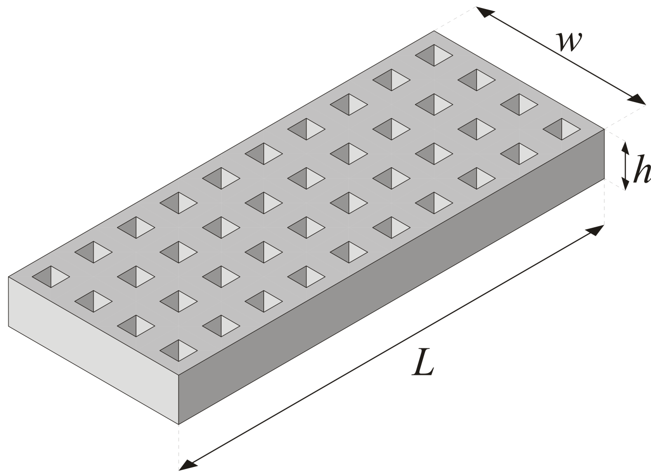

Figure 2.2: Generic resonator with a pattern of square holes arranged over a square matrix.

with different samples. In this case it is only possible to use some mathematical models [59, 60] in order to project with some error margin over the sticking limit. The typical countermeasure adopted to avoid sticking is to decrease the in-plane dimensions L and w, in order to make the structure stiffer in the out-of-plane direction. The drawbacks of dimension scaling in concentration sensors, such as resonance frequency increase and position binding effects have already been discussed in section 1.2.3. Furthermore, low structural thicknesses were found to be the main reason for the arising of surface stress effects in resonant beams [12, 39]. In a previous work of the MEMS research group of the University of Pisa, whose this thesis belongs to, concentration sensitivity of a magnetically actuated torsional resonators has been increased by adding two lateral thin wings [61]. In this case, an ad-hoc postprocessing step, combining RIE and TMAH etching of the substrate has been developed in order to increase the gap between the resonator and the substrate. Due to this expedient, sticking upon exposition to the biological sample has been avoided.

Up to this time the resonator has been considered full, and the several most often encountered complications the designer has to deal with, in order to raise resonant sensors sensitivity, have been surveyed. In the following, the beneficial effect over S_c, of a holes pattern drawn on the resonator, will be shown. The chosen pattern consist of square perforations arranged over a square matrix, as shown in figure 2.2. This kind of pattern is the easiest realizable and probably the most compatible with microfabrication processes. The resonator outer dimensions are the same of the full structure considered in figure 2.1. The hole matrix can be described using the dimensions l_s and t_s shown in figure 2.3. For the purpose of highlighting the holes effect over S_c, the best way to describe the whole structure is to take advantage of these three parameters:

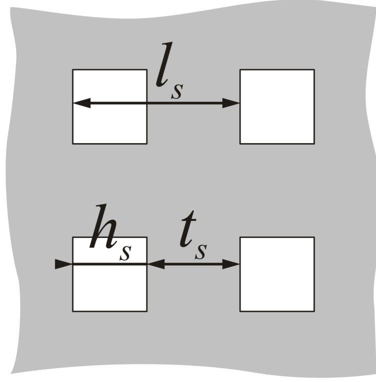

Figure 2.3: Magnification of the holes pattern with dimensions.

$$Ar = \frac{L}{w} \qquad N = \frac{w - t_s}{l_s} \qquad \alpha = \frac{t_s}{l_s} \tag{2.3}$$

where Ar is the aspect ratio of the outer dimensions, assumed to be $Ar \geq 1$ (i. e. L is the bigger in-plane dimension), N is the number of holes along the width w (which can be, in general, a rational number, but in any practical design will be an integer) and $\alpha \in (0, 1]$ is the filling fraction that defines the amount of filled space in the w or L direction. When $\alpha = 1$ the structure is completely filled and the geometry is the one of figure 2.1 independently from N, when $\alpha \to 0$ the structure becomes completely empty and can be seen as a network of slender beams hinged together. Using the parameters defined in equations (2.3) the geometry is described by five parameters: L, h, Ar, N and α. Using these parameters and considering the inner surface of the holes covered with bioreceptors, the sensitivity is:

$$\begin{aligned} S_c = & \frac{L\alpha(N(2 - N(\alpha - 2)) + \alpha) - h(N + \alpha)}{hL(N + 1)(N(\alpha - 2) - \alpha)\alpha\rho} \cdot \\ & \cdot \big(2Ar(\alpha - 1)N^2 - (Ar + 1)N - (Ar + 1)\alpha\big) \quad [\mathrm{m}^2/\mathrm{kg}] \end{aligned} \tag{2.4}$$

The expression 2.4 depends on six parameters: L, h, Ar, N, α and ρ, with only the latter one that can be normalized. Analyzing the behavior of S_c with respect to the five parameters L, h, Ar, N and α is cumbersome. Therefore, in order to highlight the dependence from the holes geometry (which is described by the only parameters N and α), the assumption of large number of holes can be made and the lower order terms in the N variable, appearing in the numerator and denominator of 2.4, can be neglected, thus giving:

$$S_{c-N} = -\frac{Ar}{L\rho} \cdot \frac{2N(1 - \alpha)}{(2 - \alpha)\alpha} \quad [\mathrm{m}^2/\mathrm{kg}] \tag{2.5}$$

As it can be seen from equation (2.5), under this assumption the approximated S_{c-N} is no longer dependent form h and the dependence from L and Ar can be factorized away.

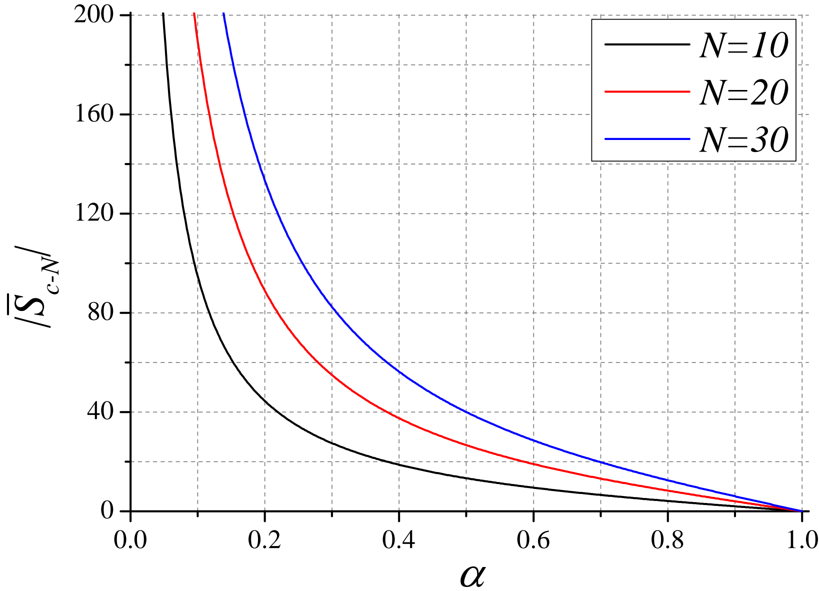

Figure 2.4: $\overline{S}_{c-N}$ as a function of α for $N = 10,\ 20,\ 30$.

Therefore, once that the outer geometry has been defined, the effect of the holes over the sensitivity is described by the nondimensional quantity $\overline{S}_{c-N}$:

$$\overline{S}_{c-N} = -\frac{2N(1-\alpha)}{(2-\alpha)\alpha} \tag{2.6}$$

The quantity $\overline{S}_{c-N}$ (as well as S_c) is always negative, this simply states that the resonance frequency decreases after the mass increase due to the binding of the analyte. For this reason, the sensitivity will be always plotted in absolute value. The plot of $\overline{S}_{c-N}$ as a function of α for three values of N is reported in figure 2.4. As it is shown in figure 2.4, both the parameters N and α, introduced by the holes matrix, can be used to raise the sensitivity. This is a remarkable result if compared with the full resonator case where there are no "effective" degrees of freedom acting on the sensitivity. The perforations approach is even more interesting considering that, in technological processes exploiting surface micromachining, drawing a pattern of holes on the structure is mandatory. This is due to the release step where the sacrificial layer have to be etched (usually through a wet etch) and the etching through the holes is needed to reduce the release step time (see figure 2.5). Once that the beneficial effect of the holes over the sensitivity has been clarified, it is important to investigate what is the best way to draw the holes pattern in order to maximize $|S_c|$.

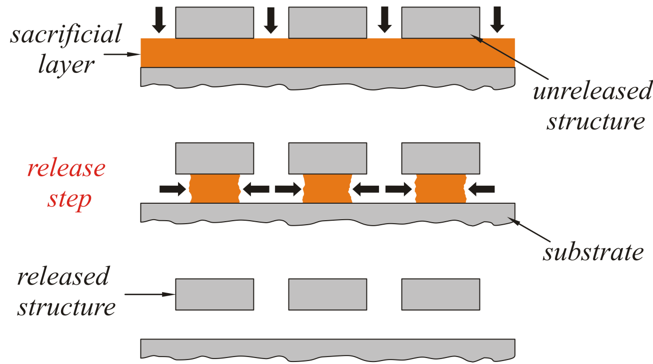

Figure 2.5: Schematic cross section of a generic release step. The sacrificial layer has to be etched through holes patterned on the structure.

2.1.1 Optimal holes design

In this section the best way to draw the holes pattern in order to maximize the device sensitivity is investigated. The analysis will be performed assuming a large number of hole and thus using $\overline{S}_{c-N}$ as the objective function to be maximized over the available design space. The optimization will be performed using two different design spaces, one constrained by only the technological process design rules, and one where an user-defined minimum number of holes N_{min} is defined. Finally, some general considerations over realistic cases where the holes number is limited to few units, an thus $|S_c|$ as to be used as the objective function, will be made. By looking at figure 2.4 it can be clearly concluded that the best design is the one with the most possible holes (maximum N) and largest possible holes (minimum α). These most and largest limits are imposed by the technological process design rules. Considering a generic process, the design rules affecting the geometry of the holes matrix can be summarized as follows:

- *Minimum width*. It is the minimum allowed dimension of the structural layer in any direction. Considering our geometry it sets a lower bound for t_s and will be called $t_{s_{min}}$ in the following.

- *Minimum spacing or minimum hole width*. It is the minimum allowed dimension for the holes in the structural layer. The holes dimension may be also lower-bounded by the ability of covering the trench with bioreceptors or by the ability of reaching these bioreceptors with the target entity. Considering our geometry it sets a lower bound for h_s and thus will be called $h_{s_{min}}$ in the following.

- *Maximum hole distance*. It is the maximum allowed distance between holes. It is imposed by the release step: the longer the etching time and the faster the etching process, the larger the hole distance can be. Considering our geometry it sets an up-

per bound for t_s and thus will be called $t_{s_{max}}$ in the following.

- *Maximum hole size*. It is the maximum allowed dimension for an hole made on the structural layer. Even if it is not a typical design rule, it can be useful to set this upper-bound in order to limit the fragility of the structure. Considering our geometry it sets an upper limit for h_s and thus will be called $h_{s_{max}}$ in the following.

The just described boundaries define the available design space in terms of the geometrical parameters t_s and h_s. In order to investigate the best approach to draw the perforations, it is useful to express the same boundaries as functions of the dimensionless parameters N and α. For this purpose equations (2.3) can be used to express α as a function of N and, in turn, one of the hole dimensions t_s and h_s:

$$\alpha(N, t_s) = \frac{N t_s}{(L/Ar) - t_s} \qquad \alpha(N, h_s) = \frac{(L/Ar) - h_s N}{(L/Ar) + h_s} \tag{2.7}$$

Substituting the 4 boundaries $t_{s_{min}}$, $h_{s_{min}}$, $t_{s_{max}}$, and $h_{s_{max}}$ in equations (2.7), four straight lines are found. The inner surface of these 4 lines is the available design space

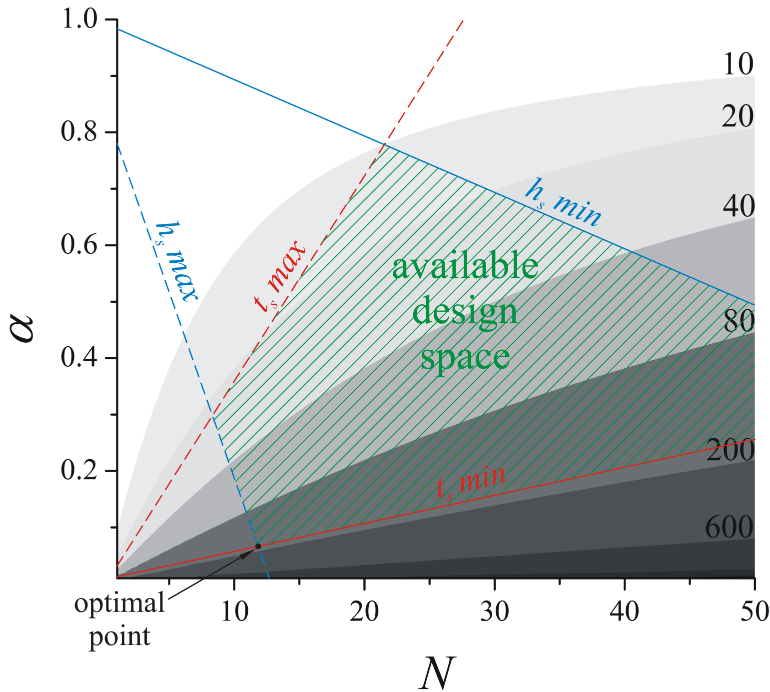

Figure 2.6: Contour plot of $|\overline{S}_{c-N}|$. The available design space generated by generic design rules $t_{s_{min}}$, $h_{s_{min}}$, $t_{s_{max}}$, and $h_{s_{max}}$ is highlighted in green. The optimal point is also shown.

expressed in the (N, α) space. The design space generated by some generic design rules is reported over the contour plot of $\overline{S}_{c-N}$ in figure 2.6. The optimal point, obtained by means of a numerical optimization tool, is found to be at the intersection between the $t_{s_{min}}$ and $h_{s_{max}}$ straight lines. The limits imposed by the design rules put the two objectives of most possible holes (hightest N) and largest holes (lowest α) in competition. The optimization point shows that, in this situation, is the objective of largest holes that has to be pursued in order to maximize $|\overline{S}_{c-N}|$. Since the optimal point has not necessarily an integer value for N, the real design point will be the nearest to the optimal one, belonging to the $t_{s_{min}}$ straight line and with an integer value for N. The drawback of utilizing this optimal point may be dealing with a low number of holes along w and L. This is in conflict with assumption made in order to obtain the normalized sensitivity $\overline{S}_{c-N}$, moreover, as it will be shown in the following chapters, having a large value for N can help to predict the resonance frequency of the structure with simple mathematical models. For these reasons, design using a lower boundary N_{min}, limiting the minimum number of holes along the width w, can be useful. In this case the available project space and the optimal point change as in figure 2.7. This alternative definition of the available

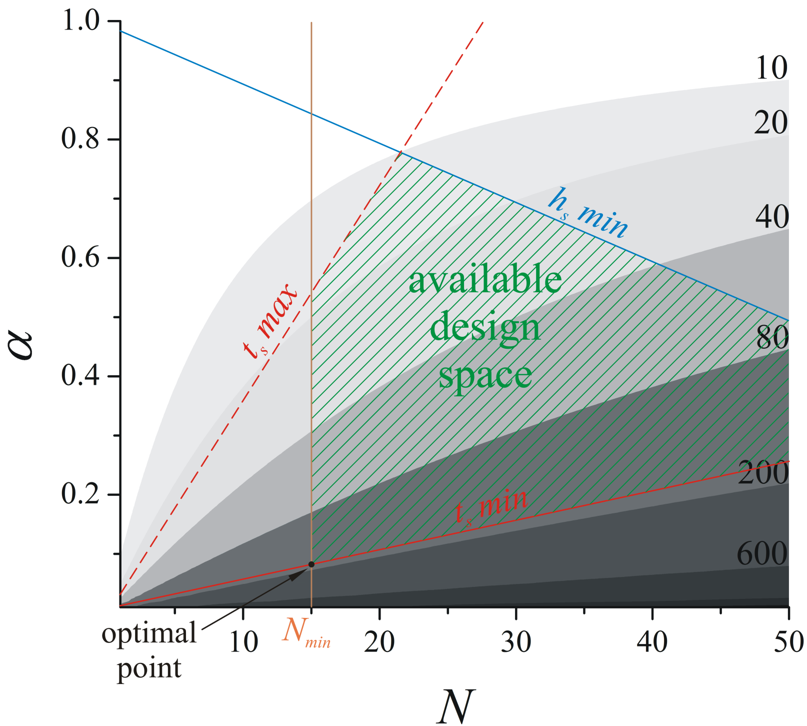

Figure 2.7: Contour plot of $|\overline{S}_{c-N}|$. The available design space generated by generic design rules $t_{s_{min}}$, $h_{s_{min}}$, $t_{s_{max}}$, and the ad-hoc defined lower boundary N_{min} is highlighted in green. The optimal point is also shown.

design space does not change the substance of the optimization, since the optimal point is still the one with the lowest possible value of α. Even if this result has been obtained using the simplified expression $|\overline{S}_{c-N}|$ of equation (2.6), it is worth to point out that the above described optimization has been performed also for the real structures that will be presented in chapters 3 and 4, using the design rules of the two employed technological processes, the real outer dimensions L, w and h, and the non-approximated objective function $|S_c|$ of equation (2.4). The obtained optimal point has always been the one with the lowest possible value of α. Finally it is important to reaffirm that the sensitivity is not the only merit parameter of the resonant sensor and the same holes matrix that has been found to beneficially impact the sensitivity may also impact other important parameters in a detrimental way. For this reason, the effect of perforations over these quantities have to be studied as well.

2.2 Electrostatic actuation

Thus far the resonant sensor has been considered as a mechanical structure capable of giving a resonant frequency f_0 function of various parameters. Among them, the dependence from the mass (initial and added) has been highlighted in order to describe the sensing principle. The problem of how to excite vibrations into the structure and then detect its resonance frequency has been solved in several ways, short reviews about the most common actuation and sensing strategies in MEMS can be found in [35, 36], among the various techniques, electrostatic actuation is one of the most used. The ease of fabrication (only a narrow gap between the structure and a fixed electrode is needed) and the straightforward modeling are strong advantages of this method. Piezoelectric actuation is another often employed technique, but needs a more complex technology allowing the deposition of piezoelectric materials. Furthermore, modeling the piezoelectric effect can be cumbersome. The main drawback of electrostatic actuation is dealing with low vibration amplitudes and thus weak meaningful signals, which are often totally or partially covered by parasitic effects. Another problem, regarding the specific biosensing application, is the stiction effect that can occur in the narrow gap between the resonator and the fixed electrode. For this reason, modeling and estimations of this effect are needed in order to design stiction-free structures. A previous work of this research group was focused on this argument and demonstrated the possibility of fabricating stiction-free structures even with few microns of structural layer thickness [62]. In this section, the modelling of the electrostatic actuation and sensing method, which is the one exploited for measuring the resonant sensors presented in chapters 3 and 4, will be discussed. The model will finally lead to the equivalent electrical circuit of an electrostatically actuated and detected resonator. In order to better understand the topic, the model will be initially derived for the easier case of lumped parameters mechanical resonators, thereafter an extension to the case of distributed parameter systems (where the devices of this thesis falls), will be given. However, this section has not to be intended as a exhaustive dissertation on electrostractically actuated systems. For a comprehensive treatise of lumped parameters electromechanics the reader is referred to [63], for distributed parameters electromechanics to [64].

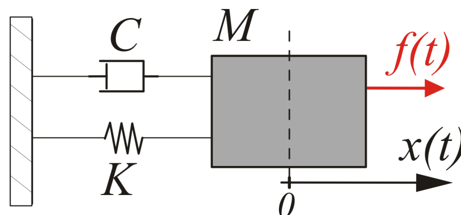

Figure 2.8: Schematic representation of a mass, spring and damper system.

Mechanical	**Electrical**
Force $[\mathrm{N}]$	*Voltage* $[\mathrm{V}]$
Velocity $[\mathrm{m/s}]$	*Current* $[\mathrm{A}]$
Mass $[\mathrm{kg}]$	*Inductor* $[\mathrm{H}]$
Spring $[\mathrm{N/m}]$	*Capacitor* $[\mathrm{F}]$
Damper $[\mathrm{kg/s}]$	*Resistor* $[\Omega]$

Table 2.1: Analogies between electrical and mechanical domains.

2.2.1 Lumped parameters

As a first step in order to derive a model for lumped parameters electromechanical systems, an equivalent electrical circuit for lumped parameters mechanical systems will be given. The Newton's second law for the mass, spring and damper system of figure 2.8 is:

$$f(t) = M\frac{d^2}{dx^2}x(t) + C\frac{d}{dx}x(t) + Kx(t) \tag{2.8}$$

where $F(t)$ is the applied force, M the resonator mass, C the viscous damping coefficient, K the spring constant and $x(t)$ the mass displacement along the x axis. Equation (2.8) can be rewritten in the frequency domain assuming a sinusoidal solicitation and using the velocity as the unknown variable:

$$F(j\omega) = j\omega M V_{el}(j\omega) + C V_{el}(j\omega) + \frac{K}{j\omega}V_{el}(j\omega) \tag{2.9}$$

where $F(j\omega)$ and $V_{el}(j\omega)$ are the phasors of the applied force and velocity respectively. Equation (2.9) is formally identical to the Kirchhoff second law for an R-L-C series resonant circuit. In this analogy the force is the voltage, the velocity is the current, the mass acts as an inductor, the spring acts as a capacitor of capacity $1/K$ and the damper acts as a resistor. These analogies are summarized in table 2.1 and the equivalent circuit is shown in figure 2.9. In the electrostatic actuation mechanism the external force acting on the moving mass is the Coulomb force generated by the voltage $\mathbf{V}$ applied between M

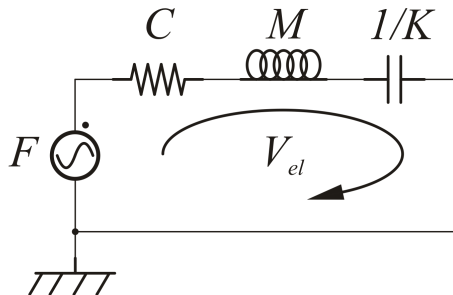

Figure 2.9: Equivalent circuit for the mass, spring, damper system of figure 2.8.

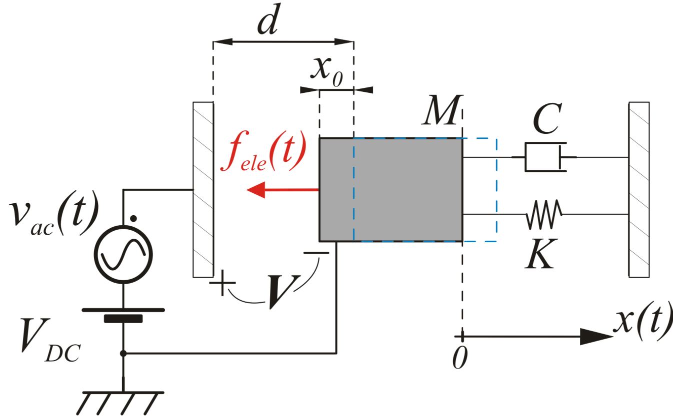

Figure 2.10: Schematic of the electrostatic actuation method with a concentrated parameter system. The static displacement $-x_0$ due to the bias voltage V_{DC} is shown.

and a fixed electrode placed at a distance d, as in figure 2.10. The total applied voltage $\mathbf{V}$ is the sum of the bias voltage V_{DC} and small signal sinusoidal voltage $v_{ac}(t)$. In the same way we can define a total displacement $\mathbf{x} = -x_0 + x(t)$, where $-x_0$ is the static displacement due to the bias voltage V_{DC}, and $x(t)$ is the small signal displacement generated by $v_{ac}(t)$. Pursuing this notation, quantities including both the static and small signal parts will be written in bold caps in the following. The electrical field between the parallel plates of the capacitor is:

$$\mathbf{E} = \frac{\mathbf{V}}{d + \mathbf{x}} \tag{2.10}$$

In order to write the Coulomb force acting on the moving plate, only the electrical field generated by the charges on the fixed electrode have to be considered, i.e. half of the total electrical field:

$$\mathbf{f_{ele}} = -\mathbf{q}\frac{\mathbf{E}}{2} = \frac{\mathbf{C_{ap}}\mathbf{V}^2}{2(d + \mathbf{x})} = -\frac{\epsilon_0 A \mathbf{V}^2}{2(d + \mathbf{x})^2} \tag{2.11}$$

where $\mathbf{q}$ is the module of the charge over the electrodes. In the last equation the expression for the parallel plate capacity $\mathbf{C_{ap}} = \epsilon_0 A/(d + \mathbf{x})$ has been used, with ϵ_0 being the electrical permittivity of the vacuum and A the area of the plates. Using the just derived expression for the Coulomb force, the equation for the static displacement x_0 is found:

$$-\frac{\epsilon_0 A V_{DC}^2}{2(d - x_0)^2} = kx_0 \tag{2.12}$$

In order to extract an equivalent circuit for the electrostatic actuator, equation (2.11) have to be linearized in both the $\mathbf{V}$ and $\mathbf{x}$ variables, using $\mathbf{V} = V_{DC}$ and $\mathbf{x} = -x_0$ as the bias point. Considering only the small signal terms:

$$f_{ele} = \left.\frac{\partial \mathbf{f_{ele}}}{\partial \mathbf{V}}\right|_{\mathbf{V}=V_{DC},\mathbf{x}=-x_0} v_{ac}(t) + \left.\frac{\partial \mathbf{f_{ele}}}{\partial \mathbf{x}}\right|_{\mathbf{V}=V_{DC},\mathbf{x}=-x_0} x(t)$$

$$= \underbrace{-\frac{\epsilon_0 A V_{DC}}{(d-x_0)^2}}_{\eta} v_{ac}(t) + \underbrace{\frac{\epsilon_0 A V_{DC}^2}{2(d-x_0)^3}}_{K^*} x(t) \tag{2.13}$$

the resulting linearized force has two terms: the first is a small signal force linearly dependent from $v_{ac}(t)$ through the *electromechanical coupling coefficient* η, the second is a spring force proportional to the small signal displacement $x(t)$ through the *spring softening constant* K^*. Equation (2.13) can be rewritten in the frequency domain an substituted in (2.9) to give:

$$\overbrace{\eta V_{ac}(j\omega) + \frac{K^*}{j\omega} V_{el}(j\omega)}^{F_{ele}(j\omega)} = j\omega M V_{el}(j\omega) + C V_{el}(j\omega) + \frac{K}{j\omega} V_{el}(j\omega)$$

$$\eta V_{ac}(j\omega) = j\omega M V_{el}(j\omega) + C V_{el}(j\omega) + \frac{\overbrace{K - K^*}^{K_{eq}}}{j\omega} V_{el}(j\omega) \tag{2.14}$$

Equations (2.14) clarify the name of *spring softening constant* given to K^*, since it results in a decrease of the system spring constant from the mechanical spring K to the total spring $K_{eq} = K - K^*$. In literature it is common to refer to this effect as the *spring softening effect*, which makes the spring constant (and thus the resonance frequency f_0) a function of the bias voltage V_{DC}. In order to complete the model, an expression for the current generated by the small signal source $v_{ac}(t)$ is needed. The charge $\mathbf{q}$ over the plates of the capacity can be written as:

$$\mathbf{q} = \mathbf{C_{ap}} \mathbf{V} = \frac{\epsilon_0 A \mathbf{V}}{d + \mathbf{x}} \tag{2.15}$$

performing the same linearization and considering only the small signal terms:

$$q = \left.\frac{\partial \mathbf{q}}{\partial \mathbf{V}}\right|_{\mathbf{V}=V_{DC},\mathbf{x}=-x_0} v_{ac}(t) + \left.\frac{\partial \mathbf{q}}{\partial \mathbf{x}}\right|_{\mathbf{V}=V_{DC},\mathbf{x}=-x_0} x(t)$$

$$= \underbrace{\frac{\epsilon_0 A}{d - x_0}}_{C_0} v_{ac}(t) \underbrace{-\frac{\epsilon_0 A V_{DC}}{(d-x_0)^2}}_{\eta} x(t) \tag{2.16}$$

where C_0 is the static value of $\mathbf{C_{ap}}$. The small signal current can be easily computed from (2.16):

$$i \simeq \underbrace{C_0 \frac{dv_{ac}(t)}{dt}}_{i_c} + \underbrace{\eta \frac{dx(t)}{dt}}_{i_{mot}} \tag{2.17}$$

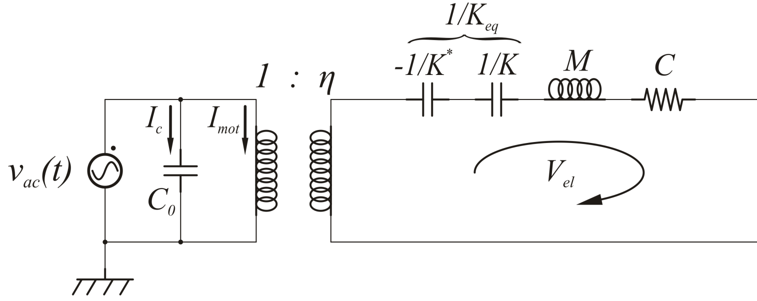

Figure 2.11: Equivalent circuit for the electromechanical system of figure 2.10.

where the fist term i_c is the *static current* due to the variable voltage $v_{ac}(t)$ applied to the constant capacitor C_0, and the second term i_{mot} is the *motional current* due to the distance variation $x(t)$ between the electrodes of a capacitor with an applied constant voltage V_{DC}. The frequency domain equation is:

$$I(j\omega) = j\omega C_0 V_{ac}(j\omega) + \eta V_{el}(j\omega) = I_c(j\omega) + I_{mot}(j\omega) \tag{2.18}$$

Equations (2.14) and (2.18) describe the small signal relationship between the electrical and mechanical domains for the system of figure 2.10. It is easy to show (Tilmans) that this relationship belongs to an ideal voltage transformer. The system equivalent circuit is therefore shown in figure 2.11. The motional current is directly related to the velocity of the moving mass M and thus exhibit the resonance peak. By solving the equivalent circuit I_{mot} is found to be:

$$I_{mot}(j\omega) = \frac{\eta^2}{j\omega M + C + \frac{K_{eq}}{j\omega}} V_{ac}(j\omega) = Y_m(j\omega) V_{ac}(j\omega) \tag{2.19}$$

where $Y_m(j\omega)$ is the resonator transconductance, i. e. the ratio of the motional current to the applied small signal voltage. $Y_m(j\omega)$ can be rewritten in a more useful way exploiting the resonance pulsation $\omega_0 = \sqrt{K_{eq}/M}$, and the quality factor Q:

$$Y_m(j\omega) = \frac{1}{K_{eq}} \frac{j\omega\eta^2}{\left(\frac{j\omega}{\omega_0}\right)^2 + \frac{j\omega}{\omega_0 Q} + 1} \tag{2.20}$$

The amplitude and phase behavior of the resonator transconductance $Y_m(j\omega)$ are shown in figures 2.12 and 2.13 respectively. The quality factor is a key parameter of the resonator. The most general definition exploits an energy ratio:

$$Q = 2\pi \frac{energy\ stored}{energy\ dissipated\ in\ 1\ period} \tag{2.21}$$

using this definition the quality factor can be easly related to the circuit parameters:

$$Q = \frac{M\omega_0}{C} \tag{2.22}$$

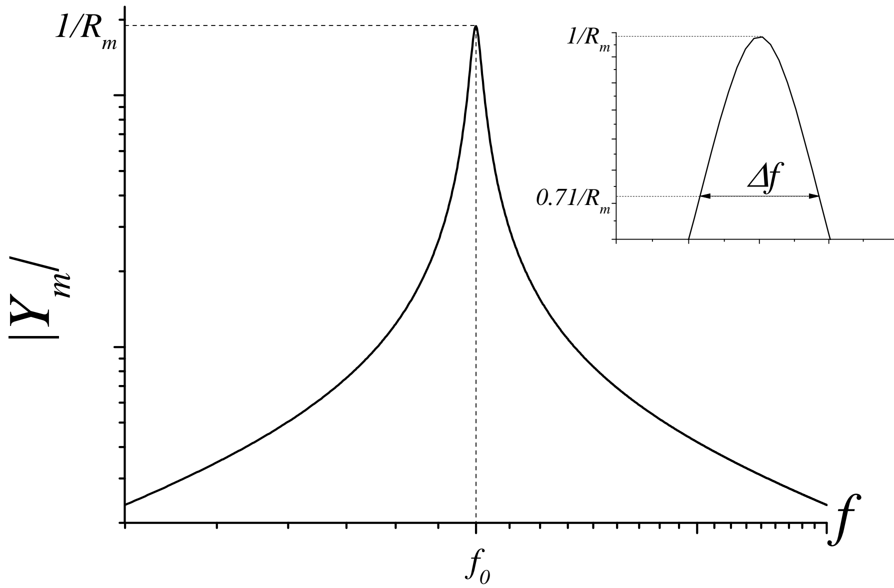

Figure 2.12: Amplitude of the resonator transconductance Y_m. The peak value is inversely proportional to the motional resistance R_m defined in 2.24. The frequency width Δf used in the Q definition (2.23) is shown in the inset.

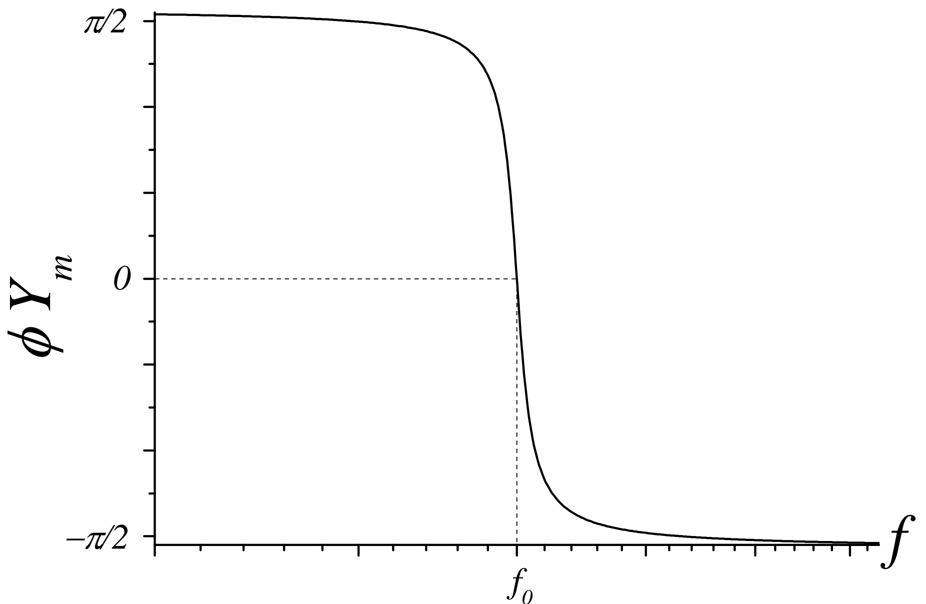

Figure 2.13: Phase of the resonator transconductance Y_m.

An alternative definition, useful to extract Q from the peak amplitude is:

$$Q = \frac{f_0}{\Delta f} \tag{2.23}$$

where Δf is the frequency width where the vibration amplitude (and thus the motional current) is reduced by a factor $\sqrt{2}$ $(-3dB)$, as is shown in the inset of figure 2.12. At the resonance frequency the inductive and reactive parts cancel themselves and the transconductance module reaches its maximum, which is the inverse of the motional resistance R_m:

$$|Y_m(j\omega_0)| = {R_m}^{-1} = \left(\frac{C}{\eta^2}\right)^{-1} \tag{2.24}$$

Unfortunately the motional current is not directly measurable. Measurement can be performed on the total current I (equation (2.18)), where the static current I_c is superimposed over I_{mot}:

$$\begin{aligned} I(j\omega) &= Y_m(j\omega)V_{ac}(j\omega) + j\omega C_0 V_{ac}(j\omega) \\ &= \underbrace{j\omega\left(C_0 + \frac{\eta^2}{K_{eq}}\right)\frac{\left(\frac{j\omega}{\omega_a}\right)^2 + \frac{j\omega}{\omega_a Q_a} + 1}{\left(\frac{j\omega}{\omega_0}\right)^2 + \frac{j\omega}{\omega_0 Q} + 1}}_{Y_t(j\omega)} V_{ac}(j\omega) \end{aligned} \tag{2.25}$$

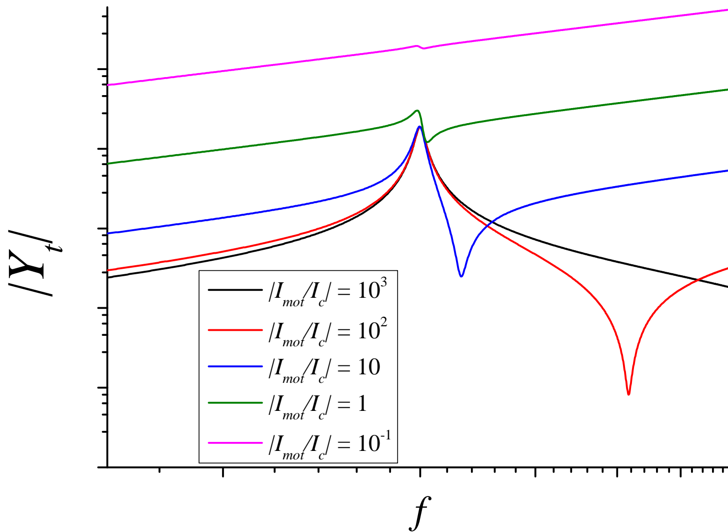

Figure 2.14: Amplitude of the total transconductance Y_t. The plot is shown for various values of the ratio $|I_{mot}/I_c|$ computed at the resonance frequency.

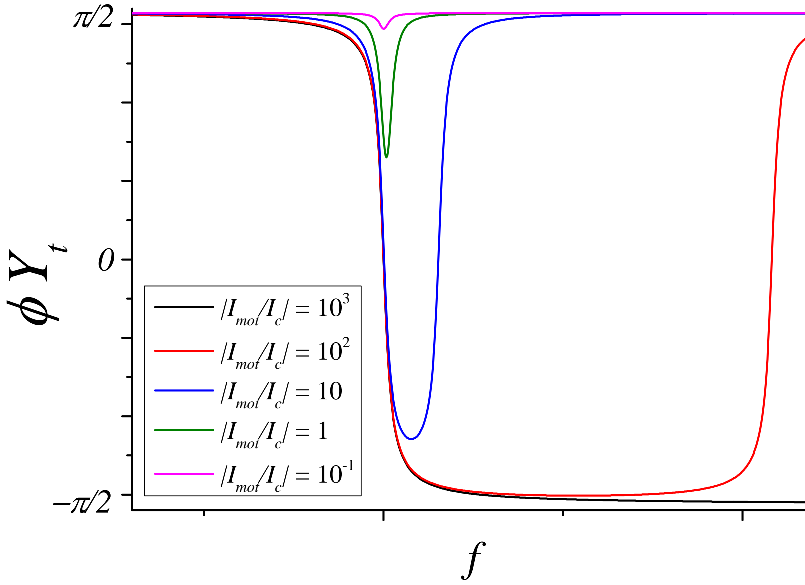

Figure 2.15: Phase of the total transconductance Y_t.

where the total transconductance seen from the small signal source $Y_t = I/V_{ac}$, has been defined. As its shown by equation (2.25), Y_t adds an anti-resonance peak, with pulsation ω_a and quality factor Q_a, to the pure motional response of Y_m. The parameters of the anti-resonance peak are:

$$\omega_a = \omega_0 \sqrt{1 + \frac{\eta^2}{C_0 K_{eq}}} \qquad Q_a = Q \sqrt{1 + \frac{\eta^2}{C_0 K_{eq}}} \tag{2.26}$$

The amplitude and phase of the total transconductance are show in figures 2.12 and 2.13 respectively. In order to highlight the effect of the static current, C_0 is varied and the plots are shown for various values of the ratio between the amplitudes of the two currents I_{mot} and I_c, both calculated at the resonance frequency. As its shown by these plots, the static current progressively cancel the resonance peak. The effect of static current partially or totally deteriorating the resonance is the main problem of the electrostatic actuation. However, a significant improvement can be achieved using a second electrode to sense to current, as shown in figure 2.16. In this new scheme the gap distance is assumed to be the same for both electrodes and the bias voltage V_{DC} is applied on the resonator in order to polarize both gaps. Finally, the measure is performed on the short-circuit current i_{out} at the output electrode. In this situation the static displacement x_0 can be neglected and the electromechanical coupling and spring softening coefficients, as well as the static capacitance, are the same on both ports:

$$C_0 = \frac{\epsilon_0 A}{d} \qquad \eta = \frac{\epsilon_0 A V_{DC}}{d^2} \qquad K^* = \frac{\epsilon_0 A V_{DC}^2}{2d^3} \tag{2.27}$$

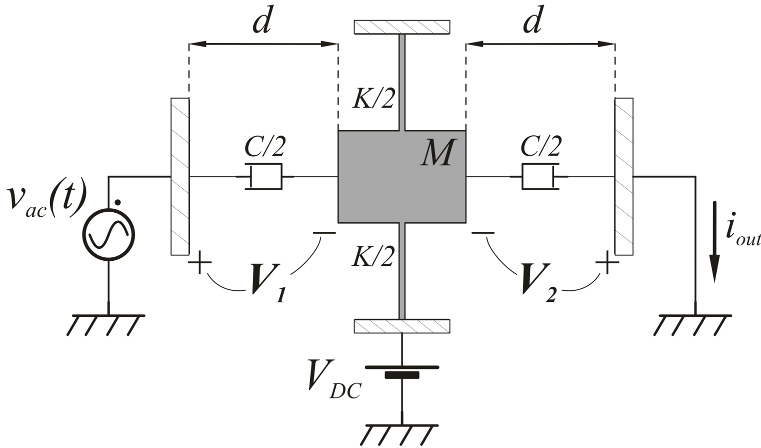

Figure 2.16: two-port scheme.

where the change of sign in the η expression with respect to single port case of equation (2.13) is due to the polarity change caused by the application of the bias voltage on the resonator instead that on the electrodes. The equivalent circuit for the two-port system is shown in figure 2.17. In this circuit the *feedthrough capacitor* C_{ft}, representing the parasitic capacitive coupling between the input and output electrodes, is highlighted. In this new scheme the feedthrough current I_{ft} flowing through C_{ft} takes the place of the static current I_c of the single port scheme. By proper design C_{ft} can be reduced to few femto Farad, with an improvement of several order of magnitude over the motional to parasitic current ratio of the single port scheme. However, even with the two-port scheme the effect of the parasitic current can be very detrimental, especially when the resonator is subjected to hight damping, as in the case when it resonates in air. For this reason, several techniques have been developed in order to cancel the feedthrough contribution: dummy resonator [65], mixing [53], 2nd harmonic driving [66]. When the resonator has more than two electrodes, more complex readout configurations are possible to reduce

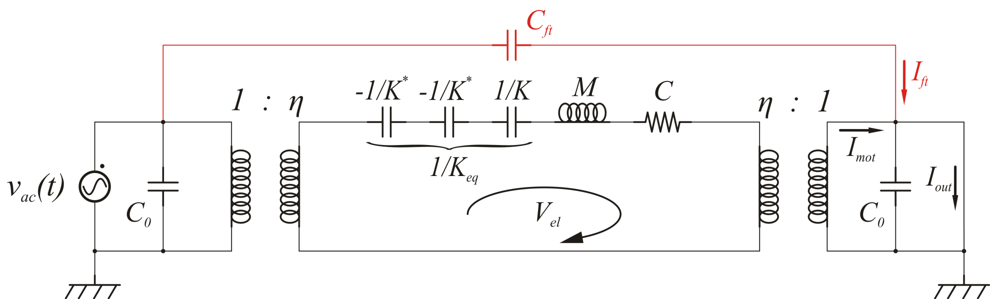

Figure 2.17: Equivalent circuit for the two-port system of figure 2.16.

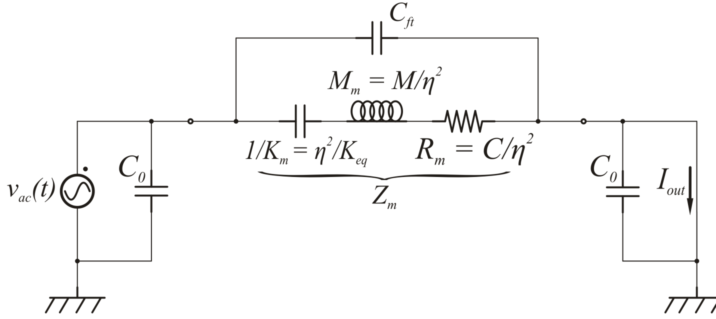

Figure 2.18: Compact representation of the two-port electromechanical transducer equivalent circuit. $Z_m(j\omega) = Y_m(j\omega)^{-1}$ is the resonator equivalent impedance.

the feedthrough current [67, 68, 69]. An often used way to draw the equivalent circuit of figure 2.17 is the compact representation of figure 2.18.

2.2.2 Distributed parameters

In the first part of this section the principles of electrostatic actuation have been exposed. The mechanical part have been modeled with lumped parameters systems, i. e. systems where the mass (and thus the kinetic energy) is concentrated into a rigid block M not allowing deformations, and the stiffness (and thus the potential elastic energy) is concentrated in a block K with no mass. This approximation work well with some MEMS structures such as comb fingers, but the most part of modern MEMS resonators (as well as the ones designed in this thesis) are distributed parameters systems where the kinetic and potential energy are continuously distributed over the resonator volume. In the following the extension of the model to distributed parameters systems will be discussed. A comprehensive dissertation over distributed parameters electromechanics can be found in [64], here the key results of this work will be highlighted. Because it is the most used and simple design, the case of a clamped-clamped beam resonating in-plane will be discussed. However, the presented theory can be extended to all types of resonators with few and easy passages. Moreover, the hole effect won't be taken into consideration and be beam will be considered full. The holes effect will be extensively studied in the following chapter, where an homogenization method will be developed. By means of equivalent parameters, this model will allow the study of the perforated beam with the standard theory for full beams. The most easy and used model for the vibration of beams is Euler-Bernoulli model [70], which is proven to be accurate for slender beams ($w, h \ll L$) over the first resonance frequencies:

$$EI\frac{\partial^4 u(x,t)}{\partial x^4} + \rho A\frac{\partial^2 u(x,t)}{\partial t^2} + c_{1l}\frac{\partial u(x,t)}{\partial t} = p(x,t) \tag{2.28}$$

where $u = u(x,t)$ is the y-coordinate of the deflected principal axis of the beam and

$p(x,t)$ is the force per unit length applied on the beam. Two parameters related to the geometry and material properties of the beam appear in the equation. The first is the bending stiffness EI, the product of the Young's modulus E and the moment of inertia $I = w^3h/12$ of the beam section, with h being the beam thickness; the second is the mass per unit length ρA, with ρ the material density and A the area of the section. Finally c_{1l} is the viscous damping per unit length applied on the beam. When dealing with the resonance frequency problem, the external load $p(x,t)$ and the damping c_{1l} are set to 0. By postulating a solution of the form

$$u(x,t) = U(x)cos(\omega t) \tag{2.29}$$

and substituting (2.29) in (2.28), an ordinary differential equation is obtained:

$$EI\frac{d^4U(x)}{dx^4} - \rho A\omega^2 U(x) = 0 \tag{2.30}$$

By imposing the clamped-clamped boundary conditions:

$$\begin{aligned} U(0) = 0 \qquad & \frac{dU(0)}{dx} = 0 \\ U(L) = 0 \qquad & \frac{dU(L)}{dx} = 0 \end{aligned} \tag{2.31}$$

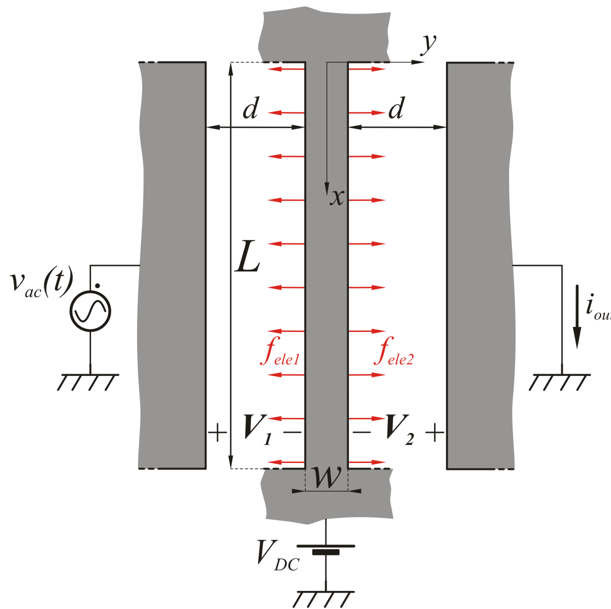

Figure 2.19: Clamped-clamped beam resonator with two-port electrostatic actuation.

n	z_n
1	4.73
2	7.85
3	11
4	14.14

Table 2.2: First four roots of the clamped-clamped eigenvalue equation (2.33).

the resonance mode shapes are found:

$$U_n(x) = U_0 \left\{ \cosh\left(\frac{x}{L} z_n\right) - \cos\left(\frac{x}{L} z_n\right) + \frac{\cosh(z_n) - \cos(z_n)}{\sinh(z_n) - \sin(z_n)} \cdot \right.$$

$$\left. \cdot \left[\sin\left(\frac{x}{L} z_n\right) - \sinh\left(\frac{x}{L} z_n\right) \right] \right\} \tag{2.32}$$

where U_0 is an arbitrary real constant and z_n are the solutions of the eigenvalue equation:

$$\cosh(z)\cos(z) - 1 = 0 \tag{2.33}$$

The first four roots of this equation are reported in table 2.2, while the corresponding eigenmodes are shown in figure 2.20. Finally, the resonance pulsations are found to be:

$$\omega_n = \sqrt{\frac{EI{z_n}^4}{\rho A L^4}} \tag{2.34}$$

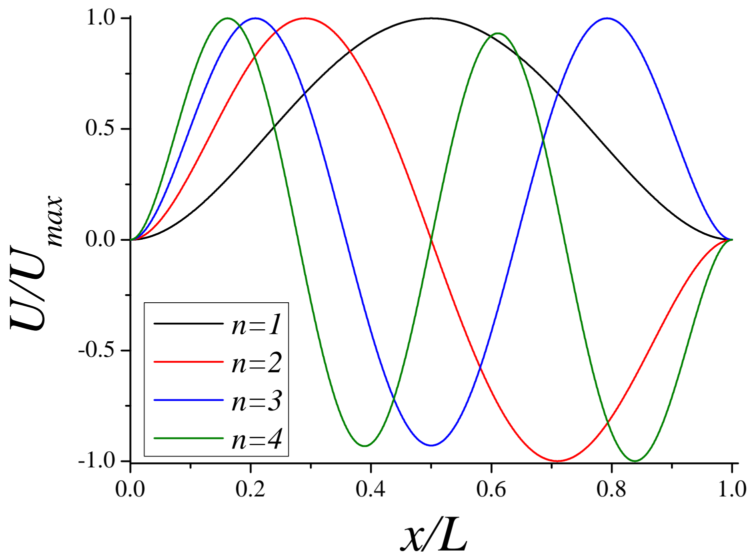

Figure 2.20: First four mode shapes of the clamped-clamped beam.

The mode shapes $U_n(x)$ are orthogonal functions:

$$\int_0^L U_n(x)U_m(x)\,dx = {U_0}^2 L\delta_{nm} \tag{2.35}$$

and form a complete set, they can thus be used as a basis:

$$u(x,t) = \sum_{m=1}^{\infty} U_m(x) f_m(t) \tag{2.36}$$

where $f_m(t)$ is the generalized time-dependent coordinate relative to the *m-th* mode. Substituting (2.36) in (2.28):

$$\sum_{m=1}^{\infty}\left(EI\frac{d^4U_m(x)}{dx^4}f_m(t) + \rho A\ddot{f}_m(t)U_m(x) + c_{1l}\dot{f}_m(t)U_m(x)\right) = p(x,t) \tag{2.37}$$

where the time derivative have been shown with dots. By using (2.30) the first term in the summation can be rewritten:

$$\sum_{m=1}^{\infty}\left(\rho A{\omega_m}^2U_m(x)f_m(t) + \rho A\ddot{f}_m(t)U_m(x) + c_{1l}\dot{f}_m(t)U_m(x)\right) = p(x,t) \tag{2.38}$$

by multiplying for $U_n(x)\,dx$ and integrating over the beam length an infinite set of uncoupled equations is found:

$$k_nf_n(t) + m_n\ddot{f}_n(t) + c_n\dot{f}_n(t) = \int_0^L U_n(x)p(x,t)\,dx \qquad n = 1...\infty \tag{2.39}$$

where the dynamic spring k_n, mass m_n and damping coefficient c_n, relative to the *n-th* mode have been defined:

$$\begin{aligned} m_n &= \rho AL{U_0}^2 \\ k_n &= m_n{\omega_n}^2 \\ c_n &= c_{1l}L{U_0}^2 \end{aligned} \tag{2.40}$$

As it can be seen from the relationships 2.40, for the particular case of clamped-clamped beams, the modal mass an damping coefficients are equal to their total values. The applied force per unit length can be written as:

$$\mathbf{p}(x,t) = \mathbf{f_{ele1}}(x,t) + \mathbf{f_{ele2}}(x,t)$$

$$= -\frac{\epsilon_0 h{\mathbf{V_1}}^2}{2(d+\mathbf{u}(x,t))^2} + \frac{\epsilon_0 h{\mathbf{V_2}}^2}{2(d-\mathbf{u}(x,t))^2} \tag{2.41}$$

following the same approach, $\mathbf{p}(x,t)$ has to be linearized in $\mathbf{u}(x,t)$=0, $\mathbf{V_1}$=$-V_{DC}$ and $\mathbf{V_2}$=$-V_{DC}$. The obtained small signal force per unit length:

$$p(x,t) = \frac{\epsilon_0 h V_{DC}}{d^2} v_{ac}(t) + \frac{\epsilon_0 h {V_{DC}}^2}{d^3} u(x,t) \tag{2.42}$$

By substituting (2.42) into (2.39) and using the factorization (2.36) for expressing $u(x,t)$:

$$k_n f_n(t) + m_n \ddot{f}_n(t) + c_n \dot{f}_n(t) = \underbrace{-\frac{\epsilon_0 h V_{DC}}{d^2} \int_0^L U_n(x)\,dx}_{\eta_n} \; v_{ac}(t)$$

$$+ \underbrace{\frac{\epsilon_0 h {V_{DC}}^2}{d^3} {U_0}^2}_{2{k_n}^*} f_n(t) \qquad n = 1 \ldots \infty \tag{2.43}$$

where the electromechanical coupling coefficient relative to the *n-th* mode η_n, and the spring softening constant relative to the same mode ${k_n}^*$ have been defined. In order to link equation (2.43) to the concentrated parameter model, it is rewritten in the frequency domain with the modal velocity $V_{el_n}(t)$ = $\dot{f}_n(t)$ as the unknown:

$$j\omega m_n V_{el_n}(j\omega) + c_n V_{el_n}(j\omega) + \frac{k_n - 2{k_n}^*}{j\omega} V_{el_n}(j\omega) = \eta_n V_{ac}(j\omega) \qquad n = 1 \ldots \infty \tag{2.44}$$

This expression is formally identical to the lumped parameter equation (2.14) and thus leads to the equivalent circuits for two-port systems 2.17 and 2.18. At this point it is important to remark that the lumped parameter system is represented by an infinite set of these equation, one for each mode, therefore the complete circuit will be the parallel of an infinite series of concentrated-like circuit, one for each set of modal parameters η_n, m_n, k_n and c_n [64]. However, if the quality factor is big enough and the resonances are well spaced in frequency (as is typically verified in MEMS resonators), in the neighborhoods of each mode the system can be studied considering only the circuit relative to that mode. This simplification will be used in the following of this work to study the resonance of two types of lumped parameters resonators vibrating in their first resonance mode. Finally it is useful to get a simplified expression for η_1 by computing the integral over the first mode shape:

$$\eta_1 = \frac{\epsilon_0 h V_{DC}}{d^2} \int_0^L U_1(x)\,dx = 0.83 \frac{\epsilon_0 h L V_{DC}}{d^2} U_0 \tag{2.45}$$

this expression is similar to the one of the lumped parameter system, the 0.83 coefficient takes into account the fact that the electrode does not translate rigidly as in the case of concentrated parameter systems. The U_0 constant appears in each dynamic parameter and not affect any physic quantity of interest. In the following will be always assumed $U_0 = 1$.

2.3 Limit of detection

In this section the limit of detection (LOD) of a resonant sensor, i.e. the minimum detectable mass concentration μ_{min}, will be investigated. A first qualitative discussion will be aimed at identifying the resonant sensors parameters affecting LOD. Thereafter, a more detailed analysis, assuming that the resonator is read by means of an electronic oscillator, which is a very efficient and frequently applied method to detect the resonance frequency, will be done. Even if it will not be supported by experimental results in this thesis, this latter readout approach has to be considered the final step of an ideal sensing system and the most interesting from a Point-Of-Care application point of view [29].
LOD estimation allows a more fair comparison than the sensitivity, since it is common to all the types of sensors discussed in chapter 1 (see figure 1.7). Furthermore it is the most important parameter from an application point of view: considering the typical example where the analyte concentration beyond a certain limit is considered as indicator of a possible disease, the suitable detector needs, as a first and essential characteristic, a LOD below, or at least equal to this limit. The limit of detection of a generic sensor is usually limited by the background noise which is always present in the output signal. Noise analysis is a key task in many applicative fields of physics and many analytical models have been developed in order to study this phenomenon. Because of the complexity of the argument, simple analytical models can only work as qualitative esteems of the real situation, and in the case of resonant sensors there are some additional issues which will be shortly addressed in the following. The meaningful noise of a resonant sensor is the noise that affect the measure of the resonance frequency, this makes the noise estimation strongly dependent from the measurement scheme. A first measurement scheme has been described in section 2.2 with the two-port electrostatic configuration of figure 2.11: the frequency of the small signal source is swept in the neighborhood of the resonance frequency and the resonator frequency response (i. e. the total transconductance Y_t) is acquired. The motional current is extracted from the total signal (if necessary) and the resonance frequency is usually obtained through a nonlinear fitting. This configuration is somewhere called open loop configuration in order to highlight its difference from the closed loop configuration that will be described in the following of this section. The open loop configuration is often exploited in the preliminary characterization of the resonance sensors [71], but it is not well suited from an application point of view, since it is time-consuming and requires complex laboratory instrumentation (a network analyser) to be performed. Some qualitative considerations on the limit of detection can be done considering the example of figure 2.21, where the resonant peaks of two resonators (identified with the subscripts a and b), have been acquired before (solid lines) and after (dashed lines) the exposition to the target analyte. The peaks are also normalized to their respective motional resistance r_m. To make a fair comparison, the resonance frequency before exposition, and the added mass per unit surface are considered equal. Resonator a has a sensitivity 10 times bigger than resonator b, thus the output quantities, i. e. the fractional frequency shifts y_a and y_b, will be subject to the same relationship:

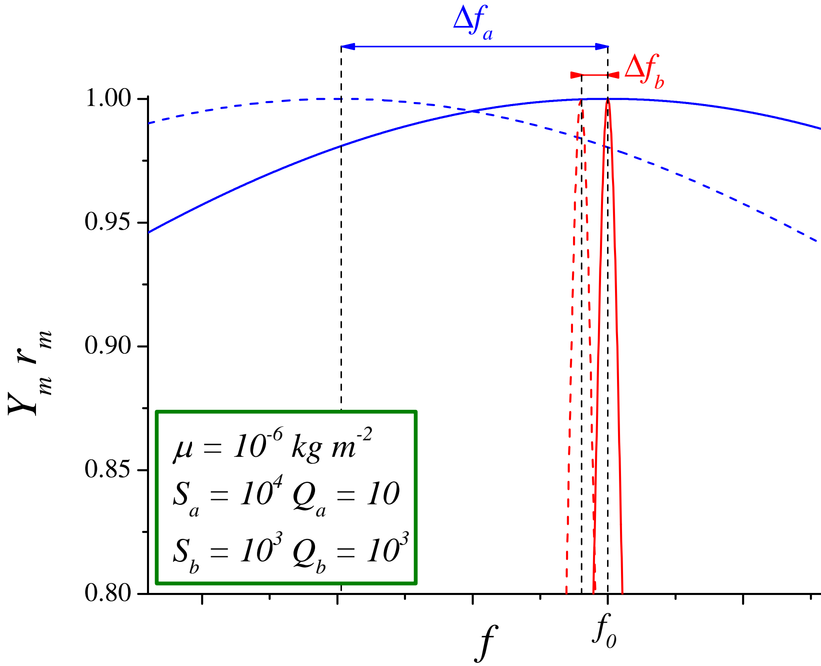

Figure 2.21: Comparison between two resonant sensors whose peaks are acquired before (solid lines) and after (dashed lines) the exposition to the target analyte. Assuming the same resonance frequency before exposition and the same added mass concentration, effects of different sensitivity and quality factor are shown.

$$y_a = \frac{\Delta f_a}{f_0} = 10\, y_b \tag{2.46}$$

However, resonator a has a quality factor Q_a 100 times smaller than Q_b. In the real case where fluctuations due to noise are present on the peaks, detecting the resonance peak shift of resonator a may be complicated or even impossible. On the other hand, the 100 times smaller width at half maximum of resonator b facilitates interpretation of frequency shifts since sharper peaks allow higher resolution of peak frequency shifts. Assuming small shifts, the peak amplitude in the neighborhood of f_0 can be approximated as:

$$|Y_m(f_0 + \Delta f_0)| \simeq |Y_m(f_0)| - \frac{2Q^2}{r_m}\left(\frac{\Delta f_0}{f_0}\right)^2 \tag{2.47}$$

If noise limits the minimum detectable change in the amplitude of the motional transconductance to Y_{min}, the minimum detectable fractional frequency shift can be written as:

$$y_{0_{min}} = \frac{1}{Q}\sqrt{\frac{Y_{min} r_m}{2}} \tag{2.48}$$

The minimum detectable mass concentration μ_{min} will be the one resulting in this minimum detectable fractional frequency shift. Therefore the resonator parameters affecting

the limit of detection:

$$\mu_{min} \propto \frac{\sqrt{r_m}}{QS_c} \tag{2.49}$$

As it was expected form the previous discussion on the example of figure 2.21, both Q and S_c appear in equation (2.49) as inversely proportional parameters with respect to μ_{min}. The effect of the motional resistance r_m cannot be appreciated since the peaks were normalized, however, a lower r_m results in a bigger oscillation amplitude and thus in a less detrimental effect of noise over the acquired peak. As it will be argued in the following, where a more detailed analysis of LOD assuming a readout using an oscillator will be done, oscillations amplitude in MEMS-based oscillators is not a factor concerning the resonator, since it is typically limited by the electronics. In this case, even if not affecting LOD, having a small r_m is still valuable, since it relaxes the constraint the electronics has to meet in order to sustain oscillation.

The most easy and used method to read a resonant sensor is to insert it into a feedback loop with an electronic amplifier. The energy lost through the several dissipation mechanisms of the resonator (such as the viscous damping discussed in section 2.2) is resupplied by the active electronics and steady-state oscillations are allowed in the loop. Such a circuit is often called MEMS oscillator, because it is simply an electronic oscillator where the frequency selective part, usually an L-C tank, has been replaced by the MEMS resonator whose resonance peak works as the frequency selective part. This type of configuration is very attractive since the sustaining electronics is amenable of monolithic integration with the MEMS resonator and the device can be read with only a frequency counter. If the resonator is actuated with the two-port electrostatic method

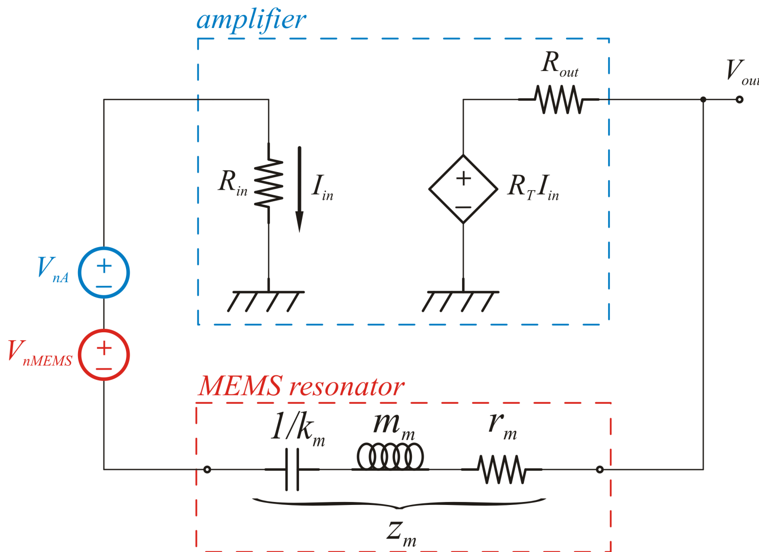

Figure 2.22: Schematic of a MEMS oscillator employing a transresistive amplifier.

described in 2.2, the natural choice is to use a transresistive amplifier as shown in figure 2.22. In this schematic the resonator is represented using the compact circuit of figure 2.18, with the static and feedthrough capacitances assumed negligible for simplicity, the transresistive amplifier is assumed to have a bandwidth at least 10 times bigger than the resonator resonance frequency f_0, and thus its input and output impedances can be approximated with the resistors R_{in}, R_{out}, and the transresistive gain with a real constant R_T. The frequency noise of an oscillator is directly related to the phase noise, which is the quantity commonly used to evaluate frequency stability of oscillators. As an example, the GSM standard establishes a limit of $-130\,\mathrm{dB/Hz}$ at an offset of $1\,\mathrm{kHz}$ from the carrier. Kaajakari [72] realized the first MEMS oscillator meeting the GSM specification. Phase noise is a consequence of the various noise sources present in the feedback loop. In a MEMS oscillator these noise sources can be ascribed to the sustaining electronics or to the MEMS resonator. In the schematic these sources are modeled with two noise generators: V_{n-A} for the amplifier and V_{n-MEMS} for the resonator. The amplifier noise will have its thermal and noise terms, while the MEMS noise has several contributions arising from different phenomenons [73]: thermal fluctuations, thermoelastic noise, momentum exchange with the surrounding gas molecules, adsorption desorption processes. However, in almost all practical cases it has been found that the noise from the amplifier is the dominant contribution [74, 75, 76]. The phase noise theory tries to relate these contributions to the instability of the oscillation frequency. This theory is relatively young and in the last years numerous models have been proposed to explain some dark points of the classical approach [77, 78, 79]. However, the very general results that are of interest for this work are proved and common to all these models. In the following, the basic points of the classical phase noise theory will be discussed, for a comprehensive treatise the reader is referred to the various references already and subsequently cited in this section. Considering the oscillator of figure 2.22, the open loop gain βA is found to be:

$$\beta A(j\omega) = \frac{R_T}{R_{in} + R_{out} + Z(j\omega)} \tag{2.50}$$

in order allow the growing of oscillations at f_0, βA has to meet the triggering Barkhausen conditions at this frequency:

$$|\beta A(j\omega_0)| \geq 1 \qquad\qquad \phi(\beta A(j\omega_0)) = 0 \tag{2.51}$$

the phase condition is already verified at f_0, since $\phi(Z(j\omega_0)) = 0$. To verify the amplitude condition the transresistive gain has to be:

$$R_T \geq R_{in} + R_{out} + r_m \tag{2.52}$$

A good transresistive amplifier should have negligible imput and output resistances with respet to the resonator motional resistance. This means that the amplifier does not add significative loss mechanism in the loop, and equation (2.52) simply states that the amplifier has to overcome the resonator losses. As the oscillations increase in amplitude,

some effect lowers the open loop gain until it equals unity, i. e. the equality in (2.52) is verified:

$$R_T = R_{in} + R_{out} + r_m \tag{2.53}$$

this is also called steady-state Barkhausen condition. Once this condition is verified, oscillations amplitude non longer grows and steady-state oscillations last indefinitely in the circuit. The βA lowering effect can be due to an automatic gain control circuit, amplifier nonlinearities (R_T reduction) or resonator nonlinearities (r_m increase). By basic circuit analysis the noise voltage at the oscillator output can be written as:

$$V_{n-out} = \frac{R_T - R_{out}}{R_{in} + R_{out} + Z(j\omega) - R_T} \left(V_{n-A} + V_{n-MEMS}\right) \tag{2.54}$$

In steady-state operation equation (2.53) holds true and the denominator of (2.54) diverges at the resonance frequency, the noise is thus shaped with a very high, ideally infinite peak centered at f_0. For this reason, the effect of noise is significant only for components close to the resonance frequency and it is usually expressed as a function of the frequency offset Δf from the frequency of the carrier f_0. For $\Delta f \ll f_0$ the resonator impedance can be approximated as:

$$Z(j\omega_0 + \Delta\omega) = r_m + j2m_m\Delta\omega \tag{2.55}$$

Substituting (2.53) and (2.55) in (2.54), and considering $R_{in} \ll r_m$, an expression for the noise voltage at an offset Δf from the oscillation frequency is found:

$$V_{n-out}(j\Delta f) = \frac{f_0}{j2Q\Delta f} \left(V_{n-A} + V_{n-MEMS}\right) \tag{2.56}$$

where Q is the resonator quality factor (see (2.21), (2.22) and (2.23)). As it was already discussed, is reasonable to assume that the amplifier noise is the dominant term, with this assumption the noise spectral density of the output voltage is:

$$S_{V_{n-out}}(\Delta f) = \left(\frac{f_0}{2Q\Delta f}\right)^2 S_{V_{n-A}}(\Delta f) \tag{2.57}$$

For typical values of the resonance frequency the amplifier power spectral density $S_{V_{n-A}}$ can be considered white ($S_{V_{n-A0}}$) in the neighborhood of f_0, a schematic of the oscillator shaping effect over the amplifier noise is shown in figure 2.23. In order to understand how this voltage noise impacts the stability of the oscillation frequency, it is customary to consider a $1\,\mathrm{Hz}$ bandwidth centered at an offset Δf for the carrier and model it as sinusoid with amplitude set such that it has the same power as the noise it represents and random phase. This is a good approximation as long as long the signal is observed for a time substantially less than one second. For a complete treatise of narrow band noise representation, refer to [80]. Assuming a steady-state oscillation of amplitude V_M, the total output signal with the above described noise component is:

$$V_{out} = V_M sin(\omega_0 t) + A_n sin\left[(\omega_0 + \Delta\omega)t + \psi_n\right] \tag{2.58}$$

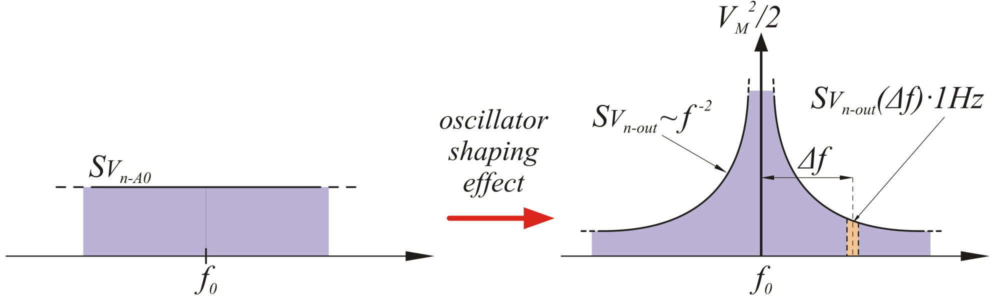

Figure 2.23: Noise shaping due to the oscillator. The signal power, represented with a delta function of area $V_M^2/2$ is also shown. The noise power in a $1\,Hz$ bandwidth, centered at a frequency offset Δf from f_0 is highlighted.

where ϕ_n is the random phase and A_n is set by (2.57):

$$\frac{{A_n}^2}{2} = S_{V_{n-out}}(\Delta f) \cdot 1\,Hz = \left(\frac{f_0}{2Q\Delta f}\right)^2 S_{V_{n-A0}} \tag{2.59}$$

Using trigonometric transformations equation (2.58) can be rewritten as:

$$\begin{aligned} V_{out} &= V_M sin(\omega_0 t) + A_n \left[\sin(\omega_0 t)\cos(\Delta\omega t + \psi_n) + \cos(\omega_0 t)\sin(\Delta\omega t + \psi_n)\right] \\ &= \underbrace{\left[V_M + A_n\cos(\Delta\omega t + \psi_n)\right]}_{P(t)}\sin(\omega_0 t) + \underbrace{A_n\sin(\Delta\omega t + \psi_n)}_{Q(t)}\cos(\omega_0 t) \\ &= \sqrt{P(t)^2 + Q(t)^2}\,\sin\left[\omega_0 t + \arctan\left(\frac{Q(t)}{P(t)}\right)\right] \end{aligned} \tag{2.60}$$

with the last equality, noise contribution to amplitude and phase fluctuations have been divided. Amplitude noise in typically not important because is cancelled by the amplitude limit mechanism, phase noise instead is the interesting quantity, assuming $A_n \ll V_M$ the phase fluctuation $\phi(t)$ can be approximated:

$$\begin{aligned} \phi(t) &= \arctan\left[\frac{A_n\sin(\Delta\omega t + \psi_n)}{V_M + A_n\cos(\Delta\omega t + \psi_n)}\right] \\ &\simeq \arctan\left[\frac{A_n\sin(\Delta\omega t + \psi_n)}{V_M}\right] \\ &\simeq \frac{A_n\sin(\Delta\omega t + \psi_n)}{V_M} \end{aligned} \tag{2.61}$$

Using (2.59) the phase noise power spectral density can be written:

$$S_\phi(\Delta f) = \frac{1}{2}\frac{{A_n}^2}{{V_M}^2} = \left(\frac{f_0}{2V_M Q \Delta f}\right)^2 S_{V_{n-A0}} \tag{2.62}$$

With the last equation, the so called *Leeson's model* for phase noise has been derived. Expression (2.62) is often reported multiplied by a factor two in order to express a single side band noise spectral density. *Leeson's model* predicts a Δf^{-2} behavior of phase noise in the neighborhood of f_0, failing to predict the experimentally observed Δf^{-3} behavior at low offsets. A recently accomplished model that explains the low offset behavior is the time-dependent model of Hajimiri and Lee [78]. However, the key result of the *Leeson's model*, i. e. the inverse dependency of the phase noise from V_M and Q, has been proven also in the Δf^{-3} region. To relate the phase noise to the frequency fluctuations one last step is needed, the fractional frequency shift can be written as:

$$y_0(t) = \frac{f(t) - f_0}{f_0} = \frac{1}{f_0}\frac{d\phi(t)}{dt} \tag{2.63}$$

ant thus the power spectral density of the fractional frequency shift:

$$S_{y_0}(\Delta f) = \frac{\Delta f^2}{{f_0}^2} = S_\phi(\Delta f) = \left(\frac{1}{2V_M Q}\right)^2 S_{V_{n-A0}} \tag{2.64}$$

Equation (2.64) describes the oscillator fractional frequency noise in the frequency domain. The transition to the time domain noise description is not straightforward in frequency measurement, since the classical statistical tools (classical variance) have found to have a divergent behavior [81, 82]. For this reason, alternative statistical tools have been developed, among them *Allan variance* is the most used. For the white fractional noise of equation (2.64) the Allan standard deviation (the square root of the variance) is [81, 82]:

$$\sigma_{y_0} = \frac{1}{2}\frac{1}{2V_M Q}\tau^{-1}\sqrt{S_{V_{n-A0}}} \tag{2.65}$$

where τ is the observation time. σ_{y_0} can be taken as an estimator of the minimum detectable fractional frequency shift due the analyte binding. Therefore, an estimator for the minimum detectable mass concentration μ_{min} is found considering the mass concentration that results in this minimum detectable frequency shift:

$$\mu_{min} \sim (S_c V_M Q)^{-1} \tag{2.66}$$

The discussion expounded in this section should be intended as a qualitative exposition of the frequency noise mechanisms in a MEMS oscillator and thus far away from giving reliable values for the minimum detectable mass concentration μ_{min}. However, with equation (2.66), the important result of highlighting the oscillator parameters that affect LOD is reached and the product $S_c V_M Q$ can be used as merit parameter for the comparison of various design. If the mass sensitivity S_c and the quality factor Q are clearly resonator parameters, some further considerations are needed for the oscillation amplitude V_M. As it was previously outlined, V_M can be limited by either amplifier or resonator nonlinearities. Resonator nonlinearities are affected by the power handling capability, which is the

ability of the resonator material to store energy without falling into nonlinear regime (material nonlinearities). For this reason, oscillators with MEMS-limited amplitudes are often observed when the resonator dimensions are scaled towards micron or tens of microns scale [75, 83]. Other situations that typically contribute in the early arise of material nonlinearities are the operation under vacuum and electrostatic actuation gaps in the order or below 200 nm. Another documented issue arises from electrostatic actuation which is inherently nonlinear (see the non-linearized relationship between force and displacement of equation (2.11)). This electrostatic nonlinearity add another amplitude limit that may be lower than the one fixed by mechanical nonlinearities. Moreover, electrostatic nonlinearity involves a folding effect over the amplifier flicker noise, which generates a Δf^{-3} region at low offsets from the oscillation frequency, however, this effect is found to be important only with very narrow actuation gaps ($d < 200\,\mathrm{nm}$) [84, 85]. In this work, resonators operating at ambient pressure, with typical dimensions in the order of several hundreds of microns and actuation gaps ranging in the micrometer scale, are considered. For these reasons, is reasonable to consider the sustaining electronics as the amplitude limiting part. Form the resonator point of view the merit parameter related to the limit of detection is the product $S_c Q$. Finally it is worth to point out that drawing the holes pattern on the resonator probably has a detrimental effect on its power handling capability, this effect needs an experimental evaluation.

2.4 Air damping limited quality factor

In the discussion expounded in the previous sections of this chapter, the quality factor Q emerged as key parameter of the resonant sensor. The advantages of having an high quality factor will be shortly recalled in the following, thereafter the discussion will be focused on the air damping, which is the main loss mechanism, and thus the one limiting Q, for MEMS resonators operating at ambient pressure. As it will be argued in the following, the operation at ambient pressure is the most interesting case for resonant sensors. For this reason, the devices presented in this thesis will be assumed to work in air. Air damping in MEMS can be divided in slide and squeeze film damping, analytical models working as rough estimators of the damping coefficients will be given for both these cases. Finally some considerations over the effect of the holes pattern on the quality factor will be done. In section 2.2 a first definition for Q has been given assuming a concentrated parameter system (equations (2.22), (2.21) and (2.23)). For a lumped resonator Q can be expressed using equation (2.22) and the dynamic parameters (2.40):

$$Q = \frac{m\omega_0}{c} \tag{2.67}$$

where the resonance mode number subscripts have been omitted. Using equation (2.24) the motional resistance can be shown to be inversely proportional from Q:

$$r_m = \frac{m\omega_0}{\eta^2 Q} \tag{2.68}$$

An high value of Q results in a low motional resistance and thus in a better motional to parasitic current ratio. As can be seen from figure 2.24, an high quality factor also results is a narrow peak (see (2.23)). As it has already been argued in sections 2.2 and 2.3, both these properties have a fundamental and positive effect over resonance frequency measure and limit of detection with the two-port open loop setup of figure 2.11. These advantages have also shown to well translate in the closed loop setup of figure 2.22: the low motional resistance results in a less stringent constraint on the amplifier (equation (2.52)), which can entail a reduction in power consumption, area occupation and amplifier noise. The narrow peak results in even a more narrow frequency shaping from the oscillator, which finally entails the presence of the quality factor among the three parameters affecting the limit of detection (equation (2.66)). Towards a more general vision, having an high Q implies key advantages in all resonator applications, besides resonant sensors, the most common applications involving MEMS/NEMS resonators are: AFM probes [86], filters [87, 88, 89], oscillators for timekeeping and radiofrequency applications [90], accelerometers and gyroscopes [91]. It can be concluded that the pursuit of ultrahigh quality factors underlies almost all research in MEMS and NEMS resonators [92]. By looking at equation (2.67) it is clear that the problem of Q estimation is essentially a problem of damping estimation. In section 2.2 the dynamic damping coefficient c is a consequence of the viscous damping taking place along the beam, in a more general case c is simply a loss coefficient that takes into account several losses mechanism present in the resonator:

$$c = \sum c_i \tag{2.69}$$

Among the most common and studied loss mechanism in MEMS are: thermoelastic damping (TED) [93], clamping losses [94], surface losses [95], viscous damping in air and fluid (see below), Akaiser and other quantum effects [96, p.287]. Substituting (2.69) in (2.67) the quality factor can be written as:

$$\frac{1}{Q} = \sum \frac{1}{Q_i} \tag{2.70}$$

where Q_i is the quality factor that the device would have if only the *i-th* loss mechanism would take place in the resonator. In most of the cases there is a dominating loss mechanism that makes the other effects negligible:

$$Q \simeq Q_i \tag{2.71}$$

thus, for an accurate estimation of the quality factor, an accurate model for the dominating loss mechanism is needed. The resonant sensors considered in this work have to be exposed to the analyzed environment or biological sample. For this reason, in order to maintain assay simplicity, at least the work at ambient pressure is required. Otherwise one would have to expose the sensor, dry it if the analyte is in a liquid environment, put it into a vacuum chamber, wait for the desired pressure level and perform the measure. If the labelling step of the fluorescence method has been stigmatized has a time-consuming and labor-intensive process, the above described assay does not seem to be so different. By making the sensor work in air at least the final and more time-consuming steps can be

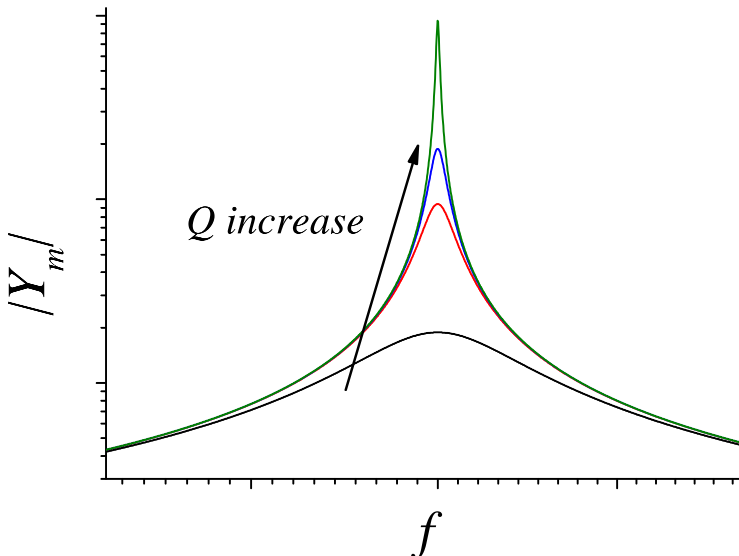

Figure 2.24: Motional transconductance with varying of the quality factor.

avoided and the vacuum chamber is not necessary. Clearly, the final and most attractive step is to let these sensors work in liquid environment. Several research groups have been moving towards this objective [97]. However, this section is limited to the study of the work in air. When a MEMS resonator vibrates in air, the dominating loss mechanism is the viscous damping that the device experience during its movement in the surrounding fluid. This effect is typically referred as *air damping*. In the following of this section, a short introduction to the air damping of MEMS structures will be given. For a complete treatise of this argument, the reader is referred to the several works that will be cited during the exposition. The problem of the estimation of the viscous force acting on a moving structure surrounded by a viscous fluid, is basically the problem of solving the displacement field of the fluid in the neighborhood of this structure. If the fluid can be considered as a continuum, the equations of motion are the Navier-Stokes equations [98]. Closed form solutions for these equations are still an ongoing challenge, approximate solutions, based on rough simplifications are the basis of the models used today for modelling the gas damping in MEMS. Another problem is strictly related with the micrometric scale of MEMS devices: when the devices feature sizes are comparable with the mean free path of the gas molecules, the fluid cannot be considered as a continuum anymore, and thus molecular models have to be used in order to solve the displacement field. The transition from the continuum to the molecular regime is not abrupt, based on the Knudsen number, it is customary to define four regions of work. The Knudsen number is defined as:

$$K_n = \frac{\lambda_f}{d} \tag{2.72}$$

where λ_f is the mean free path of the fluid molecules at the working pressure and temperature, and d is the characteristic length of the problem. The regions of work are:

$$\begin{aligned} K_n &< 10^{-2} && \textit{continuum regime} \\ 10^{-2} \leq K_n &\leq 10^{-1} && \textit{slip flow regime} \\ 10^{-1} \leq K_n &\leq 10 && \textit{transition regime} \\ K_n &> 10 && \textit{free molecular regime} \end{aligned} \tag{2.73}$$

The mean free path of air at ambient pressure and room temperature is $\lambda_f = 68\,\mathrm{nm}$, for a characteristic length in order of few micrometers the problem falls into the *slip flow regime*. In this working region, Navier-Stokes equations are still assumed to be valid, but ad-hoc boundary conditions (first or higher order slip boundary condictions) are used in order to take into account the effects of rarefaction. Air damping in MEMS can be divided in two main categories: slide and squeeze film damping. In the following a brief formulation of these problems and the expressions of the damping coefficients will be given.

2.4.1 Slide film damping

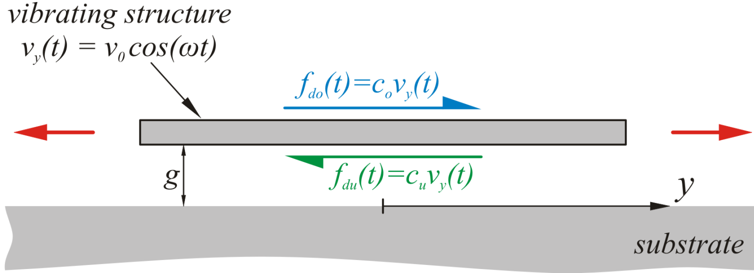

Figure 2.25: Schematic of the slide film damping. ν_y is the velocity of the vibrating structure. f_{do} and f_{du} are the viscous damping forces acting on the upper and lower surfaces respectively, c_0 and c_u are their proportionality coefficients with respect to ν_y.

Slide film damping takes place over structures translating in parallel with the substrate, as in figure 2.25. The fluid in contact with the upper and lower moving surfaces starts moving too and the velocity field penetrates in the surrounding fluid. Part of the vibratory energy of the structure is thus transferred to the fluid in form of kinetic energy, revealing a loss mechanism. By solving the velocity field in the surrounding of the structure, the viscous damping forces f_{do} and f_{du}, that the fluid exercises over the upper and lower surfaces can be calculated. The presence of the substrate a few micrometers far from the lower surface may influence the velocity field of the fluid underneath the structure, therefore the problem has to be divided in slide under and over the structure. The details about the mathematical approach and the solution of this problem can be found in [99] and [100, p.150] (continuum regime), [101] (slip regime with first and higher order boundary conditions) and [102] (numerical methods). The slide damping coefficient per unit surface under the structure, using first order slip boundary conditions is [101]:

$$c_{u-1s} = \frac{\sqrt{R_{ey}}\mu}{\sqrt{2}g} \cdot \frac{\sinh\left(\sqrt{2R_{ey}}\right) + \sin\left(\sqrt{2R_{ey}}\right) + k_1}{\cosh\left(\sqrt{2R_{ey}}\right) - \cos\left(\sqrt{2R_{ey}}\right) + k_2} \tag{2.74}$$

where R_{ey} is the Reynholds number, defined as:

$$R_{ey} = \frac{g\omega^2}{\nu} \tag{2.75}$$

with $\nu = \mu/\rho_f$ being the kinematic viscosity, defined as the ratio of the dynamic viscosity μ and the fluid density ρ_f. The coefficients k_1 and k_2 can be expressed as two functions of R_{ey} and K_n:

$$
\begin{aligned}
k_1 = & -3R_{ey}\sin\left(\sqrt{2}\sqrt{R_{ey}}\right)K_n^2 + 3R_{ey}\sinh\left(\sqrt{2}\sqrt{R_{ey}}\right)K_n^2 \\
& + \sqrt{2}\sqrt{R_{ey}}\left(2 - K_n^2 R_{ey}\right)\cos\left(\sqrt{2}\,\sqrt{R_{ey}}\right)K_n \\
& + \sqrt{2}\sqrt{R_{ey}}\left(R_{ey}K_n^2 + 2\right)\cosh\left(\sqrt{2}\sqrt{R_{ey}}\right)K_n
\end{aligned} \tag{2.76}
$$

$$
\begin{aligned}
k_2 = & R_{ey}\left(4 - K_n^2 R_{ey}\right)\cos\left(\sqrt{2}\sqrt{R_{ey}}\right)K_n^2 \\
& + R_{ey}\left(R_{ey}K_n^2 + 4\right)\cosh\left(\sqrt{2}\sqrt{R_{ey}}\right)K_n^2 \\
& + 2\sqrt{2}\sqrt{R_{ey}}\left(1 - K_n^2 R_{ey}\right)\sin\left(\sqrt{2}\,\sqrt{R_{ey}}\right)K_n \\
& + 2\sqrt{2}\sqrt{R_{ey}}\left(R_{ey}K_n^2 + 1\right)\sinh\left(\sqrt{2}\sqrt{R_{ey}}\right)K_n
\end{aligned} \tag{2.77}
$$

The slide damping coefficient per unit surface over the structure can be simply obtained by taking the limit $g \to \infty$:

$$
c_{o-1s} = \lim_{g\to\infty} c_{u-1s} = \frac{\mu(2\lambda_f\rho_f\omega + \sqrt{2\mu\rho_f\omega})}{2(\mu + \lambda_f(\lambda_f\rho_f\omega + \sqrt{2\mu\rho_f\omega}))} \tag{2.78}
$$

The damping coefficients in the continuum region can also be obtained by considering $\lambda_f = 0$ in the slip flow expressions. In the expression (2.78) of the damping coefficient over the structure this substitution is straightforward, for the coefficient under the structure gives $K_n = 0$ and thus $k_1 = k_2 = 0$ in equation (2.74).

2.4.2 Squeeze film damping

Squeeze film damping is typical of electrostatic actuated resonators, where the structure oscillates in the direction of a fixed electrode, as shown in figure 2.26. The volume between the structure and the fixed electrode changes with time and part of the fluid is squeezed in and out of this volume. Part of the vibratory energy is thus lost in the fluid motion and the effect is modeled with a squeeze film damping coefficient. Detailed expositions about the mathematical approach to the squeeze film damping problem can be found in [100, p.124] and [103]. The squeeze film damping coefficient for a rectangular plate with in-plane dimensions L, h and a distance d from the fixed electrode is:

$$
c_{sqz} = \frac{64P_a hL\sigma}{\pi^6 d\omega}\sum_{n,m\ odd}\frac{m^2 + \left(\frac{n}{\eta}\right)^2}{m^2n^2\left\{\left[m^2 + \left(\frac{n}{\eta}\right)^2\right]^2 + \frac{\sigma^2}{\pi^4}\right\}} \tag{2.79}
$$

where P_a is the pressure at the edges of the squeezed volume, $\eta = L/h$ is the aspect ratio of the moving plate and σ is the squeeze number:

$$
\sigma = \frac{12h^2\mu_{eff}\omega}{d^2P_a} \tag{2.80}
$$

where μ_{eff} is the effective viscosity that takes into account the effect of rarefaction (slip boundary conditions):

$$\mu_{eff} = \frac{\mu}{1 + 9.568\left(\frac{\lambda_f}{d}\right)^{1.159}} \tag{2.81}$$

and d is the distance between the fixed electrode and the moving plate at rest.

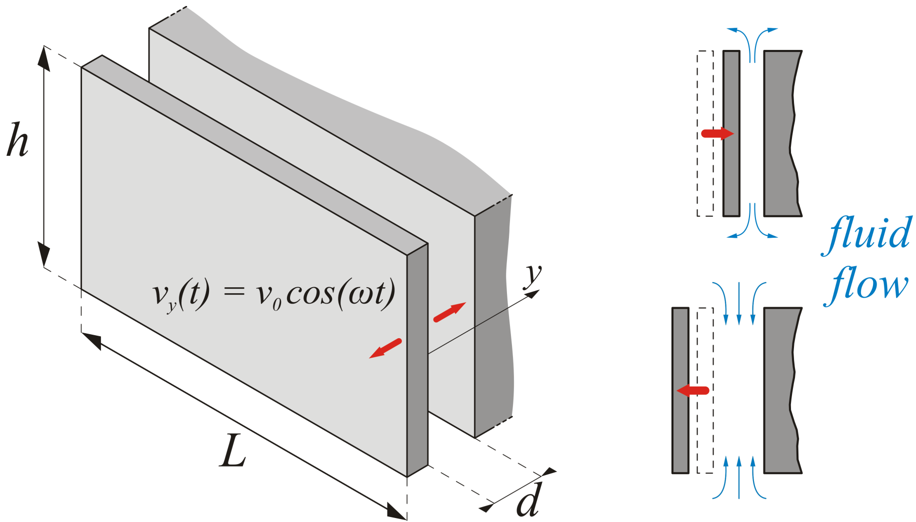

Figure 2.26: Schematic of squeeze film damping.

2.4.3 Effect of holes

In this section, few simple considerations on how the holes pattern drawn onto the resonator may impact the quality factor will be done. Holes certainly reduce the resonator mass and, in principle, may also impact the resonance pulsation and the viscous damping coefficient, which are the other two parameters appearing in the quality factor expression 2.67. Regarding the effect of holes on the viscous damping, squeeze film effect of perforated structures vibrating out-of-plane has been extensively investigated [104, 105]. However, the structures presented in chapters 3 and 4 do not fall into this case, as they move in-plane and the squeeze film effect takes place between the structure and the fixed electrode used for electrostatic actuation. The effect of holes on the air damping of structures vibrating in-plane as not jet investigated. The reasonable assumption considered in this work is to not assume any significant damping inside the holes, therefore the only effect of the holes on the air damping is to reduce the area of the surfaces where slide damping takes place. Moreover, for many typical MEMS designs, such as the ones presented in this thesis, squeeze film damping is order of magnitude bigger than slide film

damping, therefore the holes would not produce any significant change on the damping coefficient (and on the motional resistance too). The effect of holes on the resonance frequency is instead an open point and will be treated separately for each of the presented resonators in the following chapters. However, even with this aspect still to be investigated, it is reasonable to conclude that holes reduce the quality factor, thus generating an important trade-off with the sensitivity S_c that needs to be carefully evaluated when drawing the geometry of the holes matrix. Unfortunately the quality factor estimation with the proposed models is expected to have a very poor accuracy, therefore a numerical optimization of the holes geometry, aimed at maximizing $|QS_c|$ (such as the one presented for the sensitivity in section 2.1), would result in a merely theoretical exercise. This poor accuracy is mostly due to the presented damping models which work as rough estimators for the viscous losses that the resonator experience in the surrounding fluid. For this reason, experimental evaluation is a necessary step when dealing with air damping problems, the absence of significant losses inside the holes is another aspect that deserves an accurate experimental evaluation.

3

Resonant beam sensor

In this chapter clamped-clamped beam resonant sensors with regular square perforations will be presented. The resonant mode of interest will be the first in-plane mode. In order to estimate the resonant sensor main parameters described in chapter 2, a time-efficient technique to compute the resonance frequency that takes into account the effect of perforations is needed. For this reason, in section 3.1 of this chapter, a simple analytical model capable of estimating the resonance frequency of square perforated beams will be developed. In section 3.2 the dimensions of the designed structures, as well as the main parameters of the two technological precesses used to realize them, will be briefly exposed. In section 3.3, the properties of one of the employed processes along with the resonance frequency model developed in section 3.1, will be used in order to estimate the other important parameters of the sensor. Finally, in section 3.4, a few preliminary measurements, carried out with the two-port open loop electrostatic setup of figure 2.19, will be presented.

3.1 Analytical model for the resonance frequencies

As already stated in section 2.1, perforations are often introduced in MEMS structures for technological purposes (release step) and affect the mechanical behavior of these structures in various ways. However, their effect on the mechanical behavior of beams and plates has been extensively investigated only for specific cases and applications. For example, models exist for the effect of holes on the viscous losses around plates for the case of squeeze damping [104, 105]. The influence of perforations on thermoelastic damping and anchor losses in bulk plate resonators has been studied as well [106, 107]. Numerical methods can be and have been used to predict the mechanical behavior of such structures [108, 109, 110]. However, their computational load increases dramatically with the reduction of the hole size. Moreover, the mechanical properties of regularly structured materials can also be modeled by an equivalent anisotropic material [111, 112, 113]. As far as the determination of resonance frequencies is concerned, different semianalytical models have been developed. For example, Yan and Seshia [113] use the Rayleigh-Ritz

method on the standard solution of a full beam, a method which is only valid for small holes, or an equivalent material model based on cellular material theory [111], which, on the contrary, assumes very large holes. Herrera-May and coworkers [114] derive alternative expressions for the kinetic and elastic energies to be used with the Rayleigh-Ritz method under the assumption that the system can be decomposed in a finite number of elements obeying the Euler-Bernoulli beam equation, an hypothesis which fails for a wide range of practical cases (for example, when the holes are small with respect to the typical structure dimensions). The method developed by Civet et al. [115], though more general, leads to very complex calculations for large number of holes. Overall, these approaches are cumbersome and do not lead to simple models for the structural behavior of regularly perforated structures with many holes. In this section, the mechanical properties of beams with regular square perforations are examined, and a simple analytical model to compute the in-plane resonance frequencies of perforated, clamped-clamped beams is proposed. The model is aimed at the fast an accurate estimation of the resonance frequency of these complex structures, which may be of help in the time-efficient design of beam-based MEMS resonant structures, such as resonant sensors. The proposed method is based on a modification of the established beam theory. Specifically, equivalent expressions for the mechanical parameters (stiffness and inertia terms) of perforated beams will be developed, conditions under which such expressions can be used to obtain a valid estimate of the resonance frequencies will be studied too. As it will be clear with the proceeding of this section, in order to describe all the holes geometries, the model has to be based on a modification of the Timoshenko beam equation. While the Timoshenko beam equation is the most complete model for the deflection of beams,

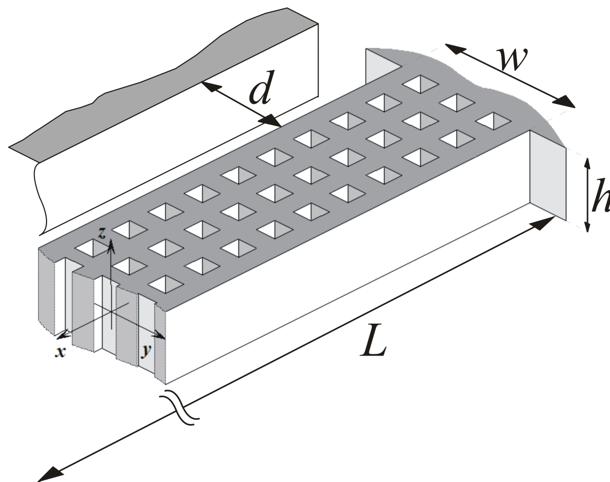

Figure 3.1: View of a perforated beam with the coordinate system used in the text. Part of the beam is cut away for clarity. One of the electrodes used for the two-port electrostatic sensing is also shown.

in most cases simplified models can be used. For example, for slender beams, the Timoshenko equation reduces to the simpler Euler-Bernoulli (EB) equation. Under appropriate hypotheses, that will be discussed extensively later in this section, simplified models can be used also in the case of perforated beams. As a first step, a complete Timoshenko equivalent model for perforated beams is developed. The Timoshenko beam equation for the in-plane motion of a full beam, referred to the axes in 3.1, can be written as [70]:

$$EI\frac{\partial^4 u}{\partial x^4} + \rho A\frac{\partial^2 u}{\partial t^2} - \left(\rho I + \frac{EI \cdot \rho A}{kAG}\right)\frac{\partial^4 u}{\partial x^2 \partial t^2} + \frac{\rho I \cdot \rho A}{kAG}\frac{\partial^4 u}{\partial t^4} =$$
$$p(x,t) + \frac{\rho I}{kAG}\frac{\partial^2 p(x,t)}{\partial t^2} \tag{3.1}$$

where $u = u(x,t)$ is the y-coordinate of the deflected principal axis of the beam and $p(x,t)$ is the force per unit length applied on the beam. Four parameters related to the geometry and material properties of the beam appear in the equation. The first is the bending stiffness EI, the product of the Young's modulus E and the moment of inertia I of the beam section; the second is the mass per unit length ρA, with ρ the material density and A the area of the section; the third is the shear stiffness kAG, with G the shear modulus of the material and k a correction factor (smaller than 1) taking into account the shape of the section; finally the fourth parameter is the rotational inertia per unit length, ρI. When dealing with the resonance frequency problem, the external load $p(x,t)$ is set to 0. By postulating a solution of the form

$$u(x,t) = U(x)cos(\omega t) \tag{3.2}$$

and substituting (3.2) in (3.1), an ordinary differential equation is obtained:

$$EI\frac{d^4 U}{dx^4} + \rho A\omega^2 U + \left(\rho I + \frac{EI \cdot \rho A}{kAG}\right)\omega^2\frac{d^2 U}{dx^2} + \omega^4\frac{\rho A \cdot \rho I}{kAG}U = 0. \tag{3.3}$$

For many practical cases, complete solution of (3.3) is not required. It can be shown [70] that for typical materials and cross-sections the rotational inertia term ρI is 3-6 times smaller than the shear deformation term $EI \cdot \rho A/kAG$, so that the former can be neglected. In the following, we will show that this approximation holds also for perforated beams. Also, for lower order resonance modes and slender beams, shear stiffness is high enough that shear deformations can be neglected. If both these approximations hold, (3.3) degenerates into the EB equation:

$$EI\frac{d^4 U(x)}{dx^4} - \rho A\omega^2 U(x) = 0 \tag{3.4}$$

for which closed-form solutions are available for all typical boundary conditions. When only the contribution of rotational inertia can be neglected (i.e., again, in many cases of practical importance), (3.3) reduces to the so-called shear beam equation [70]:

$$EI\frac{d^4 U}{dx^4} - \rho A\omega^2 U + \frac{EI\rho A}{kAG}\omega^2\frac{d^2 U}{dx^2} = 0. \tag{3.5}$$

In the following paragraphs, equivalent models for the characteristic parameters of a perforated beam (i.e. the bending and shear stiffnesses EI_{eq} and AG_{eq}, and the mass and rotational inertia per unit length ρA_{eq} and ρI_{eq}) will be developed. The behavior of a perforated beam will be analyzed using a modified Timoshenko equation containing the equivalent characteristic parameters. To this purpose, a beam of length L, width w and thickness h, with the pattern of square holes described in section 2.1 (see figure 2.3 and equations (2.3)) will be considered. Because the most part of MEMS designs fall into this category, the analysis will be limited to the case of slender beams, assuming ($w \ll L$).

3.1.1 Perforated beam equivalent parameters

Equivalent bending stiffness model

In the classic beam theory for full beams [116, p. 91] (i.e. beam with constant rectangular cross-section), a linear distribution of the normal stress $\sigma_x = \sigma_{eb}$ along the beam width is assumed (figure 3.2):

$$\sigma_{eb}(y) = \frac{M_z}{I_{eb}} y \tag{3.6}$$

where M_z is the total bending moment at the cross-section and $I_{eb} = w^3h/12$ is the moment of inertia of the cross-section. In presence of holes, EB theory fails because of the variable beam cross-section. While variable cross-section beams are often studied using the standard EB theory for each segment [116, p. 209], this approximation gives sufficient accuracy provided that 1) the variation of the cross-section along the beam length is continuous and not too extreme, or 2) in the case of abrupt changes, the variation of cross-section is small in comparison with the lengths of the segments. In reality, most perforated beams of interest in MEMS applications do not belong to either case. Therefore, special considerations have to be made in order to develop a model for the normal stress distribution in a perforated structure. For comparison, the equivalent bending stiffness derived from the standard stress distribution, called *geometric model* in the following, will be firstly exposed. The standard approximation of the Euler-Bernoulli theory for treating variable cross section beams is to assume in each section the stress distribution that the section would have if it would have been part of a constant section beam, as shown in figure 3.3. Therefore the stress in the filled section will be the same of the full beam case of equation (3.6), while the normal stress in the perforated section σ_h will be:

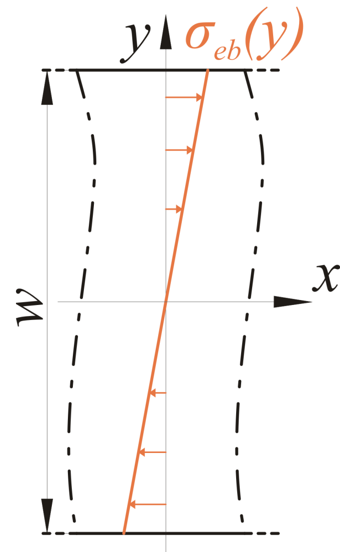

Figure 3.2: Normal stress distribution in a full beam.

$$\sigma_h(y) = \frac{M_z}{I_h} y \tag{3.7}$$

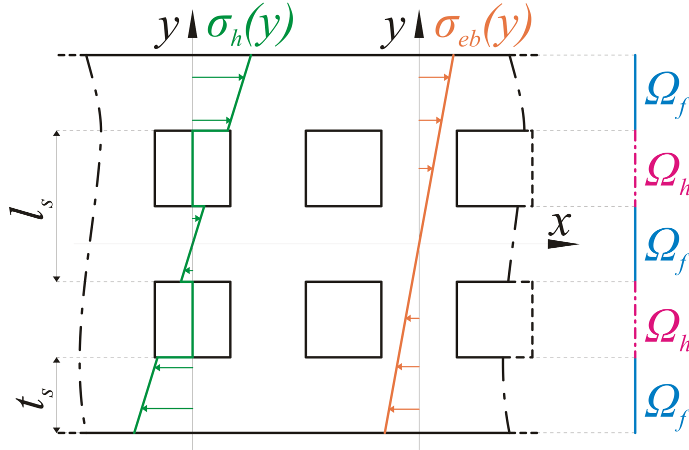

Figure 3.3: Normal stress distribution obtained applying the linear distribution of the Euler-Bernoulli theory in each of perforated beam sections, this approximation is referred as *geometric model* in the text. The domains of integration highlighting the regions along the y axis where the beam is full (Ω_f) and where the beam is perforated (Ω_h) are also shown.

where I_h is the moment of inertia of the perforated cross-section, whose value can be computed from the general formula for the moment of inertia:

$$I_h = \int_{-h/2}^{h/2} \int_{y \in \Omega_f} y^2 \, dy \, dz = I_{eb} \frac{\alpha(1+N)(2N+N^2+\alpha^2)}{(N+\alpha)^3} \tag{3.8}$$

The bending stiffnesses in the filled and perforated sections will be EI_{eb} and EI_h respectively. With the bending stiffness defined in any of the beam cross sections, its deformed shape due to any type of load can be computed. To find a simple closed form expression for the bending stiffness of the perforated beam, the pure bending problem of figure 3.4 is considered. The deformed shape $u_{beam}(x)$ can be found by solving each constant section segment and linking them with continuity conditions. This deformed shape is thus approximated with the one of a full beam subjected to the same boundary conditions:

$$u_{geom}(x) = -\frac{M_z}{2EI_{geom}} x^2 = \beta_{geom} x^2 \tag{3.9}$$

where EI_{geom} is the equivalent bending stiffness of the *geometric model*. An expression for EI_{geom} can be found by using a least square approximation:

$$min \left\{ \int_0^L \left(u_{beam}(x) - \beta_{geom} x^2 \right)^2 \, dx \right\} \rightarrow EI_{geom} \tag{3.10}$$

Where the ad-hoc variable β_{geom}, useful for the following computations has been defined. Once that the integral is solved, expression (3.10) si a second order polynomial in the β_{geom} variable. Therefore a closed form expression for EI_{geom} is found by solving:

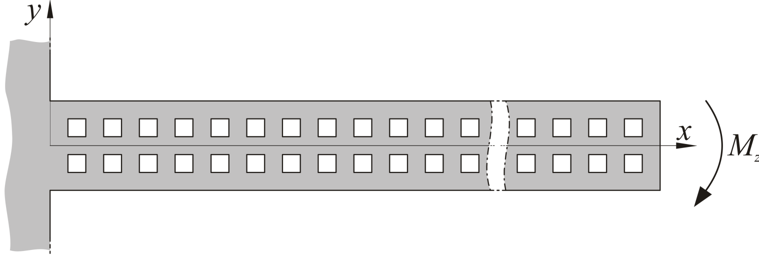

Figure 3.4: Pure bending problem used to find a compact expression for the equivalent bending stiffness of the perforated beam.

$$\frac{d}{d\beta_{geom}}\left[\int_0^L \left(u_{beam}(x) - \beta_{geom}x^2\right)^2\, dx\right] = 0 \tag{3.11}$$

The solution β_{opt} of equation (3.11), though straightforward, can be a very complex function, if the beam is slender a good simplification is to take the limit for $N \to \infty$. Exploiting the relationship between β_{geom} and EI_{geom} of equation (3.9), the expression for the equivalent bending stiffness of the *geometric model* is found:

$$EI_{geom} = \lim_{N\to\infty} -\frac{M_z}{2}\cdot\frac{1}{\beta_{opt}} = \left(\frac{1-\alpha}{EI_h} + \frac{\alpha}{EI_{eb}}\right)^{-1} \tag{3.12}$$

The final expression is found by substituting equation 3.8 in the solution:

$$EI_{geom} = EI_{eb}\frac{(N+1)\alpha(N^2+2N+\alpha^2)}{(\alpha^2-\alpha+1)N^3+3\alpha N^2+\alpha^2(\alpha^2-3\alpha+5)N+\alpha^3} \tag{3.13}$$

The limit of this model is the assumption of a linear distribution of the normal stress in the filled sections. The new model proposed in this section, called *equivalent model* in the following, is based on a piecewise-linear distribution of the stress in these sections. Some argument are needed in order to explain why this distribution is more realistic than the one of the *geometric model*, and why the linear distribution is instead a valid assumption in the sections with holes. Each longitudinal fiber in the beam segments with holes (referred with subscript h in the following), extending for a length $(1-\alpha)l_s$, belong to material fibers which extend throughout the length of the beam, so that, in analogy with constant-section beams, assuming that they withstand the normal stress implied by the EB stress distribution $\sigma_h(y)$ of equation 3.7 is reasonable. Each filled beam segment (referred with subscript f in the following) extends for a length αl_s. A linear stress distribution is obviously unreasonable in this case, as the material between two adjacent holes has a stress-free boundary, while the remaining parts of the segment (belonging to the same fibers as the perforated segments) withstand the traction at their boundaries imposed by the perforated segments on their sides. As a result, the normal stress will be reduced in the parts between holes, which will be under-stressed with respect the full beam case, and will concentrate in the remaining parts, which will be over-stressed, so that the total bending moment remains constant. A possible model for this stress condition is the

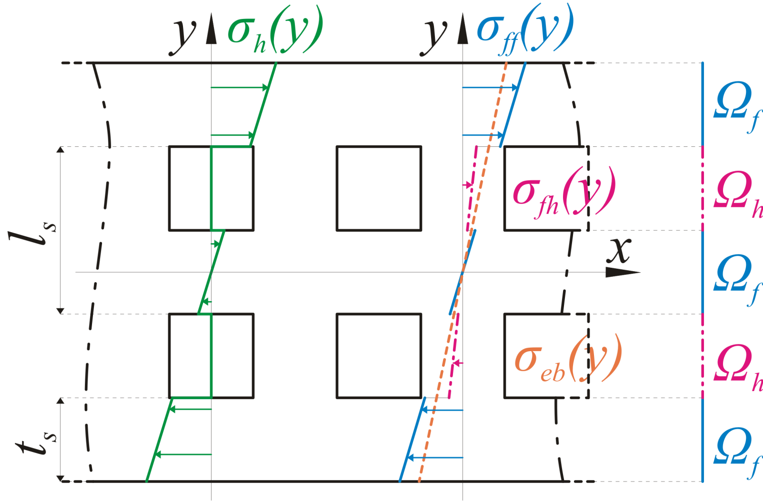

Figure 3.5: Equivalent model for the normal stress distribution in the perforated (left, green line) and filled (right, blue-pink line) segments of a perforated beam. The geometric stress distribution in the filled section (right, dashed line) is superimposed for comparison.

piecewise linear distribution (with two different slopes) of figure 3.5 (the parts between holes and the remaining ones are referred with the subscripts fh and ff, respectively). This distribution can be written with to different linear functions:

$$\sigma_{fh}(y) = \frac{M_z}{I_{fh}} y \qquad \sigma_{ff}(y) = \frac{M_z}{I_{ff}} y \tag{3.14}$$

where I_{ff} and I_{fh} (with the dimensions of a moment of inertia) are parameters whose values depend on the geometry of the perforations and are still to be determined. Once these parameters are obtained, the bending of the structure can be computed by considering the bending of those material fibers of the beam which extend through its whole length (3.1), which is described by the bending stiffness EI_h in the perforated sections, and by the bending stiffness EI_{ff} in the filled sections. The bending stiffness of the *equivalent model* is thus obtained by substituting EI_{ff} to EI_{eb} in the expression (3.12):

$$EI_{eq} = \left(\frac{1-\alpha}{EI_h} + \frac{\alpha}{EI_{ff}} \right)^{-1} \tag{3.15}$$

To compute an explicit expression for EI_{eq}, an expression for I_{ff} has to be determined. A first relationship between I_{ff} and I_{fh} is obtained by writing the bending moment in the filled segment and equating it to the total bending moment M_z:

$$M_z = h \left(\int_{\Omega_f} \sigma_{ff}(y) y \, dy + \int_{\Omega_h} \sigma_{fh}(y) y \, dy \right) \tag{3.16}$$

where Ω_h is the complementary domain of Ω_f (see figure 3.5). Substituting (3.14) into (3.16):

$$I_{ff} = \frac{I_{fh} I_h}{I_{fh} + I_h - I_{eb}} \tag{3.17}$$

To obtain I_{ff}, a second relationship is required. As the parts between holes are progressively less stressed for larger holes (i.e. for α approaching zero), a very simple hypothesis is to assume that the normal stress in those parts is proportional to α:

$$\sigma_{fh} = \alpha \sigma_{eb} \tag{3.18}$$

which immediately leads to:

$$I_{fh} = \frac{I_{eb}}{\alpha} \tag{3.19}$$

Substituting (3.19) and (3.17) into (3.12) finally gives:

$$EI_{eq} = EI_{eb} \frac{(N+1)\alpha(N^2 + 2N + \alpha^2)}{(1 - \alpha^2 + \alpha^3)N^3 + 3\alpha N^2 + (3 + 2\alpha - 3\alpha^2 + \alpha^3)\alpha^2 N + \alpha^3} \tag{3.20}$$

Equivalent shear stiffness model

If shear deformations are not negligible, the cross-sections of the beam and its principal axis are no longer orthogonal. The deviation of the angle between them from $\pi/2$, i.e. the shear angle β, is inversely proportional to the shear stiffness kGA [116, p. 170]:

$$\beta = \frac{T}{kGA} \tag{3.21}$$

where T is the shear force. As in the case of bending, the presence of holes modifies the shear deformation of the beam. Specifically, shear deformation of the beam can be significant even in very slender beams, which is generally not true for full beams. The starting

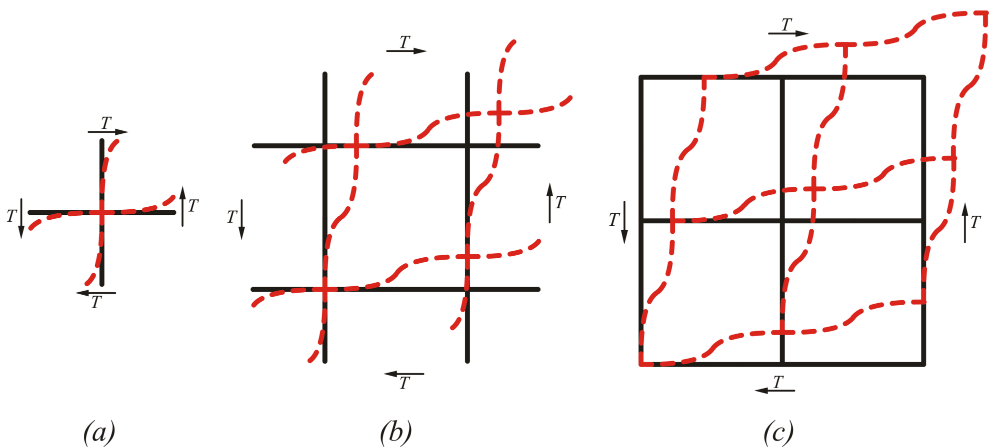

Figure 3.6: Shear deformation under the hypotesis of slender beams. *(a)* single cell, *(b)* 4 cells centered in the joint and *(c)* 4 cells centered in the hole.

point is the equivalent shear stiffness AG_{eq} for infinite square networks of joined slender beams. By using the unit cell (centered in the joint) of 3.6 (a), Wand and McDowell [111] developed the following expression:

$$AG_{eq} = A\frac{E}{2}\alpha^3 \tag{3.22}$$

In the case of a finite number of cells N, this expression has to be adjusted. Since our unit cell is centered in the hole (figure 3.6 (c)), N cells correspond to a network with $N+1$ beams, and thus to an increased shear stiffness:

$$AG_{eq} = A\frac{N+1}{N}\frac{E}{2}\alpha^3 \tag{3.23}$$

For a large number of holes this model converges to the one of (3.22), as expected. In our case, the hypothesis of slender beams would impose a very restrictive upper limit on the value of α (i.e. $\alpha < 0.1$ if we fix the slenderness limit at 10). However, with increasing α the beam progressively approximates a full slender beam, where shear deformations are generally negligible, i.e. the beam is under pure bending, so that the actual value of AG_{eq} is not important. For this reason, equation (3.23) will be used for the whole range of α.

Equivalent mass per unit length model

The computation of the equivalent mass per unit length is straightforward, and is simply the average mass per unit length of the perforated beam. By integrating over a beam segment we obtain:

$$\rho A_{eq} = \rho A\frac{(1 - N(\alpha - 2))\alpha}{N + \alpha} \tag{3.24}$$

Equivalent moment of inertia per unit length model

To derive the equivalent moment of inertia per unit length ρI_{eq} we integrate and average over a strip of N square cells of length l_s:

$$\begin{aligned}\rho I_{eq} &= \rho\frac{1}{l_s}h\int_{x,y\in\Sigma}\rho\left(x^2+y^2\right)dxdy = \\ &= \rho I_{eb}\frac{\alpha\left((2-\alpha)N^3 + 3N^2 - 2(\alpha-3)(\alpha^2-\alpha+1)N + \alpha^2 + 1\right)}{(N+\alpha)^3}\end{aligned} \tag{3.25}$$

where the plane domain Σ defines the zones without holes (see 3.7). Because of the finite width of the strip, this expression depends on the choice of the center of inertia, but this dependence becomes negligible for small cells or, equivalently, for large N.

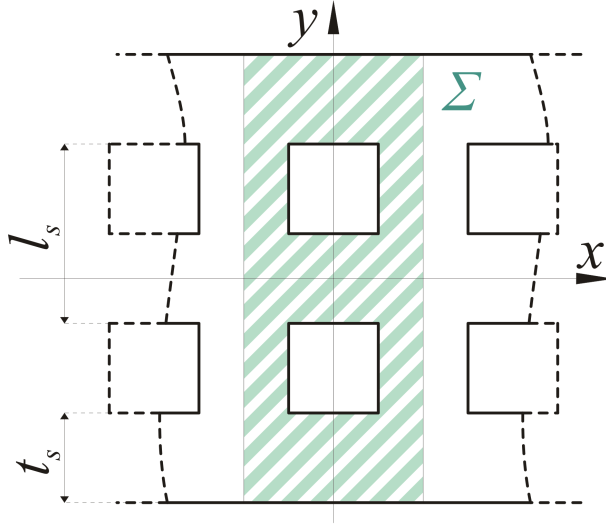

Figure 3.7: Integration domain for the integral in (3.25).

3.1.2 Expression for the resonance frequencies

By substituting the four equivalent parameters shown in equations (3.20), (3.23), (3.24) and (3.25) into the factorized Timoshenko beam equation (3.3), the model for the harmonic motion of perforated beams is obtained. Before solving the full Timoshenko equation is useful to examine the conditions that allow the use of the simplified shear (3.5) or even EB (3.4) equations. In order to neglect rotatory inertia effects the following inequality has to hold true [70]:

$$\frac{EI_{eq} \cdot \rho A_{eq}}{AG_{eq} \cdot \rho I_{eq}} \gg 1 \tag{3.26}$$

by replacing our equivalent models for the characteristic parameters, the ratio on the left side is found to be a monotonically decreasing function with α. This makes the full beam (for which the rotatory inertia is commonly neglected [70]) the worst case scenario. For this reason is reasonable to assume that the rotatory inertia term ρI_{eq} is always negligible, i.e. that the shear equation is always a good description of the perforated beam problem. To investigate the conditions for which the simpler EB equation can be used in presence of holes, a further consideration needs to be done. As it will be shown in the next section, the shear model resonance frequency expression is a function of the geometry dependent variable γ:

$$\gamma = \frac{EI_{eq}}{AG_{eq}L^2} \tag{3.27}$$

The larger is γ, the greater is the influence of shear deformations. The condition $\gamma = 0$ corresponds to the absence of shear deformations (i.e. to the EB equation). For perforated beams, γ can be expressed as a function of N and α:

$$\gamma = \frac{1}{6}\left(\frac{w}{L}\right)^2 \gamma_F(N,\alpha) \ll 1 \tag{3.28}$$

where $\gamma_F(N,\alpha)$ is an appropriate rational function of its arguments:

$$\gamma_F = \frac{N\left(N^2+2N+\alpha^2\right)}{\alpha^2\left(\left(\alpha^3-\alpha^2+1\right)N^3+3\alpha N^2+\alpha^2\left(\alpha^3-3\alpha^2+2\alpha+3\right)N+\alpha^3\right)} \tag{3.29}$$

As γ_F diverges as α^{-2} in a neighborhood of $\alpha = 0$, there is always a lower limit for α (which depends on the beam slenderness w/L) below which the inequality (3.28) fails. As a consequence, shear effects cannot be neglected if the beam is studied over the whole range $\alpha \in (0-1]$, and the shear equation (3.5) has to be used. If only the behavior above this limit is of interest, however, the EB equation (3.4) can be used. In the following, by solving the shear equation (3.5) an expression for the resonance frequencies of a clamped-clamped perforated beam will be derived. By considering an infinite shear stiffness (i.e. no shear deformations) in the shear model expression, the Euler-Bernoulli one will be also extracted. Once that both expressions are derived, a qualitative method to evaluate the error committed by using the rough EB equation with respect to the more accurate shear equation will be given. The eigenvalue equation obtained imposing the clamped-clamped boundary conditions to the shear equation 3.5 is [70]:

$$2a^3b^3 - 2a^3b^3\cos a\cosh b - \left(b^6-a^6\right)\sin a\sinh b = 0 \tag{3.30}$$

The wave numbers a and b are functions of the equivalent quantities:

$$a = \sqrt{-C_1+\sqrt{C_1^2+C_2^4}} \qquad b = \sqrt{C_1+\sqrt{C_1^2+C_2^4}} \tag{3.31}$$

$$C_1 = \frac{2\pi^2\rho A_{eq}L^2f^2}{AG_{eq}} \qquad C_2 = \sqrt[4]{\frac{4\pi^2\rho A_{eq}L^4f^2}{EI_{eq}}} \tag{3.32}$$

where f is the frequency. The values of f that solve (3.30) are the resonance frequencies. Since the only unknown f appears in both the wave numbers, the problem cannot be easily solved using this notation. This problem can be overcome by showing that:

$$\frac{C_1}{C_2^4} = \frac{\gamma}{2} \tag{3.33}$$

where γ hase been defined in (3.27). Substituting equations (3.31), (3.32) and (3.33) in equation (3.30) the result is a trascendent equation in the only unknown C_2:

$$\begin{aligned}
&-\gamma\sin\left(\sqrt{\frac{\gamma C_2^4}{2}+\sqrt{\frac{1}{4}\gamma^2C_2^8+C_2^4}}\right)\sinh\left(\sqrt{\sqrt{\frac{1}{4}\gamma^2C_2^8+C_2^4}-\frac{\gamma C_2^4}{2}}\right)\cdot\\
&\cdot\left(\gamma^2C_2^4+3\right)C_2^2+2\cos\left(\sqrt{\frac{\gamma C_2^4}{2}+\sqrt{\frac{1}{4}\gamma^2C_2^8+C_2^4}}\right)\cdot\\
&\cdot\cosh\left(\sqrt{\sqrt{\frac{1}{4}\gamma^2C_2^8+C_2^4}-\frac{\gamma C_2^4}{2}}\right)-2=0
\end{aligned} \tag{3.34}$$

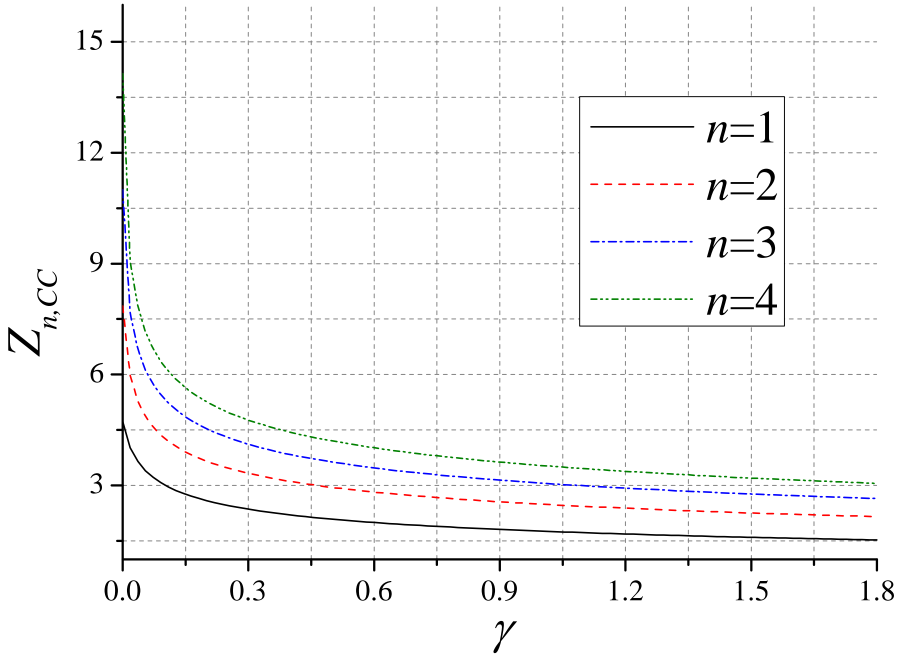

Figure 3.8: First four roots of the clamped-clamped eigenvalue equation 3.34 as a function of γ.

Equation (3.34) can be numerically solved in order to build a set of functions $Z_{n,CC}(\gamma)$, representing the nth root of the equation as a function of γ (see 3.8). Using these functions and the definition of C_2 taken from (3.32), the expression for the nth resonance frequency f_n of the perforated clamped-clamped shear beam is found:

$$f_n = \frac{1}{2\pi}\sqrt{\frac{EI_{eq}Z_{n,CC}(\gamma)^4}{\rho A_{eq}L^4}} \tag{3.35}$$

The Euler-Bernoulli model can be obtained considering an infinite shear stiffness, i.e. no shear deformations ($\gamma = 0$):

$$f_{n,EB} = \frac{1}{2\pi}\sqrt{\frac{EI_{eq}Z_{n,CC}(0)^4}{\rho A_{eq}L^4}} \tag{3.36}$$

If we limit our discussion to slender beams ($L/w \geq 10$) with α varying in the interval $[0.05 - 1]$, γ varies in the interval $[0 - 1.8]$. Table 3.1 gives a rational interpolation for the first 4 $Z_{n,CC}(\gamma)$ functions, with an error below 0.35% over the range of interest of γ. These functions are aimed at giving a fast and simple solution tool without passing through the numerical solution of (3.34). In the same table the EB solution ($\gamma = 0$) is also shown.

n	$Z_{n,CC}(\gamma)$	$Z_{n,CC}(0)$
1	$\frac{\gamma^3+3.30\gamma^2+\left(7.84\cdot10^{-1}\right)\gamma+2.57\cdot10^{-2}}{1.06\gamma^3+1.60\gamma^2+(2.33\cdot10^{-1})\gamma+5.44\cdot10^{-3}}$	4.73
2	$\frac{\gamma^3+2.90\gamma^2+\left(5.07\cdot10^{-1}\right)\gamma+9.61\cdot10^{-3}}{(7.30\cdot10^{-1})\gamma^3+(9.43\cdot10^{-1})\gamma^2+(9.76\cdot10^{-2})\gamma+1.22\cdot10^{-3}}$	7.85
3	$\frac{\gamma^3+2.76\gamma^2+\left(4.15\cdot10^{-1}\right)\gamma+5.19\cdot10^{-3}}{(5.91\cdot10^{-1})\gamma^3+(7.12\cdot10^{-1})\gamma^2+(5.91\cdot10^{-2})\gamma+4.72\cdot10^{-4}}$	11.00
4	$\frac{\gamma^3+2.63\gamma^2+\left(3.49\cdot10^{-1}\right)\gamma+3.35\cdot10^{-3}}{(5.08\cdot10^{-1})\gamma^3+(5.76\cdot10^{-1})\gamma^2+(4.04\cdot10^{-2})\gamma+2.37\cdot10^{-4}}$	14.14

Table 3.1: Rational functions interpolating the first four roots of the clamped-clamped eigenvalue equation (3.34) as a function of γ. Their values at $\gamma = 0$ is also shown. The error with respect to the exact root is below 0.35% over the range of γ shown in figure 3.8.

3.1.3 FEM validation

In order to verify the validity of the proposed model, extensive Finite Element Method (FEM) simulations with ANSYS were carried out. To allow a consistent comparison, clamped-clamped perforated beams were modelled as 2D structures (meshed with the ANSYS element PLANE182) under a plane stress hypothesis, which corresponds to the case of beams of negligible thickness. A modal analysis was performed and the resonance frequencies of the first four resonance modes were extracted. The beam material was [110] single crystal silicon, described with the following parameters: Young's modulus $E = 169\,\mathrm{GPa}$, Poisson's ratio $\nu = 0.064$, shear modulus $G = 50.9\,\mathrm{GPa}$ [117]. The in-plane dimensions of the beams were $L = 1401.1\,\mu\mathrm{m}$ and $w = 46.9\,\mu\mathrm{m}$. Simulations have been performed for four different values of N (1, 2, 4 and 8) and for a range of α between 0.05 and 1 (for $N = 1, 2, 4$) and between 0.15 and 1 for $N = 8$ (where small values of α led to excessive computational load). The FEM simulated values of the first resonance frequency, which is the most significant from an application point of view, are shown in figures 3.9 through 3.12 as a function of α and for the four different values of N, along with the corresponding values obtained with our model, both in the case of shear and EB equations ((3.35) and (3.36) respectively), and also, for comparison, using the *geometric model* for the bending stiffness. The relative errors of the four models with respect to the FEM simulations are shown in figure 3.13 and 3.14 for two values of N (2 and 8, respectively). For legibility, the graphs for the EB-based models (which are expected to fail for small α) have been clipped to exclude very large values of the errors. The errors for the proposed *equivalent model* are consistently smaller than those of the *geometric model*. Also, the error quickly decreases for increasing N's: for the shear equation, for example, the error is below 2% over the whole range of α for $N = 8$. Since the only difference between equivalent and geometric models (for each equation) is the expression used for the bending stiffness, this comparison clearly shows the superiority of the more realistic piecewise-linear stress distribution (shown in figure 3.5) with respect to the geometric one. A similar analysis can be performed for higher resonance modes as well. The analysis presented here is limited up to the fourth mode. For comparison, the plots

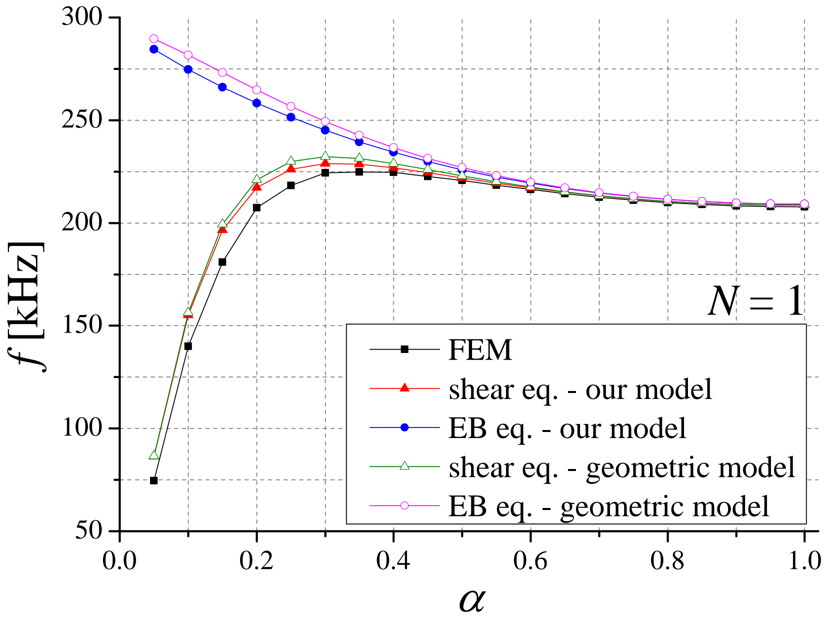

Figure 3.9: First resonance frequency as a function of α and $N = 1$. Beam dimensions are $L = 1401.1\ \mu\text{m}$ and $w = 46.9\ \mu\text{m}$. FEM simulations and models are presented.

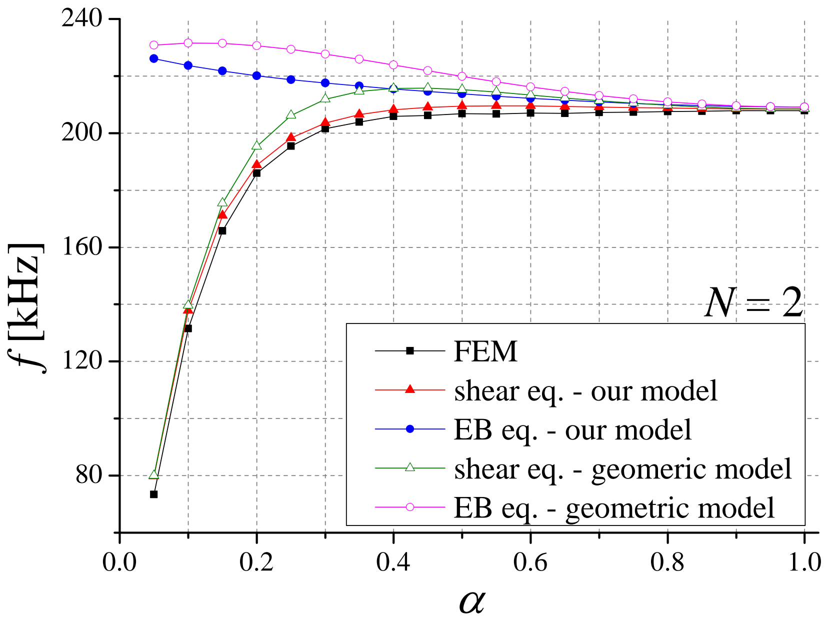

Figure 3.10: First resonance frequency as a function of α and $N = 2$. Beam dimensions are $L = 1401.1\ \mu\text{m}$ and $w = 46.9\ \mu\text{m}$. FEM simulations and models are presented.

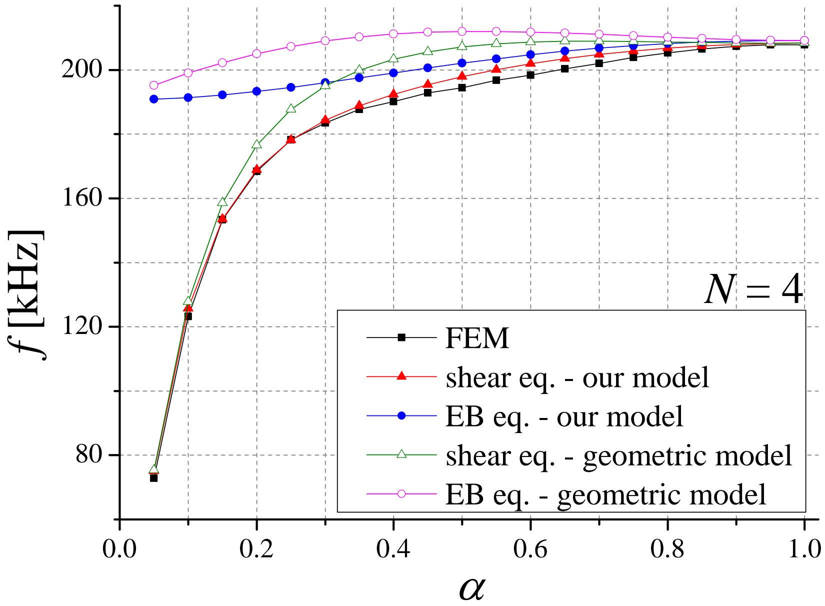

Figure 3.11: First resonance frequency as a function of α and $N = 4$. Beam dimensions are $L = 1401.1\ \mu\text{m}$ and $w = 46.9\ \mu\text{m}$. FEM simulations and models are presented.

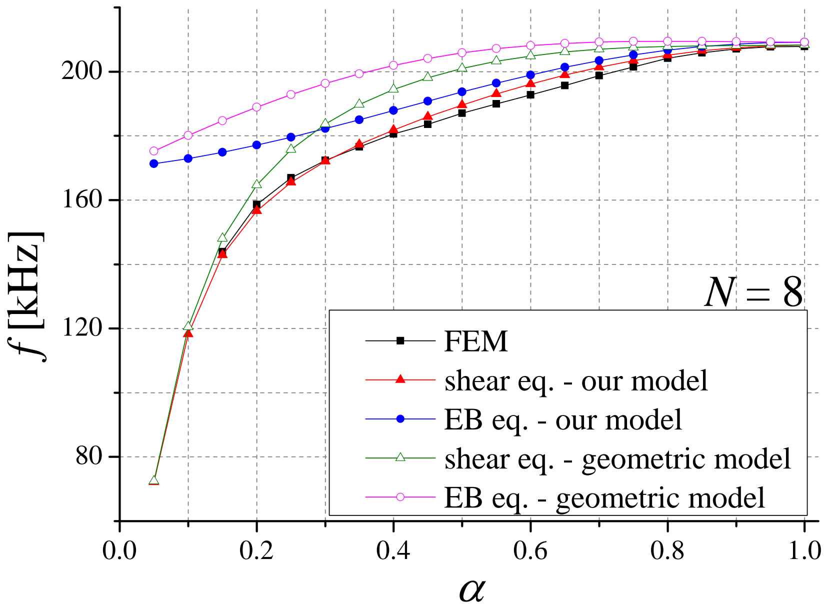

Figure 3.12: First resonance frequency as a function of α and $N = 8$. Beam dimensions are $L = 1401.1\ \mu\text{m}$ and $w = 46.9\ \mu\text{m}$. FEM simulations and models are presented.

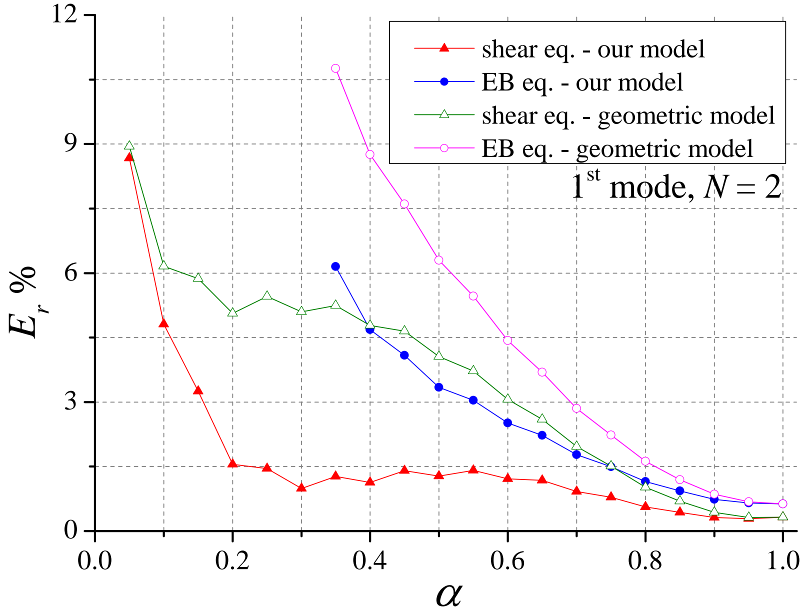

Figure 3.13: Relative error of the models with respect to FEM simulations. First resonance mode, $N = 2$.

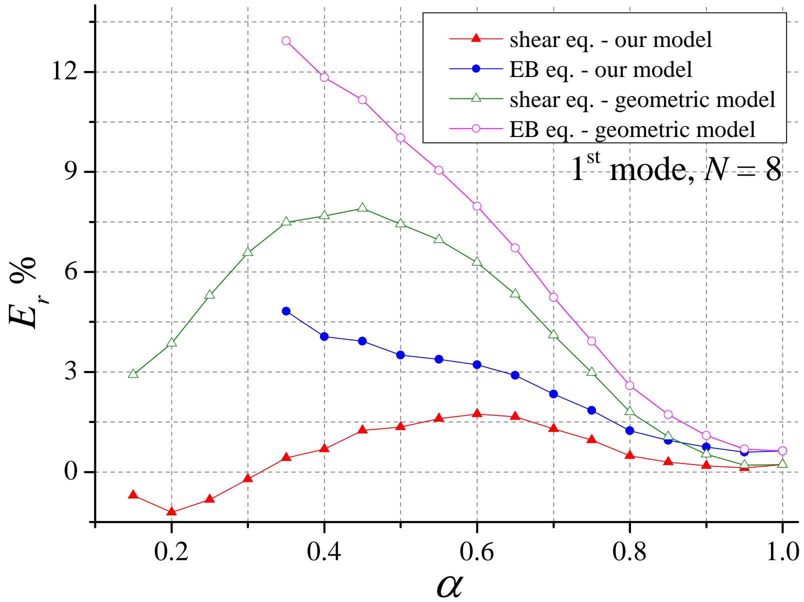

Figure 3.14: Relative error of the models with respect to FEM simulations. First resonance mode, $N = 8$.

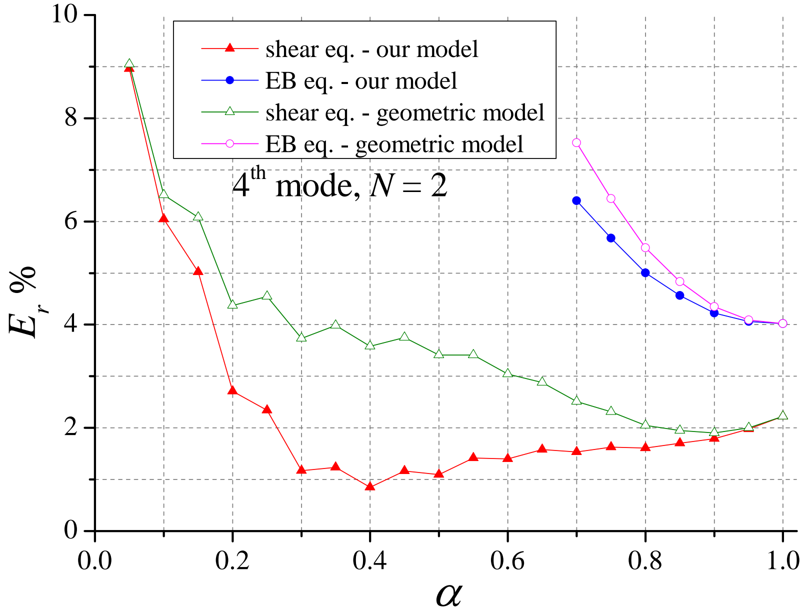

Figure 3.15: Relative error of the models with respect to FEM simulations. Fourth resonance mode, $N = 2$.

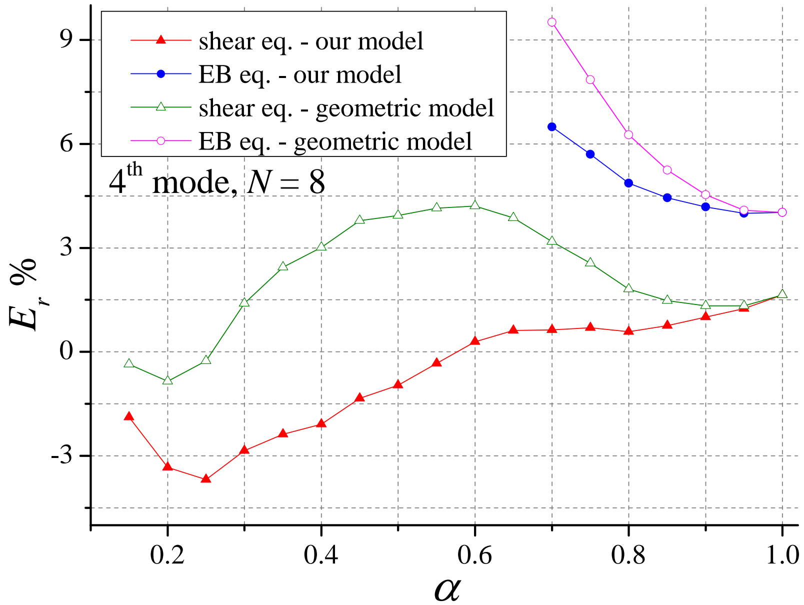

Figure 3.16: Relative error of the models with respect to FEM simulations. Fourth resonance mode, $N = 8$.

for the relative errors for the fourth resonant mode are shown in figures 3.15 and 3.16. As a practical method to decide when to use the EB equation or the shear equation (which is computationally more complex) to determine a resonance frequency with the proposed models, the relative error between the two cases was determined through the respective equations for the resonance frequencies (3.36) and (3.35). This error, which depends only on the value of γ, is plotted for the first four resonance modes in figure 3.17. For each problem at hand, the value of γ (computed from (3.28) and (3.29)) can be used, in conjunction with the error plot, to determine the expected error for the EB model with respect to the shear model. As a conclusion to this section, an analytical model for the estimation of the resonance frequency of square-perforated beams with an accuracy of a few percentage points was presented. From the point of view of the resonance sensor, this model can be used to estimate viscous losses, quality factor and motional resistance with the models presented in chapter 2. This topic will be expanded in section 3.3. However, by looking at the resonance frequency behavior with respect to α, shown in the plot of this section, some consideration can already be done. If the effect of holes over f_1 is very slight as long as the Euler-Bernoulli model assures a sufficient accuracy (i.e. about $\alpha \geq 0.3$), the same cannot be concluded when shear effects starts to be relevant. The increased compliance due to shear deformations results in the remarkable drop of

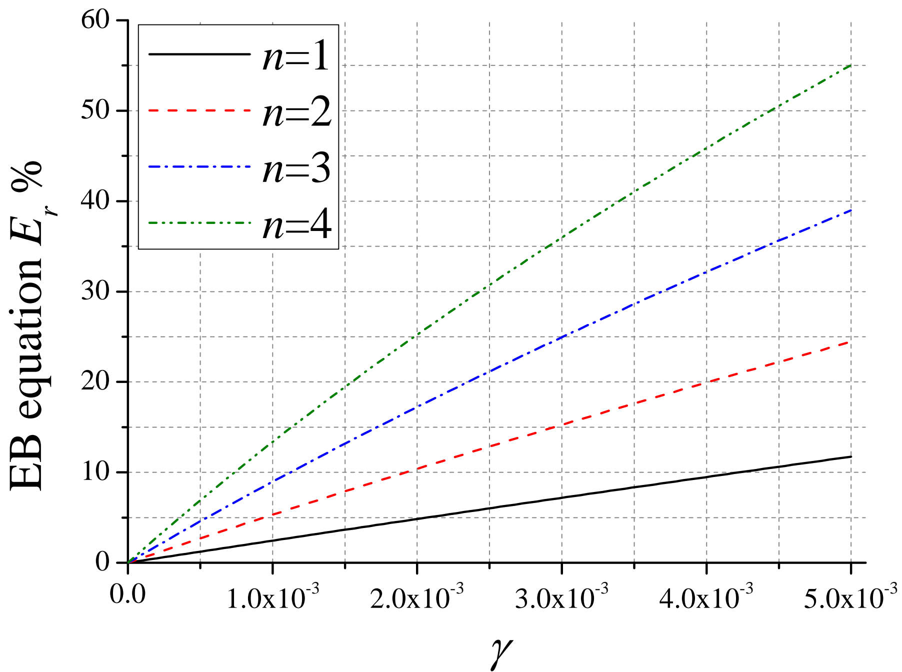

Figure 3.17: Relative error of the EB model (equation (3.36)) with respect to the shear model (equation (3.35)) as a function of γ. The first four resonant frequencies are shown.

the resonance frequency, which falls of about $65\,\%$ when $\alpha \approx 0.05$ with respect to the full beam case. Since the resonance frequency is proportional to the quality factor, its drop due to shear effects has to be considered an unwanted effect as it deteriorates the resonance sensor performances.

3.2 Technological processes

In this section the main characteristics of the two technological processes used to fabricate the beam-based resonant sensors described in this chapter will be briefly summarized. Designed structures dimensions will be summarized too. Based on the geometry described in the previous section, clamped-clamped resonant beam sensors have been fabricated using two different technological processes available through the multi-project wafer of the EUROPRACTICE consortium. The devices have been designed in order to cover most of the available (N-α) design space, considering the technological processes design rules and a minimum acceptable number of holes along w of $N_{min} = 4$ (see figure 2.7). The covering of the whole design space is aimed at experimentally verifying the trends that quantities such as S_c, Q, r_m, and f_0 exhibit while the geometry of the holes pattern moves in the (N-α) design space. These trends have been the subject of the discussion expounded in chapter 2 and in section 3.1 of this chapter, where an analytical model capable of estimating the resonance frequency of square perforated has been developed. In the following section 3.3, the resonance frequency model, jointly with the models presented in section 2.2 for the electromechanical coupling and in section 2.4 for the viscous losses, will be used to estimate damping coefficient, quality factor and motional resistance as a function of N and α. In order to work out these quantities, material and process parameters are needed. Some of these informations cannot be given here due to copyright restrictions, the unrestricted informations for both the technological processes used, together with the designed structures dimensions, will be listed in the following. However, even if not explicitly specified, the full set of process parameters will be used in the computations every time the text refers to these technological processes.

3.2.1 TRONICS

TRONICS process is an SOI process with $60\,\mu\mathrm{m}$ thick (h) Single Cristal Silicon (SCS) structural layer. The material properties of SCS can be found in [117] and are summarized in table 3.2 along with the structural layer thickness h. The layout dimensions of the beams realized with the TRONICS process are instead listed in table 3.3.

material	E [GPa]	ν	G [GPa]	ρ [kg/m^3]	h [µm]
[110] SCS	169	0.064	50.9	2330	60

Table 3.2: TRONICS process main parameters.

3.2.2 SiGe

Poly Silicon-Germanium is a MEMS technology developed at IMEC. The key feature of SiGe MEMS is their processing over CMOS substrates using a low temperature process compatible with the underlying electronics. This technology is thus amenable for

name	L [µm]	w [µm]	N	α
B1	1400	35	0	1
B2	1400	40	4	0.44
B3	1400	48	4	0.36
B4	1400	39	5	0.57

Table 3.3: Resonant beams fabricated with the TRONICS process.

monolithic integration of MEMS resonators with their sustaining electronics. Material and process properties, such as elastic moduli, density, structural layer thickness h an actuation gap d can be found in [118, 119]. Further details about the SiGe technological process can be found in [62]. The process main parameters are summarized in table 3.4, the layout dimensions of the beams realized with the SiGe process can instead be found in table 3.5.

material	E [GPa]	ν	G [GPa]	ρ [kg/m^3]	h [µm]	d [µm]
poly SiGe	120	0.22	49.2	4400	4	0.55

Table 3.4: SiGe process main parameters.

name	L [µm]	w [µm]	N	α
B1	500	36	4	0.25
B2	500	36	4	0.5
B3	500	36	4	0.75
B4	500	28	4	0.3
B5	500	28	4	0.5
B6	500	28	4	0.7
B7	500	36	6	0.35
B8	500	36	6	0.65
B9	500	28	6	0.42
B10	500	28	6	0.58
B11	500	36	0	1
B12	500	28	0	1

Table 3.5: Resonant beams fabricated with the poly silicon germanium (SiGe) process.

3.3 Estimated resonance sensor performances

In this section, the effect of holes over the sensor parameters other than the resonance frequency will be investigated. As an example, a beam with the same outer dimensions used in FEM validation section 3.1.3, $L = 1401.1\,\mu\mathrm{m}$ and $w = 46.9\,\mu\mathrm{m}$ will be considered. The chosen process is TRONICS, whose structural layer is [110] crystalline silicon (see table 3.2). In order to highlight the effect of holes, α will be swept from 0.05 to 1, without considering the layout rules that limit the design space. Damping losses, motional resistance and quality factor will be estimated by means of the modal parameters (2.40) derived in section 2.2.2. The shear equivalent model (3.35) will be used to compute the resonance pulsation. For the particular clamped-clamped beam, modal parameters were found to be equal to the total quantities over the structure (see equations 2.40). The viscous losses due to slide and squeeze film damping are the first quantities that need to be estimated. Slide film damping takes place on the upper and lower surfaces parallel to the substrate of area A_{slide}:

$$A_{slide} = \frac{L^2\alpha\left(-(\alpha-2)N^2 + 2N + \alpha\right)}{Ar(N+\alpha)^2} \tag{3.37}$$

where Ar is the aspect ratio defined in equation (2.3). The resonator slide film damping coefficient c_{slide} is:

$$c_{slide} = \underbrace{A_{slide}c_{u-1s}}_{c_{under}} + \underbrace{A_{slide}c_{o-1s}}_{c_{over}} \tag{3.38}$$

where c_{u-1s} and c_{o-1s} are the slide per unit surface under and over the structure of equations (2.74) and (2.78). The squeeze film damping takes place in the volume between the resonator and the fixed electrodes of the two-port electrostatic configuration. Even if the model of equation (2.79) assumes a surface translating rigidly, it can be used as a valid approximation. This is the same approximation made by Bao in [100, p.138], where the squeeze film damping is assumed uniformly distributed along the gap, thus weighted by the modal shape and finally integrated to give the modal parameter. The total viscous damping is thus obtained by summing the slide damping of equation (3.38) with 2 times the squeeze damping of equation (2.79), in order to take into account both the electrostatic gaps:

$$c_{tot} = c_{under} + c_{over} + 2c_{sqz} \tag{3.39}$$

The damping coefficients computed at the resonance frequency as a function of α are shown in figure 3.18 for $N = 6$. The other cases (N =6, 8) are omitted since there is no substantial difference in the damping behavior, which can be totally ascribed to the squeeze film effect. The predominance of squeeze effects is typical of slender beams where there a small slide area an long actuation gaps. By decreasing the surface A_{slide} where the slide damping takes place, the presence of holes increase even more this dominance. As the damping is totally ascribable to squeeze film effects, it does not depend on holes, therefore the motional resistance $r_m = c_{tot}/\eta^2$, where η is the electromechanical

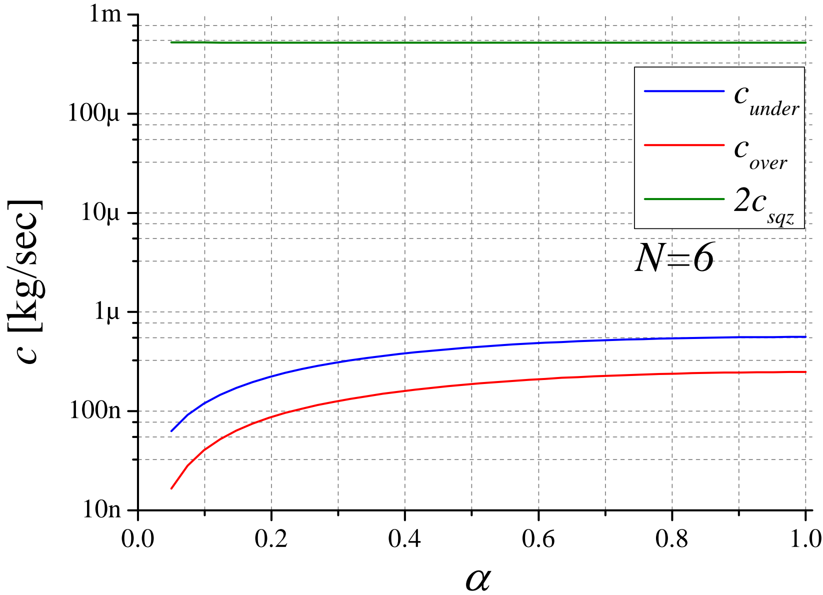

Figure 3.18: Slide and film damping coefficients computed at the beam resonance frequency of the considered beam as a function of α for $N = 6$.

coupling coefficient of equation (2.45), is also independent from the holes. Considering a polarization voltage $V_{DC} = 40\,\mathrm{V}$, an estimation of r_m is found:

$$r_m \approx 144\,\mathrm{M}\Omega \tag{3.40}$$

This high value of the motional resistance is mostly due to the large actuation gaps. The substantial independence of the motional resistance from the hole pattern has been already forecasted in the qualitative discussion expounded in section 2.4.3. By computing the resonator total mass m as:

$$m = hA_{slide}\rho \tag{3.41}$$

the quality factor is known by using equation (2.67). The quality factor plot of figure 3.19 highlights an important decrease of Q when holes dimension is getting bigger ($\alpha \to 0$). This effect results in an important trade-off acting over the perforation approach, which has been initially introduced as a way to increase the concentration sensitivity (see figure 2.4 and section 2.1 for more details). The holes detrimental impact over Q is the result of 2 combined effects: the unavoidable mass decrease (and thus stored energy decrease) with the increase of holes dimension, and the resonance frequency drop (and thus the increase in 1 cycle dissipated energy) well described by the proposed model (equation (3.35)), with the latter effect being very important when $\alpha \lesssim 0.3$ due to shear effects. Also this unwanted effect of the holes over the quality factor has already been forecasted in the qualitative discussion of section 2.4.3. The very poor value estimated

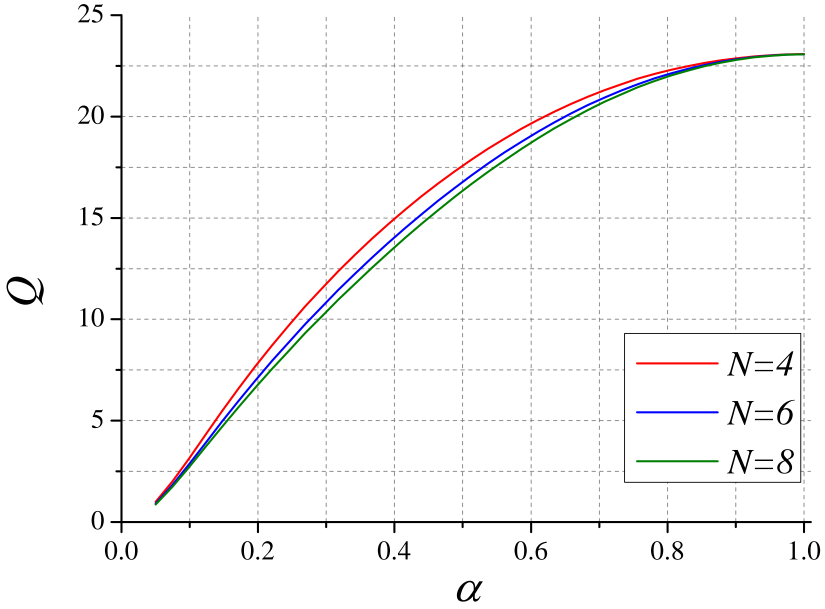

Figure 3.19: Quality factor as a function of α and for $N = 4, 6, 8$.

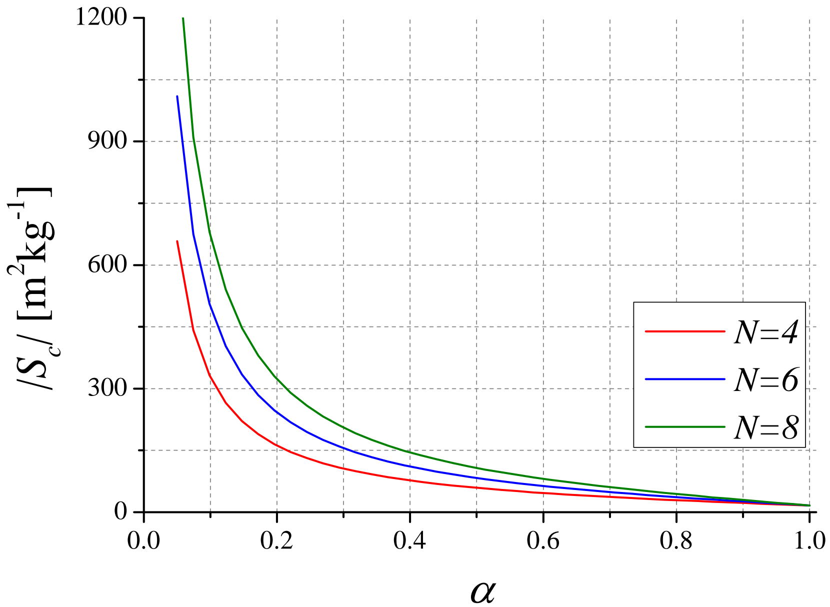

Figure 3.20: Concentration sensitivity module as a function of α and for $N = 4, 6, 8$.

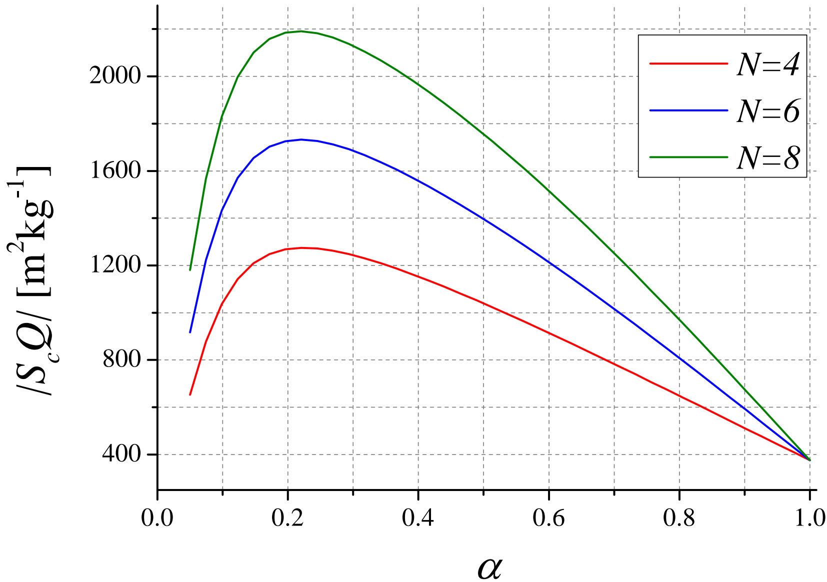

Figure 3.21: Module of the S_cQ product as a function of α and for N = 4, 6, 8. As it has been argued in section 2.3, this quantity is related with the resonant sensor limit of detection.

for Q must also be ascribed to the well known limits of flexural resonators, which rarely have been found to have in air quality factors above few hundreds. This limit is very marked in the TRONICS technological process considered here (see the Q value for $\alpha = 1$ in the plot of figure 3.19), due to the high structural thickness $h = 60\,\mu\mathrm{m}$ which results in a exceptionally high damping coefficient. Once that both S_c and Q can be estimated with varying of the holes matrix geometry, it is very interesting to investigate the trade-off between these two parameters by looking at the $|S_cQ|$ product reported in figure 3.21. This value as a very important meaning, since it has been related to the sensor limit of detection (see section 2.3). The graph of figure 3.21 states that, even considering the detrimental effect over Q, perforations are still sharply advantageous in terms of limit of detection, at least until holes dimension becomes too big ($\alpha \leq 0.3$) and shear effects arises. As it has already been affirmed in section 2.4.3 the estimation of Q presented here cannot be assumed as accurate, therefore these aspects deserve an extensive experimental evaluation. Finally is important to highlight that one of the main limits of beam based sensors is the small design space available once that the layout rules are introduced. This aspect has been omitted from the previous plots, but is very well testified by the small N and α covered ranges of the designed beams reported in tables 3.3 and 3.5.

3.4 Measurements

In this section preliminary measurements carried out over resonant beams fabricated with the TRONICS process will be presented. After a brief description of the measurement setup, the method used to isolate the motional contribution from the total signal, where a strong feedthrough is present, will be described. Resonance frequencies and quality factors will be finally extracted for the motional signals through a nonlinear fitting, a comparison of the resonance frequencies with FEM simulations an the analytical model of equation (3.35) will be made.
The measured beams are beams 2 and 3 of table 3.3. Micrograph images of beam 2 are reported in figures 3.22 and 3.23. From such images, acquired with larger magnification, devices dimensions reported in table 3.6 have been obtained. These values differ slightly from the layout ones of table 3.3 due to process variations.

name	L [µm]	w [µm]	N	α
B2	1401.1	38.9	4	0.356
B3	1401.1	46.9	4	0.282

Table 3.6: Dimensions of the measured beams fabricated with TRONICS technological process described in section 3.2. Dimensions have been extracted from micrograph images.

Resonance peaks have been measured using the two-port open loop setup of figure 2.19. The small signal driving and the short circuit current sensing have been performed using the Agilent E5061B network analyzer, the DC biasing with the Agilent E3646A power supply. A schematic of the measurement setup is shown in figure 3.24. The contribution to the capacitance on the output path, which is needed in the following for the expression of the output signal, is shown in the same figure. The measure performed by the instrument gives amplitude and phase of the frequency response $H(j\omega)$:

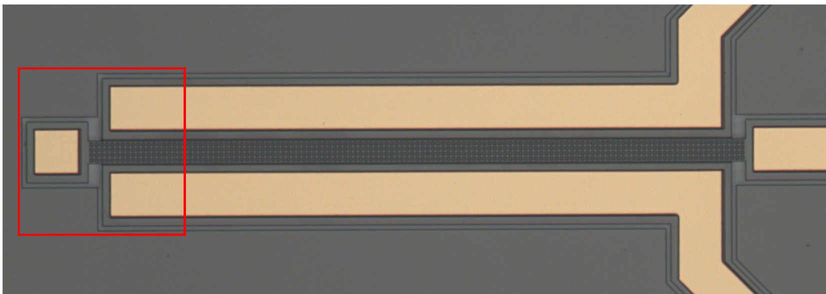

Figure 3.22: Optical micrograph of beam 3.

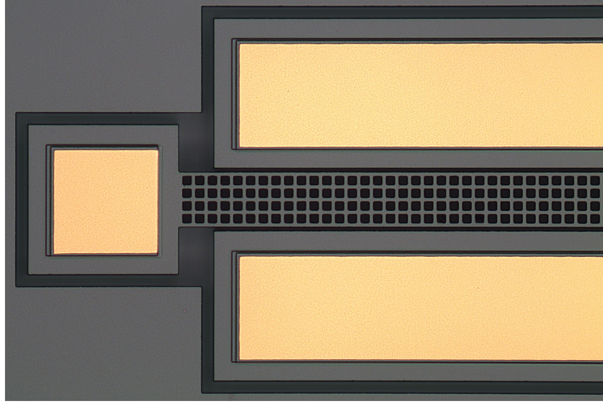

Figure 3.23: Optical micrograph of beam 3 (detail).

$$H(j\omega) = \frac{V_T(j\omega)}{V_R(j\omega)} \tag{3.42}$$

The typical approach to measure the short circuit current is to use the output port (T port) of the network analyzer in the $50\,\Omega$ configuration and measure the voltage drop that I_{out} generates while flowing through this resistor. However, due to the large actuation gaps and poor quality factors, the motional current is very weak ad thus it has been preferable to operate with the network analyzer terminals (T and R ports) both in the $1\,\mathrm{M\Omega}$ configuration. The capacity seen from the output electrode C_{tot} has several contributions: package (C_{pk}), PCB (C_{PCB}), coaxial cable (C_{coax}), input port of the network analyzer (C_{NA}) and finally the only contribution ascribable to the MEMS structure, the static capacitance C_0.

$$C_{tot} = C_{pk} + C_{PCB} + C_{coax} + C_{NA} + C_0 \tag{3.43}$$

Before acquiring the beam resonant peak, the total capacitance on the output electrode is measured by using C_{tot} as the capacity of an R-C filter built with an external resistor. The value of C_{tot} can be obtained with good accuracy by fitting the single-pole low pass frequency response of this circuit. Having a typical value in the order of $100\,\mathrm{pF}$, at the resonance frequency C_{tot} has an impedance well below $1\,\mathrm{M\Omega}$:

$$\frac{1}{\omega_0 C_{tot}} \ll 1\,\mathrm{M\Omega} \tag{3.44}$$

therefore the total current flows through C_{tot} and the output voltage V_T is proportional to the modal displacement instead that to the modal velocity. The measured resonance frequency response can thus be written as the product of the resonator total transconductance Y_t (see equation 2.25) with the impedance of the total capacitance:

$$H(j\omega) = \frac{1}{j\omega C_{tot}} Y_t(j\omega) \tag{3.45}$$

Amplitude and phase of the frequency response acquired from beam 3 at different bias

voltages are shown in figures 3.25 and 3.26 respectively. As it can be seen, parasitic effects are important and need to be cancelled in order to easily extract the resonator characteristic parameters from the measure. When the resonator is biased with $V_{DC} = 0\,\mathrm{V}$ there is no motional current and the circuit is a capacitive divider between C_{ft} and C_{out}:

$$H(j\omega)|_{V_{DC}=0} = H_0(j\omega) = \frac{C_{ft}}{C_{ft} + C_{tot}} \simeq \frac{C_{ft}}{C_{tot}} \tag{3.46}$$

By using equation (3.46) and the amplitude measured at $V_{DC} = 0\,\mathrm{V}$ presented in figure 3.25:

$$20 \log \left(H_0(j\omega)\right) \approx -76.5\, dB \tag{3.47}$$

the parasitic feedthrough capacitance can be estimated:

$$C_{ft} = C_{tot} \cdot 10^{\frac{H_0}{20}} \tag{3.48}$$

For the measure reported in this section the total capacitance was found to be $C_{tot} \approx 74.9\,\mathrm{pF}$, giving a parasitic feedthrough of $C_{ft} = 11.2\,\mathrm{fF}$. In most of the cases, once that C_{ft} is known the motional current can be extracted from the total signal with acceptable

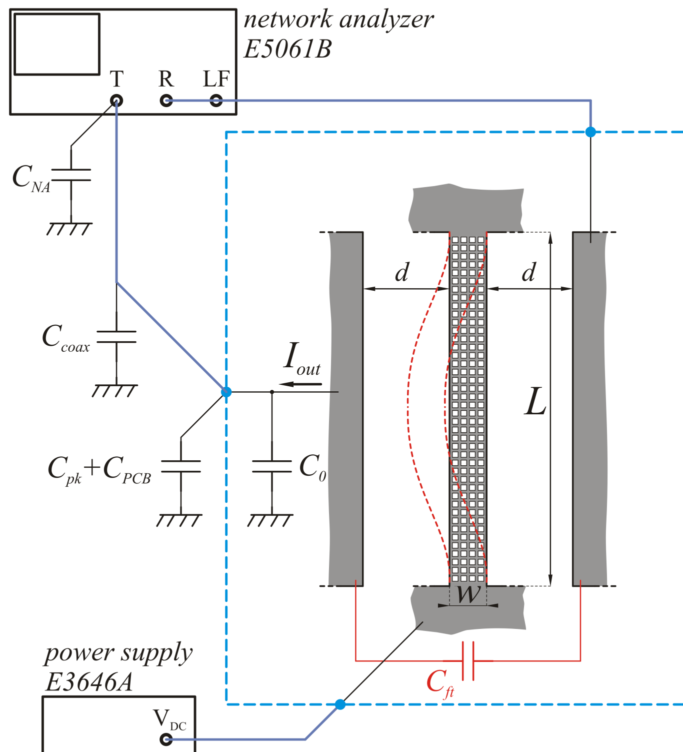

Figure 3.24: Measurement setup used. The parasitic capacitance contributions on the output path are shown, as well as the parasitic feedthrough C_{ft}.

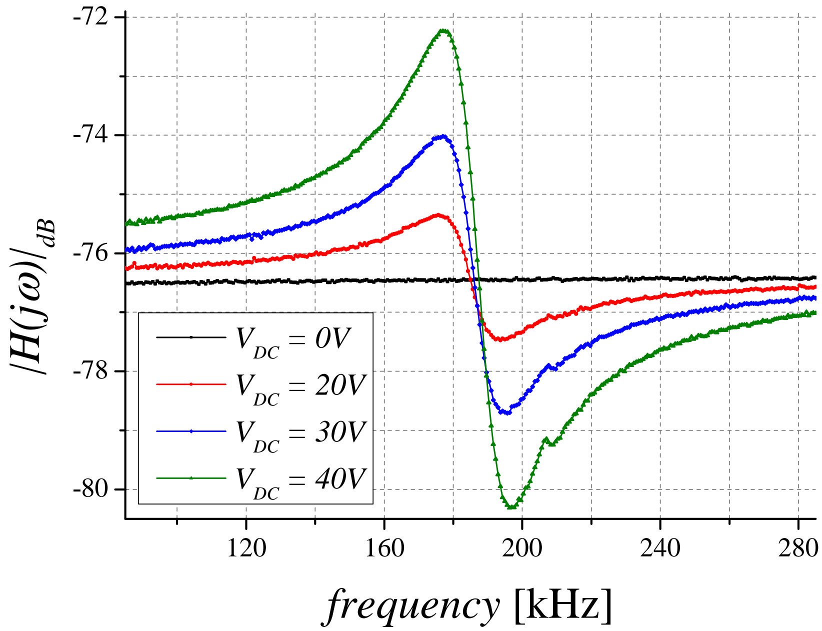

Figure 3.25: Measured amplitude of $H(j\omega)$ for various values of the bias voltage V_{DC}.

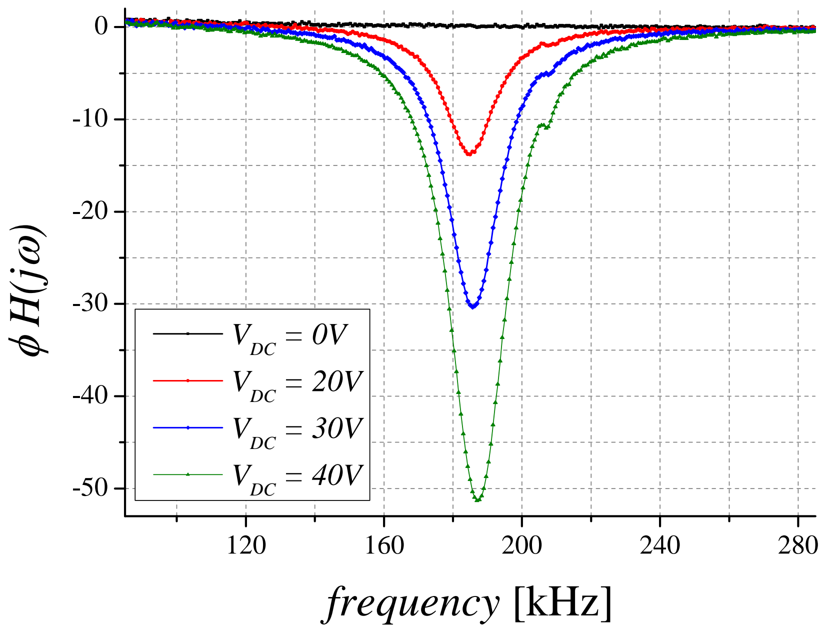

Figure 3.26: Measured phase of $H(j\omega)$ for various values of the bias voltage V_{DC}.

accuracy. For the considered measures the very low Q spreads the peak over a wide frequency range and second order effects are not negligible (i. e. the frequency response for $V_{DC} = 0\,\mathrm{V}$ is not flat). In order to obtain a more accurate peak, the motional part of the frequency response H_{mot} can be isolated by using H_0 response as a complex baseline:

$$H_{mot}(j\omega) = H(j\omega) - H_0(j\omega) \tag{3.49}$$

The motional frequency response relative to the $V_{DC} = 40\,\mathrm{V}$ measure, as well as the nonlinear fitting used to extract the resonator parameters are reported in figure 3.27. Using the same approach, beam 2 has been measured and the results are shown in figure 3.28. A comparison between of the resonance frequencies obtained from the measure, the equivalent shear model and FEM simulation is reported in table 3.7 for both beams. While the explored range of α is very small, the agreement between the experimentally determined frequencies and those obtained by our model is remarkable, and is comparable to that of FEM simulations.

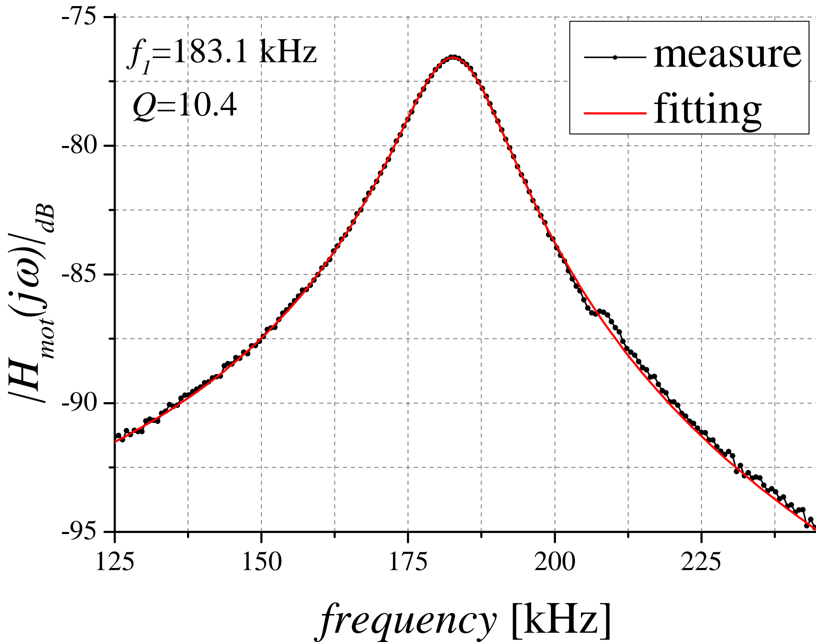

Figure 3.27: Amplitude of the motional frequency response $H_{mot}(j\omega)$ obtained subtracting the complex baseline H_0 from the $V_{DC} = 40\,\mathrm{V}$ measure of figure 3.25. The nonlinear fit used to extract resonance frequency and quality factor is also shown.

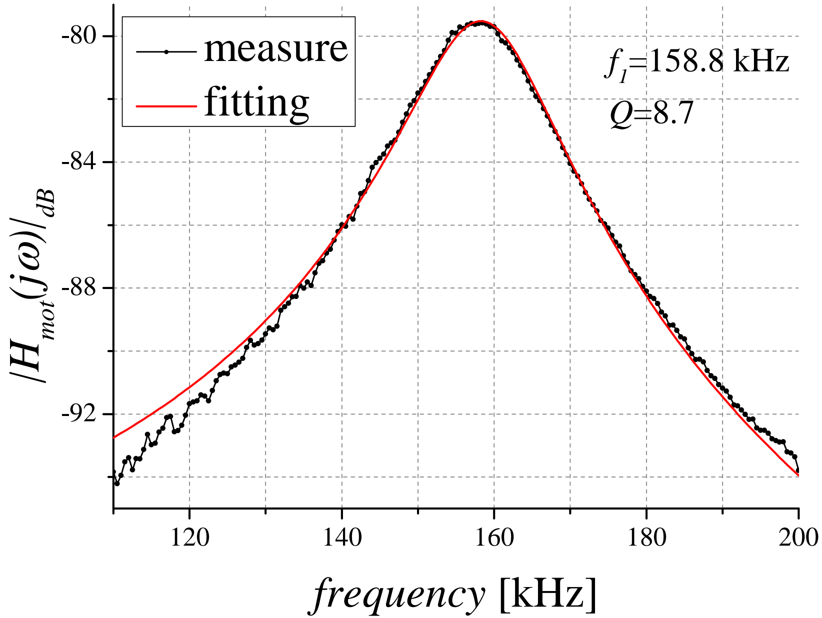

Figure 3.28: Amplitude of the motional frequency response $H_{mot}(j\omega)$ of beam 2 with $V_{DC} = 40\,\text{V}$. The nonlinear fit used to extract resonance frequency and quality factor is also shown.

	measure (kHz)	model (kHz)	FEM (kHz)
beam 2	158.8	159.1	157.7
beam 3	183.1	182.3	182.2

Table 3.7: Comparison of the resonance frequencies obtained from experimental data, from the shear equivalent model, and from FEM simulations.

4

Resonant Lamé sensor

In this chapter the project of a resonant sensor vibrating on the Lamé mode will be described. The discussion will start off with a short introduction of the Lamé resonance mode and its advantages with respect to flexural modes such as the ones presented in the previous chapter. Thereafter the structure of the chapter will fundamentally follow the one of chapter 3: in section 4.1 perforations will be introduced on the resonator and a model to estimate their effect over the resonance frequency will be developed. In section 4.2, dimensions of Lamé resonators, designed using the same technological processes used for the beams (see section 3.2) will be listed. Finally, in section 4.3, the resonance frequency model, jointly with the damping models presented in section 2.4, will be used to estimate the other resonance sensor meaningful parameters.
The Lamé resonator falls into the so-called category of bulk resonators, which have been subject of a growing interest in the last years. The name bulk resonators has not a rigorous meaning, since it is typically associated to any type of resonator not exploiting flexural, beam-like resonance modes. Because of their simple fabrication and modelling, beam-like resonators, also called flexural resonators, have been historically the first type of resonators studied and designed in the MEMS field. The recent effort in developing bulk resonators arises form the intrinsic limits of flexural resonators, such as poor quality factors and power handling and low resonance frequencies not suited for radio frequency applications. From the point of view of the resonance sensing application considered in this work, the only important advantage in using a Lamé resonator with respect to flexural one, is the dramatical increase in quality factor. Quality factors of flexural resonators operating in air rarely exceeds few hundreds, while bulk resonator operating at the same conditions have quality factors in the range of several thousands or even tens of thousands. Regarding the particular case of electrostatic actuation, another advantage in using a Lamé mode shape arises from having four electrodes where actuation an sensing can take place. This property, which will not be exploited in this work, since characterization of these resonators is still ongoing, is essential in the development of an efficient readout scheme, as it allows the use of unconventional actuation and sensing mechanisms, resulting in a dramatic decrease of parasitic effects [67, 68, 69]. Finally, as

it will be shown in the following, another advantage of this type of resonators, which is closely connected with the particular approach developed in this work, is that the Lamé resonance frequency is sharply less influenced by the holes than flexural resonators resonance frequency. A full Lamé resonator, together with a qualitative representation of the deformed shape, as well as the anchors needed to fix the structure to the substrate, is represented in figure 4.1. For a full Lamé resonator, the resonance frequency f_l can be calculated with a closed form and exact expression [120, p.35]:

$$f_l = \frac{1}{\sqrt{2}L}\sqrt{\frac{G_d}{\rho}} \tag{4.1}$$

where L is the side of the square, ρ is the material density and G_d is the material shear modulus computed in the direction of the square diagonal. The latter clarification is needed only if the resonator material is anisotropic, as in the case of a structure made of single crystal silicon. However, it is plain that, once the holes matrix is drawn on the structure, the elastic properties are no more isotropic, whether if the material in the filled parts is isotropic or not. As it will be shown in section 4.1, for a large number of holes, the elastic properties of the perforated structure can be approximated with the ones of an equivalent material with cubic anisotropy, which is, by chance, the same anisotropy of single crystal silicon. Referring to the coordinate system of figure 4.1, the deformed shape of the Lamé mode is [120, p.35]:

$$\mathbf{U_l}(x,y) = \begin{Bmatrix} U_x(x,y) \\ U_y(x,y) \end{Bmatrix} = U_0 \begin{Bmatrix} -\sin\left(\frac{\pi x}{L}\right)\cos\left(\frac{\pi y}{L}\right) \\ \cos\left(\frac{\pi x}{L}\right)\sin\left(\frac{\pi y}{L}\right)) \end{Bmatrix} \tag{4.2}$$

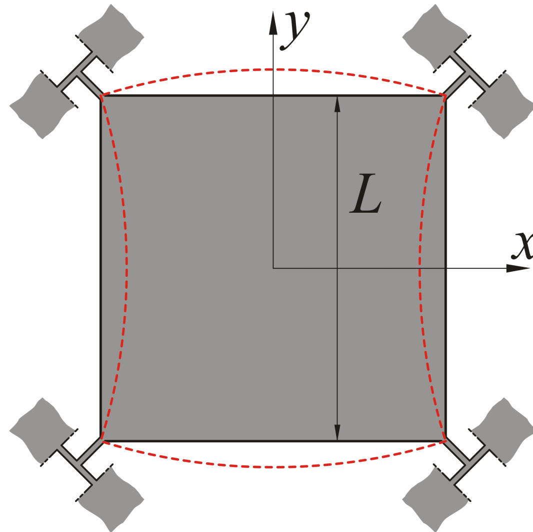

Figure 4.1: Schematic of a full Lamé resonator, the deformed shape is shown in red.

where U_0 is an arbitrary real constant.

4.1 Analytical model for the resonance frequencies

In this section, an analytical model for the resonance frequency of square perforated Lamé resonators will be developed. A schematic of the perforated resonator in reported in figure 4.2, the holes geometry is the one described in figure 2.3 and section 2.1 and already used for the perforated beams of chapter 3. By looking at the expression 4.1 for the resonance frequency of a full resonator, it is clear that, in order to develop a model that takes into account the effect of the holes over f_l, expressions for the equivalent diagonal shear modulus G_{d-eq} and equivalent mass density ρ_{eq}, are needed. Following the same approach used in section 3.1, where the analytical model for the resonance frequencies of perforated beams was developed, the following subsections will introduce the equivalent models for the mass density ad diagonal shear modulus in presence of perforations. Thereafter these models will be putted together in order to write a closed form expression for the resonance frequency of the perforated Lamé resonator.

4.1.1 Perforated material equivalent parameters

Equivalent mass density

The model for the equivalent mass density is very simple. As the typical side of Lamé resonators is several hundreds of microns long, the number of holes along it can be

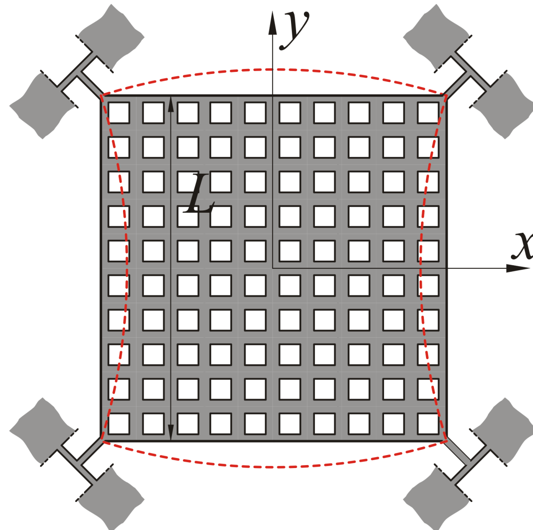

Figure 4.2: Schematic of a Lamé resonator with a pattern of square perforations. Holes geometry is described in figure 2.3 and section 2.1.

sharply increased with respect to the case of beams, where, in practical designs, N was limited to few units (see tables 3.3 and 3.5). As it will be shown in section 4.2, where the dimensions of the designed Lamé resonators will be summarized, N is constantly below 10 and reaches a maximum of 30. As N is so big, boundary effects can be neglected and the equivalent mass density can be computed on the single cell. A straightforward computation gives:

$$\rho_{eq} = \rho\alpha\,(2-\alpha) \tag{4.3}$$

Since the effect of the finite number of holes in neglected, the obtained expression for the equivalent mass density ρ_{eq} is, in contrast with the equivalent mass per unit length ρA_{eq} of the perforated beam (equation 3.24), independent from N.

Equivalent diagonal shear modulus

The computation of the equivalent diagonal shear modulus G_{d-eq} is sharply more complex than the just exposed one for the equivalent mass density. As in the case of the equivalent bending stiffness of perforated beams, different expressions for G_{d-eq} can be obtained through different assumptions over the stress distribution in the perforated Lamé resonator. In the following, three models, based on three different stress assumptions, will be used to obtain an expression for the diagonal shear modulus in presence of perforations: the *network model*, the *geometric model* and the *equivalent model*. The first is directly derived from the so-called cellular material theory, the second is a straightforward extension of the model with the same name described in the equivalent bending stiffness discussion of section 3.1.1, and the last one is an original model proposed in this section, aimed at overcoming the limits of the previous two. Moreover, it will be also shown that the model for the equivalent diagonal shear modulus G_{d-eq} can be related to two models: one for the equivalent Young's modulus E_{eq}, and one for the equivalent Poisson's ratio ν_{eq}. While the relationship between G_{d-eq} and E_{eq} is linear, the dependence of G_{d-eq} from ν_{eq} is very poor. For this reason, only the simple expression using the *network model* will be derived for ν_{eq} and will be assumed as a fair model for this parameter, while all the three models will be used in order to compute an accurate expression for the more important E_{eq} parameter.

Network model

The study of the elastic properties of regularly perforated structures falls under the name of cellular material theory [111, 121]. The square perforations arranged over a square matrix, such as the ones considered in this thesis, are one of the most simple and often studied geometry. Unfortunately, for the aim of this theory, only the case of extremely empty structure ($\alpha \to 0$) is of interest. The computations carried out in these works take advantage of this strong hypothesis under which the structure can be see as a network of slender beams hinged together. Therefore, the standard beam theory can be exploited in order to model the deformation of the single cell and, as a consequence, of the whole structure. Using the notation of this thesis, the assumption of slender beam

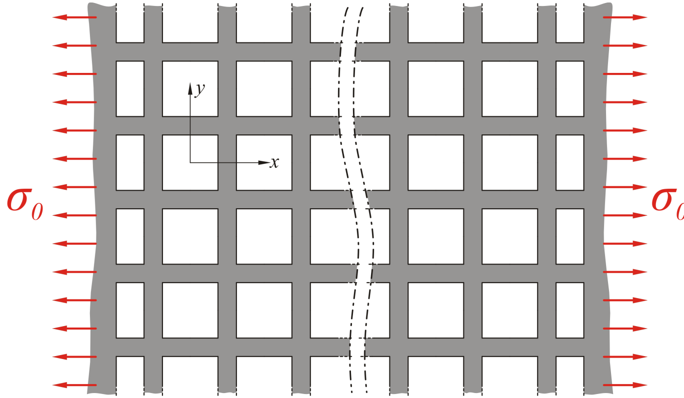

Figure 4.3: Traction problem used to computed the equivalent parameter of the perforated material.

network (beam aspect ratio below 10) would limit the describable holes geometry to a poor $\alpha \lesssim 0.1$. For the just exposed reason, cellular material models are not suited for the purpose on this section, where the holes geometry needs to be swept ideally in the whole range $\alpha \in (0, 1]$. However, for the purpose of comparison, the model derived from cellular material theory will be extended to the whole range of α in the following. As it has already been outlined, once that the holes matrix is patterned on the structure, the elastic properties are no more isotropic, whether if the material in the filled parts is isotropic or not. Since the holes matrix has a square symmetry, the anisotropy will be of the cubic type (as the one of crystalline silicon). The first step in order to compute the equivalent diagonal shear modulus in presence of holes, is to recall a property of materials with cubic anisotropy:

$$G_{d-eq} = \frac{E_{eq}}{2(1+\nu_{eq})} \tag{4.4}$$

where E_{eq} and ν_{eq} are the equivalent Young's modulus and Poisson's ratio computed in the axial direction, i. e. in any direction parallel to any side of the square resonator (see figure 4.2). This equation is the same of the one that relates the three elastic properties of an isotropic material. In a material with cubic anisotropy, this relationship does not hold true if all of the three quantities are computed in the axial direction, conversely, if the shear modulus is computed at $45°$ from the axial direction, the value found verifies equation 4.4. Exploiting this result, a model for G_{d-eq} can be obtained by deriving two models, one Young's modulus E_{eq} and one for Poisson's ratio ν_{eq}, both of them computed in the axial direction. These models can be derived by considering the problem of figure 4.3: if the holes number is big enough, boundary effects can be neglected and the structure Young's modulus in the x direction can be approximated as:

$$E_{eq} \simeq \frac{l_s}{\Delta l_s}\sigma_0 \tag{4.5}$$

where l_s is the unit cell length and Δl_s is the elongation of the cell in the x direction, due to the imposed external traction σ_0. Other assumptions made in writing equation 4.5 are: $\sigma_z \approx 0$ and $\sigma_y \approx 0$, where σ_z, σ_y are the normal stresses in the z and y direction respectively. This is the same of assuming that the structure dimensions in these directions are much smaller than the one in the x direction. As in the case of perforated beams, modelling this problem is simple in the perforated sections, while some careful considerations are needed in the filled ones. The stress in the perforated section is reported in figure 4.4, by considering the continuity of the force along the x direction, the stress value σ_h can be computed:

$$\sigma_h = \frac{\sigma_0}{\alpha} \tag{4.6}$$

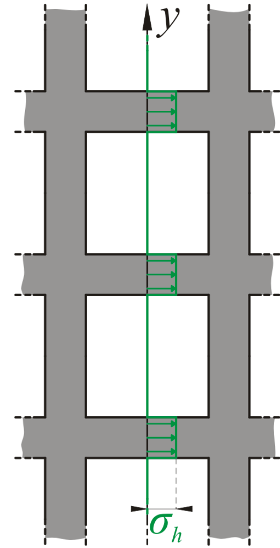

Figure 4.4: Stress in the perforated section.

When the hypothesis of slender beams network is verified, the effect of the filled sections in negligible and the knowledge of the stress distribution in the perforated sections is enough in order to compute the equivalent Young's modulus and Poisson's ratio of the structure. The network model derived in this paragraph extends this result to the whole α space by assuming that the stress distribution in the unit cell is the one of figure 4.5. As it the case of the flexural stiffness of perforated beams, where the bending of the structure was modeled by con-

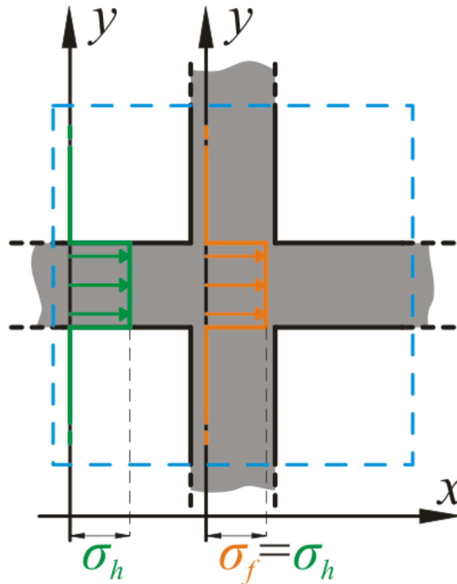

Figure 4.5: Unit cell stress distribution using the *network model*.

sidering the bending of those material fibers which extend through its whole length, the elongation of the unit cell can be computed by considering the elongation of the material fibers which extend through the whole length of the unit cell (and thus of the whole structure). By exploiting the constitutive equation of the material, Δl_s can be written as:

$$\Delta l_s = \frac{l_s}{E}\sigma_h = \frac{l_s}{E}\frac{\sigma_0}{\alpha} \tag{4.7}$$

where E is the Young's modulus of the material constituting the filled parts of the structure. By substituting this expression in equation (4.5), the equivalent Young's modulus of the *network model* E_{nw}, is found:

$$E_{nw} = \alpha E \tag{4.8}$$

Because of the rough assumption made in the stress distribution of the unit cell of figure 4.5, this model is expected fail for large values of α, in particular, it will underestimate the real Young's modulus of the structure. However, the error have to tend to 0 when the structure is full ($\alpha = 1$), since the derived model is consistent with this case. Using similar arguments, the Poisson's ratio in the network approximation is found to be:

$$\nu_{nw} = \alpha \nu \tag{4.9}$$

As it has already been outlined, and can be now justified by looking at equation (4.4), the dependence of the diagonal shear modulus from the Poisson's ratio is poor. Typical values of the Poisson's ratio of filled materials are around 0.25 and these values are expected to decrease with the grow of the holes size (as it is shown by equation (4.9)), which entails a decrease in the above mentioned relationship. For this reason, even if the approximation of the Poisson's ratio of equation (4.9) is rough as it is the one of the Young's modulus (4.8), ν_{nw} is a good model when the computation of the diagonal shear modulus is considered. The expression of the equivalent diagonal shear modulus using the *network model* G_{d-nw} is found by substituting equations (4.8) and (4.9) into the expression (4.4):

$$G_{d-nw} = \frac{\alpha E}{2(1+\alpha\nu)} \tag{4.10}$$

For a detailed treatise on cellular materials models, the reader is referred to the references [111, 121].

Geometric model

Another possible model for the equivalent Young's modulus is the *geometric model*, whose name remarks its analogy with the one developed for the flexural rigidity of perforated beams in section 3.1.1. Recalling that discussion, the stress distribution in each section is the one that the section would experience if it would has been part of a constant section structure. Therefore the stress in the perforated section will have the same distribution shown in figures 4.4 and 4.6, where $\sigma_h = \sigma_0/\alpha$, while the filled sections will have a constant stress distribution with $\sigma_f = \sigma_0$. The just described distribution assumed

by the *geometric model* is reported for the unit cell in figure 4.6. Using this model the unit cell elongation can be written as:

$$\Delta l_s = \Delta h_s + \Delta t_s = \frac{h_s}{E}\sigma_h + \frac{t_s}{E}\sigma_0 = \left(\frac{1-\alpha}{\alpha E} + \frac{\alpha}{E}\right) l_s \sigma_0 \tag{4.11}$$

where in the last equality the expressions of the cell dimensions $t_s = \alpha l_s$, and $h_s = (1-\alpha) l_s$, as well as the expression of stress in the perforated sections $\sigma_h = \sigma_0/\alpha$ have been used. Substituting the elongation of equation (4.11) in equation 4.5, the expression of the Young's modulus of the perforated material using the *geometric model* E_{geom}, is found:

$$E_{geom} = \left(\frac{1-\alpha}{\alpha E} + \frac{\alpha}{E}\right)^{-1} \tag{4.12}$$

The obtained expression is in close analogy with the expression of the equivalent flexural rigidity of the perforated beam (3.12) derived using the same model. For the same reasons putted forward when dealing with the perforated beam problem, the *geometric model* is not an accurate model for the stress distribution in the perforated structure, in particular, it will overestimate the real Young's modulus of the perforated structure. However, as in the case of the *network model*, it will be used for comparison in section 4.1.3, where a FEM validation will be carried out. The expression of the equivalent diagonal shear modulus using the *geometric model* G_{d-geom} is found by substituting equation (4.8) in expression (4.4):

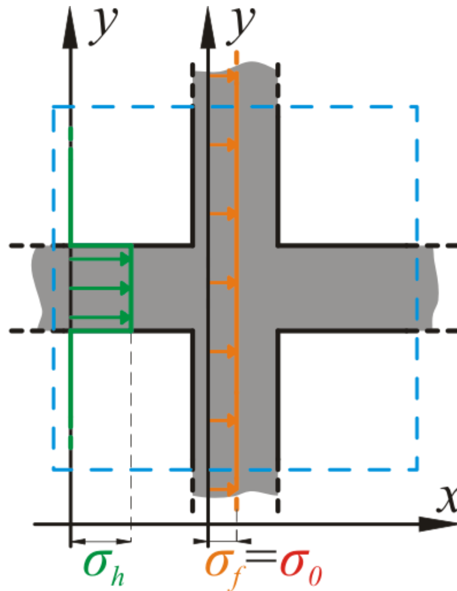

Figure 4.6: Unit cell stress distribution using the *geometric model*.

$$G_{d-geom} = \frac{\left(\frac{1-\alpha}{\alpha E} + \frac{\alpha}{E}\right)^{-1}}{2(1+\alpha\nu)} \tag{4.13}$$

where, as it has been argued in the previous paragraph, the assumption $\nu_{eq} = \alpha\nu$ has been used as a good model for the equivalent Poisson's ratio.

Equivalent model

Up to this time, the equivalent Young's modulus of the perforated structure of figure 4.3 has been modeled using two simple approximations, which leaded to the *network model* and *geometric model* of equations (4.8) and (4.12), and to their related expressions for the equivalent diagonal shear modulus. These expression are of interest since appear in the formula (4.1) for the Lamé resonance frequency. Both these models will be found inaccurate in section 4.1.3, when used to estimate the resonance frequencies of perforated Lamé resonators. In order to overcome these limits, in the following of this paragraph, an original approach, called *equivalent model*, aimed at an accurate estimation of the Young's modulus of the perforated structure, will be presented. As it is clear after the discussion expounded above, and in section 3.1.1 when dealing with perforated beams, the inaccuracy of both the previously presented model lies in the stress distribution in the filled section. For having a more accurate model for the stress in these sections, a stress analysis in an area of the filled section centered at the joint, as it is shown in figure 4.8, can be carried out.

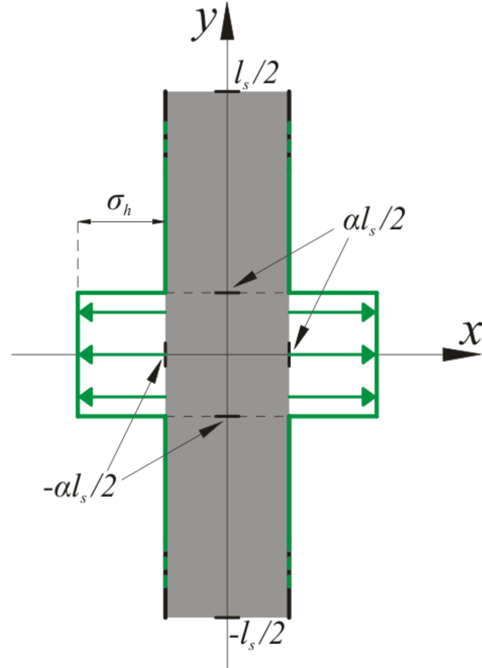

Figure 4.7: Magnification of the area where the stress analysis is performed. The coordinate system used in the computations and the traction boundary conditions are also shown.

This area, centered in the reference system used in the following computations, is magnified in figure 4.7. Boundary tractions exerted on the area by the perforated sections on its sides are also shown in the figure. Assuming that the material constituting the filled parts of the structure is isotropic and no body forces are present, the stress field equations can be summarized in the biharmonic equation [122, p.133]:

$$\frac{\partial^4 \phi(x,y)}{\partial x^4} + 2\frac{\partial^4 \phi(x,y)}{\partial x^2 \partial y^2} + \frac{\partial^4 \phi(x,y)}{\partial y^4} = 0 \tag{4.14}$$

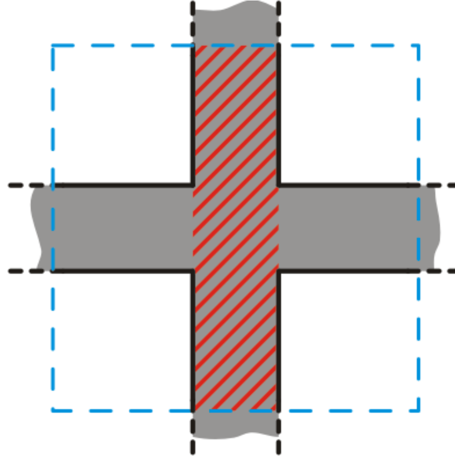

Figure 4.8: Unit cell. The area where the stress analysis is performed in order to derive the *equivalent model*, is highlighted in red.

where $\phi(x, y)$ is the biharmonic function, whose derivative are the stress components of the plane problem:

$$\sigma_x = \frac{\partial^2\phi(x,y)}{\partial y^2} \qquad \tau_{xy} = -\frac{\partial^2\phi(x,y)}{\partial x\partial y} \qquad \sigma_y = \frac{\partial^2\phi(x,y)}{\partial x^2} \tag{4.15}$$

The solution strategy adopted is the one presented in [122, p.154]: some ad-hoc terms of the general solution of (4.14) are taken with their relative degrees of freedom, these degrees of freedom are thus used to satisfy the boundary conditions. If all the boundaries are specified, the uniqueness theorem [122, p.108] can be exploited and the solution found is unique. In the case considered in this section, only the traction along the x direction is imposed while the others stress components are unspecified. The most reasonable assumption is to put these components at zero along the boundaries of figure 4.7:

$$\sigma_x(\pm\frac{\alpha l_s}{2}, y) = f_{\sigma_x}(y) \qquad \tau_{xy}(\pm\frac{\alpha l_s}{2}, y) = 0$$

$$\sigma_y(x, \pm\frac{l_s}{2}) = 0 \qquad \tau_{xy}(x, \pm\frac{l_s}{2}) = 0 \tag{4.16}$$

where $f_{\sigma_x}(y)$ is the function representing the traction boundary of figure 4.7. For the following computations is useful to expand it in a Fourieur series:

$$f_{\sigma_x}(y) = \sigma_h \mathrm{rect}\left(\frac{y}{\alpha l_s}\right) = \alpha\sigma_h + \sum_{m=1}^{\infty} \sigma_h \frac{2\sin(m\pi\alpha)}{m\pi} \cos\left(\frac{m2\pi y}{l_s}\right) \tag{4.17}$$

Equation (4.14) with the boundary conditions (4.16) form a problem analogous to the one solved in [122, p.154]. This solution, tough straightforward, leads to a cumbersome linear

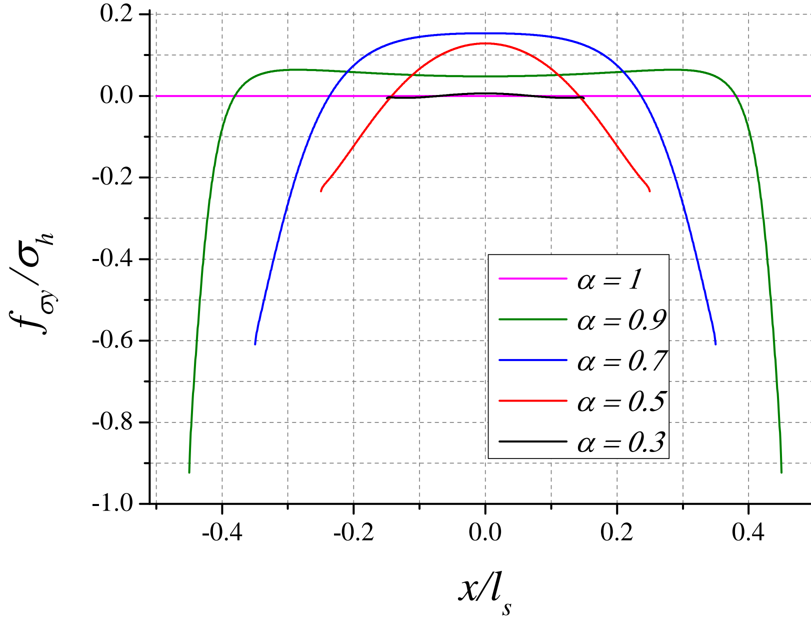

Figure 4.9: $f_{\sigma_y}(x)$ as a function of the normalized coordinate x/l_s for various values of α. The function is normalized to σ_h and truncated out of the meaningful interval $x/l_s \in [-\alpha/2, \alpha/2]$. The summation has been stopped at the tenth term.

system and no simple expression for the equivalent Young's modulus for the filled section can be extracted. The problem can be dramatically simplified if an ad-hoc boundary condition is assumed for σ_y:

$$\sigma_x(\pm\frac{\alpha l_s}{2}, y) = f_{\sigma_x}(y) \qquad \tau_{xy}(\pm\frac{\alpha l_s}{2}, y) = 0$$

$$\sigma_y(x, \pm\frac{l_s}{2}) = f_{\sigma_y}(x) \qquad \tau_{xy}(x, \pm\frac{l_s}{2}) = 0 \tag{4.18}$$

where $f_{\sigma_y}(x)$ can be written as:

$$f_{\sigma_y}(x) = \sum_{m=1}^{\infty} \frac{4\sigma_h \cos(m\pi)\sin(m\pi\alpha)}{m\pi[2m\pi\alpha + \sinh(2m\pi\alpha)]} \cdot$$

$$\left\{\cosh\left(\frac{m2\pi x}{l_s}\right)[\sinh(m\pi\alpha) - m\pi\alpha\cosh(m\pi\alpha)]\right.$$

$$\left.+2m\pi\frac{x}{l_s}\sinh\left(\frac{m2\pi x}{l_s}\right)\sinh(m\pi\alpha)\right\} \tag{4.19}$$

The plot of $f_{\sigma_y}(x)$ is shown in figure 4.9 for various values of α. As the length of the boundary where $f_{\sigma_y}(x)$ has to imposed varies with α ($x \in [-\alpha l_s/2, \alpha l_s/2]$) the function is truncated out the meaningful segment. This function appears to be a reasonable boundary, since it is even with respect to x, and has a zero integral:

$$\int_{-\frac{\alpha l_s}{2}}^{\frac{\alpha l_s}{2}} f_{\sigma_y}(x)\, dx = 0 \tag{4.20}$$

which is a needed property, since no total force is acting in the y direction. The general form of the biharmonic function considered in order to solve equation (4.14) with the boundary conditions (4.18) is:

$$\phi(x, y) = K_0 y^2 + \sum_{m=1}^{\infty} \cos(\beta_m y) \left[F_m \cosh(\beta_m x) + G_m \beta_m x \sinh(\beta_m x)\right] \tag{4.21}$$

where K_0, β_m, and the double infinity of coefficients F_m and G_m are the degrees of freedom needed to impose the boundary conditions. By imposing $\tau_{xy} = 0$ on the borders parallel to the y axis, a relationship between F_m and G_m is found:

$$F_m = -\frac{1}{2}\left[2 + l_s \alpha \beta_m \coth\left(\frac{\alpha l_s \beta_m}{2}\right)\right] \tag{4.22}$$

The remaining degrees of freedom can be obtained by applying the condition over σ_x:

$$K_0 = \frac{\alpha \sigma_h}{2} \qquad \beta_m = \frac{2\pi m}{l_s}$$

$$G_m = \frac{{l_s}^2 \sigma_h \sin(m\pi\alpha)\sinh(m\pi\alpha)}{m^3\pi^3\left[2m\pi\alpha + \sinh(2m\pi\alpha)\right]} \tag{4.23}$$

The other two boundary conditions are automatically satisfied once that the substitutions (4.22) and (4.23) are made. For the purpose of calculating the equivalent Young's modulus in the x direction, only the σ_x stress component is of interest. The final expression for this quantity gives:

$$\begin{aligned} \sigma_x(x, y) =& \alpha\sigma_h + \sum_{m=1}^{\infty} \frac{4\sigma_h \cos\left(\frac{m2\pi y}{l_s}\right)\sin(m\pi\alpha)}{m\pi\left[2m\pi\alpha + \sinh(2m\pi\alpha)\right]} \cdot \\ & \left\{\cosh\left(\frac{m2\pi x}{l_s}\right)\left[m\pi\alpha\cosh(m\pi\alpha) + \sinh(m\pi\alpha)\right]\right. \\ & \left. -2m\pi\frac{x}{l_s}\sinh\left(\frac{m2\pi x}{l_s}\right)\sinh(m\pi\alpha)\right\} \end{aligned} \tag{4.24}$$

Using this stress distribution the elongation of the unit cell can be written as:

$$\Delta l_s = \Delta h_s + \Delta t_s = \frac{h_s}{E}\sigma_h + \frac{1}{E\alpha l_s}\int_{-\frac{\alpha l_s}{2}}^{\frac{\alpha l_s}{2}}\int_{-\frac{\alpha l_s}{2}}^{\frac{\alpha l_s}{2}} \sigma_x(x,y)\,dx\,dy \tag{4.25}$$

where the elongation Δh_s of the perforated sections uses the same computations of the previous models, while the elongation Δt_s of the filled sections exploits the stress field 4.24 obtained from the just described analysis. Solving the integral and substituting $h_s = (1-\alpha)l_s$, $\sigma_h = \sigma_0/\alpha$, equation (4.25) can be rewritten as:

$$\Delta l_s = l_s\sigma_0 \left\{ \frac{1-\alpha}{\alpha E} + \frac{\alpha}{E}\left[1 + \sum_{m=1}^{\infty} \frac{8\sin(m\pi\alpha)^2\sinh(m\pi\alpha)^2}{m^3\pi^3\alpha^3[2m\pi\alpha + \sinh(2m\pi\alpha)]}\right]\right\} \tag{4.26}$$

By substituting equation (4.26) into equation 4.5, the expression of the Young's modulus with the *equivalent model* is found:

$$E_{eq} = \left\{ \frac{1-\alpha}{\alpha E} + \frac{\alpha}{E}\left[1 + \sum_{m=1}^{\infty} \frac{8\sin(m\pi\alpha)^2\sinh(m\pi\alpha)^2}{m^3\pi^3\alpha^3[2m\pi\alpha + \sinh(2m\pi\alpha)]}\right]\right\}^{-1} \tag{4.27}$$

Finally, the expression for the diagonal shear modulus using the *equivalent model*:

$$G_{d-eq} = \frac{\left\{ \frac{1-\alpha}{\alpha E} + \frac{\alpha}{E}\left[1 + \sum_{m=1}^{\infty} \frac{8\sin(m\pi\alpha)^2\sinh(m\pi\alpha)^2}{m^3\pi^3\alpha^3[2m\pi\alpha + \sinh(2m\pi\alpha)]}\right]\right\}^{-1}}{2(1+\alpha\nu)} \tag{4.28}$$

4.1.2 Expression for the resonance frequencies

In this section, the closed form expressions for the resonance frequencies of perforated Lamé resonators, using the three models presented in the previous section, will be presented. In the next section, these models will be compared with the resonance frequencies obtained through FEM simulations. The resonance frequency expressions are found by substituting the equivalent parameters derived in section 4.1.1 in the expression (4.1) for the resonance frequency of the full resonator. While the only derived equivalent mass density ρ_{eq} is the one of equation (4.3), three different models have been developed for the shear modulus G_d in presence of perforations. If the *network model* is considered, equation (4.10) have to used to model this parameter, leading to the resonance frequency expression f_{nw} using the *network model*:

$$f_{nw} = \frac{1}{\sqrt{2}L}\sqrt{\frac{G_{d-nw}}{\rho_{eq}}} \tag{4.29}$$

If equation (4.13) is used instead, it leads to the resonance frequency f_{geom} of the *geometric model*:

$$f_{geom} = \frac{1}{\sqrt{2}L}\sqrt{\frac{G_{d-geom}}{\rho_{eq}}} \tag{4.30}$$

Finally, if the expression (4.28) is considered, the expression will be one of the *equivalent model* proposed in this work:

$$f_{eq} = \frac{1}{\sqrt{2}L}\sqrt{\frac{G_{d-eq}}{\rho_{eq}}} \tag{4.31}$$

4.1.3 FEM validation

In this section, the three closed form expressions for the Lamé resonance frequency in presence of perforations, presented in section 4.1.2, will be compared with modal simulations carried out with ANSYS. Regarding the *equivalent model*, summations have been stopped at the tenth term. As an example, a Lamé resonator made of poly Silicon-Germanium, with a side $L = 400\mathrm{\mu m}$, has been considered. The holes number N has been swept from 10 to 30 with a step of 10 while α have has been swept from 0.05 to 1 with steps of 0.05. The material properties have already been reported in table 3.4, the structure is modeled under a plane stress hypothesis (negligible thickness) and meshed with the PLANE182 element. Since the models assume a large number of holes, the resonance frequency expressions (4.29), (4.30) and (4.31) are independent from N. The results can hence be plotted in the compact form of figure 4.10, where the three simulations are reported together with the three models. Plot markers are used only for simulated data for clarity. The errors of the three models with respect to FEM simulations, for the three values of N considered, are reported in figure 4.11. The *geometric model* results to be a very rough estimate of the FEM data over the whole range of α, showing with errors below $10\,\%$. As expected, both the *network model* and *equivalent model* are good approximations for low values of α, but only the latter is a good model when holes are small. Apart from having a smaller percentage error, the *equivalent model* is the only

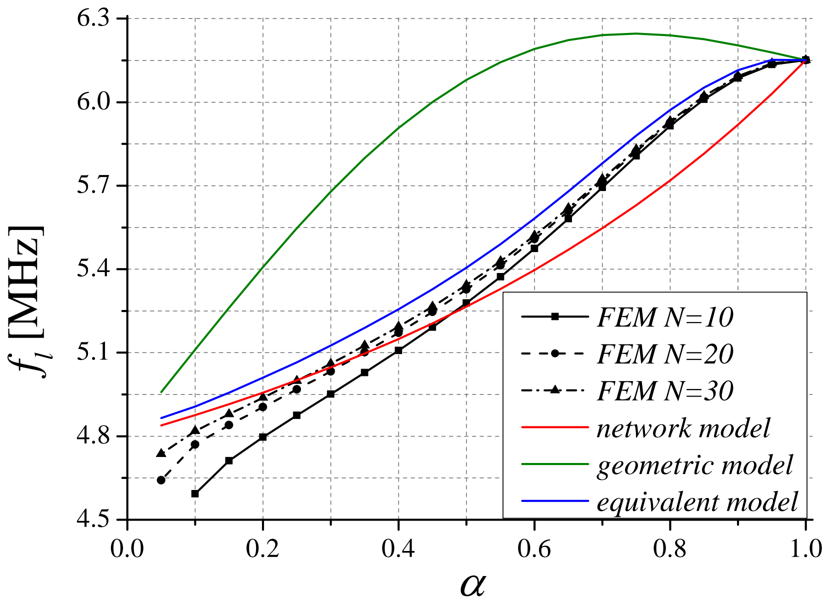

Figure 4.10: Lamé resonance frequency as a function of α for a resonator made of Silicon-Germanium with $L = 400\,\mathrm{\mu m}$. FEM simulations for three values of N considered, as well as the models (which are independent form N), are presented.

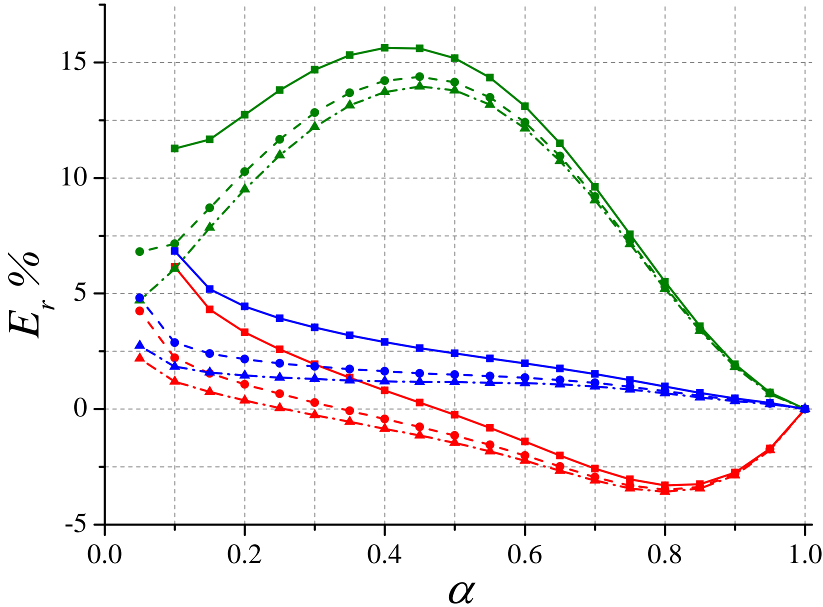

Figure 4.11: Silicon-Germanium resonator with $L = 400\,\mu\mathrm{m}$. Relative error of the models with respect to FEM simulations: *network* (red), *geometric* (green), *equivalent* (blue). Plots are shown for the three values of N used in figure 4.10 using the same markers: ■ 10, ● 20, ▲ 30.

one predicting the inflection point present in the simulations and having a decreasing error with the increasing of N over the whole range of α. Even if the *equivalent model* of expression (4.31) has been derived assuming an isotropic material as the constitutive element of the filled parts of the structure, the model shows good results if applied to perforated Lamé resonators made of Single Crystal Silicon. The comparison between models and FEM simulations, for a resonator made of [110] SCS with side of length $L = 1000\,\mu\mathrm{m}$ is shown in figure 4.12. The relative errors of the models with respect to FEM data are shown in figure 4.13. As it can be seen from these figures the model seems to work exactly in the same way when used to predict the resonance frequency of a structure made of a material with cubic anisotropy, such as SCS. A rigorous treatment of this case is still ongoing. However, the good results obtained using the isotropic model should not surprise, since the traction problem of figure 4.3, considered in extracting this model, is unidimensional and thus depending only on E and ν. Following the analysis developed in chapter 3 for the perforated beam sensor, the *equivalent model* for the Lamé resonance frequency in presence of perforations will be used in the following of this chapter to estimate viscous losses, quality factor and motional resistance of Lamé resonant sensors. However, few qualitative conclusions are already possible. As it can be assured by comparing the resonance frequency plots of this section with the ones presented for

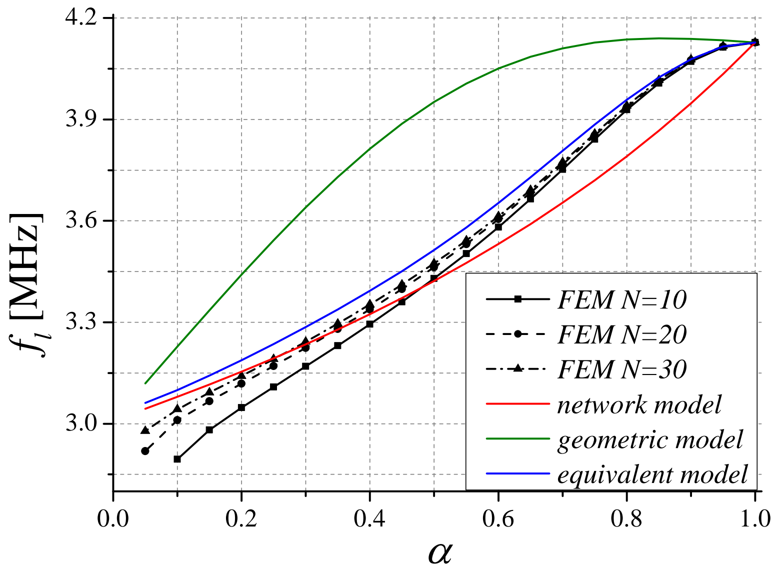

Figure 4.12: Lamé resonance frequency as a function of α for a resonator made of [110] Single Crystal Silicon with $L = 1000\,\mu\text{m}$. FEM simulation for three values of N considered, as well as the models (which are independent form N), are presented.

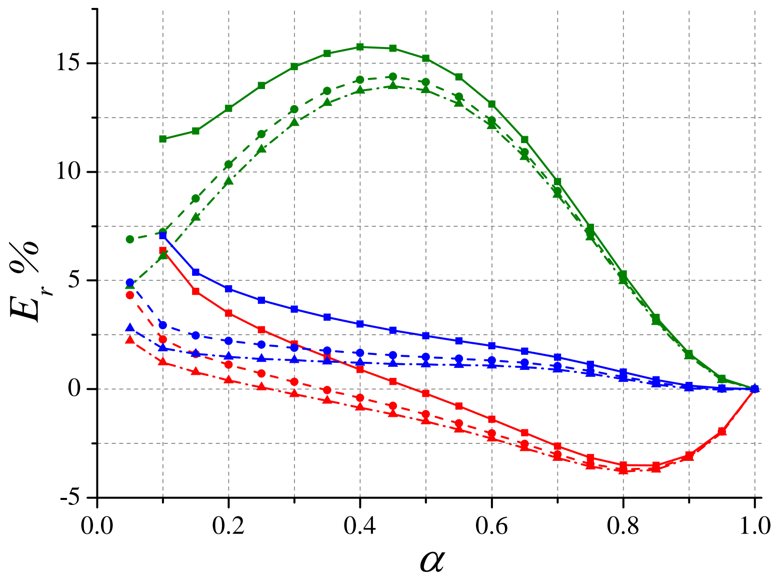

Figure 4.13: [110] Single Crystal Silicon resonator with $L = 1000\,\mu\text{m}$. Relative error of the models with respect to FEM simulations: *network* (red), *geometric* (green), *equivalent* (blue). Plots are shown for the three values of N used in figure 4.12 using the same markers: ■ 10, ● 20, ▲ 30.

the perforated beams in section 3.1.3, the resonance frequency drop due to the holes is sharply less important in the case of Lamé resonators. The resonance frequency falls of about $25\,\%$ when $\alpha \approx 0.05$ with respect to the full case. Over the same α span, the beam resonance frequency drops of about $65\,\%$. The reduced effect of the holes over the resonance frequency is a clear advantage from the resonance sensor point of view, since in mitigates the detrimental effect of the holes over the quality factor. As it will be shown in section 4.3, the quality factor of perforated Lamé resonators takes advantage also of a better starting point, i. e. the Q of the full case ($\alpha = 1$) which is several orders of magnitude bigger that its corresponding value for the full beam case. These advantages makes the Lamé topology discussed in this chapter, clearly more suited for resonance sensing than the beam topology described in chapter 3.

4.2 Designed structures

In this section the dimensions of the designed Lamé resonators will be summarized. The structures have been designed using the same technological processes used for the design of beam resonant sensors, which have already been briefly introduced in section 3.2. Therefore the section will be limited only to the list of the structures layout dimensions.

TRONICS

name	L [μm]	N	α
L1	1000	20	0.1
L2	1000	20	0.3
L3	1000	20	0.5
L4	1000	20	0.7
L5	1000	30	0.3
L6	1000	30	0.5

Table 4.1: Lamé resonators fabricated with the TRONICS process.

SiGe

name	L [µm]	N	α
L1	300	10	0.1
L2	300	10	0.3
L3	300	10	0.5
L4	300	10	0.7
L5	300	20	0.3
L6	300	20	0.5
L7	300	20	0.7
L8	400	10	0.1
L9	400	10	0.3
L10	400	10	0.5
L11	400	10	0.7
L12	400	20	0.1
L13	400	20	0.3
L14	400	20	0.5
L15	400	20	0.7

Table 4.2: Lamé resonators fabricated with the SiGe process.

4.3 Estimated resonance sensor performances

As for the case of beams resonant sensors, the effect of holes over parameters other than the resonance frequency needs to be investigated. In this section, an analysis similar to the one developed in section 3.3 for resonant beams, will be done. In order to estimate damping losses, motional resistance and quality factor of the Lamé resonator, modal parameters and electromechanical coupling coefficients of the Lamé mode are needed. Expressions for these parameters can be easily found by extending the formulas derived for the clamped-clamped beam, the *equivalent model* will be used in order to estimate the resonance frequency. As in the case of the clamped-clamped beam, the modal parameters will be firstly computed for the full resonator case, thereafter they will be extended to the case with holes through straightforward computations. The overall of this analysis will show the superior performances of the Lamé topology with respect to the beam topology discussed in chapter 3. In order to have a direct comparison with the values estimated for in the beam case, the same technological process (TRONICS) will be considered for the analysis. The same side length used in the FEM validation section 4.1.3, $L = 1000\mu\mathrm{m}$ oriented in the [100] crystallographic direction, will be considered. Regarding the holes, four different values of N, ranging from 10 to 40 with steps of 10 will be tested, α will be swept from 0.05 to 1 without considering the layout rules that limit the design space. In the following computations, the Lamé mode shape of equation (4.2) will be used. For simplicity, the multiplicative coefficient U_0, which is not a factor in any physical quantity, will be considered unitary in the following. Considering the electromechanical coupling coefficient, a first remarkable difference of the Lamé resonators with respect to the beams case is that they have four electrodes where electrostatic actuation can take place. Limi-

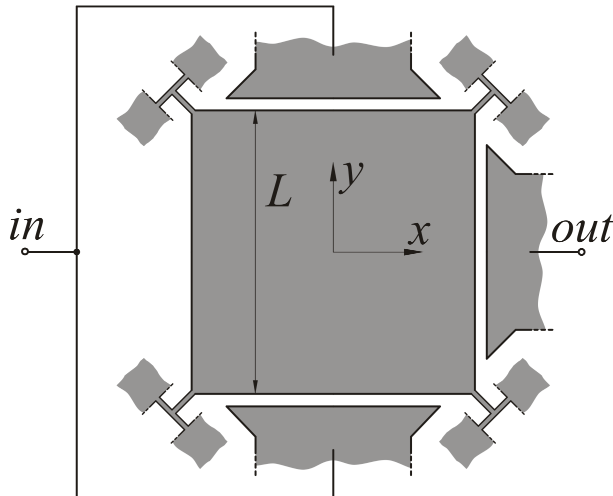

Figure 4.14: Full Lamé resonator used for the modal parameters extraction. The input and output electrodes are shown.

tations of the technological process restrict the number of electrically addressable sides of the resonators to three, therefore two of them are used for actuation an the remaining one for sensing, as it is shown in figure 4.14. Even if not exploited in this work, the presence of more than two electrodes is a first advantage of the Lamé topology, since it can be exploited for parasitic feedthrough cancellation by using unconventional actuation and detection schemes [67, 68, 69]. Considering the reference system of figure 4.14, the electrodes have a deformed shape which is an arc of cosine, making a straightforward analogy with the expression 2.45 derived for the clamped-clamped beam, the electromechanical coupling coefficient η of one electrode is:

$$\eta_l = \frac{\epsilon_0 h V_{DC}}{d^2} \int_{-\frac{L}{2}}^{\frac{L}{2}} \cos\left(\frac{\pi\xi}{L}\right) d\xi = \frac{2}{\pi}\frac{\epsilon_0 h L V_{DC}}{d^2} \tag{4.32}$$

where the electrode length has been assumed equal to L. Since two electrodes are used for actuation, the input electromechanical coefficient will be $\eta_{in} = 2\eta_l$, while $\eta_{out} = \eta_l$. If the total modal damping coefficient is c_{tot}, the motional resistance can be written as:

$$r_m = \frac{c_{tot}}{\eta_{in}\eta_{out}} = \frac{r_m}{2\eta_l^2} \tag{4.33}$$

The integral for the total damping has to contributions: one from the slide damping, which takes place over the upper and lower surfaces, and one from the squeeze damping which takes place along the three sides where the electrodes are present:

$$\begin{aligned} c_{tot} =& \int_{-\frac{L}{2}}^{\frac{L}{2}} \int_{-\frac{L}{2}}^{\frac{L}{2}} (c_{u-1s} + c_{o-1s}) \left(U_x(x,y)^2 + U_y(x,y)^2\right) dx\, dy \\ &+ 3\int_{-\frac{L}{2}}^{\frac{L}{2}} \frac{c_{sqz}}{L} \cos\left(\frac{\pi\xi}{L}\right)^2 d\xi \end{aligned} \tag{4.34}$$

where c_{u-1s} and c_{o-1s} are the slide coefficients per unit surface under and over the structure respectively (see equations (2.74) and (2.78)), c_{sqz} is the squeeze coefficient (equation (2.79)) and U_x, U_y are the x and y component of the Lamé modal shape (equation (4.2)). As in the case of beams, squeeze film damping has been considered uniformly distributed over the electrode length and thus integrated over this dimension weighted for the square of the deformed electrode shape. By solving the integrals equation (4.34) can be rewritten as:

$$c_{tot} = \frac{1}{2}\left(\underbrace{c_{u-1s}L^2}_{c_{under}} + \underbrace{c_{o-1s}L^2}_{c_{over}} + \underbrace{3c_{sqz}}_{c_{squeeze}}\right) \tag{4.35}$$

The total modal damping c_{tot} is thus half of the damping computed as if the structure would experience rigid motion. A straightforward extension to the case with perforations gives:

$$c_{tot} = \frac{1}{2}\left(\underbrace{c_{u-1s}A_{slide}}_{c_{under}} + \underbrace{c_{o-1s}A_{slide}}_{c_{over}} + \underbrace{3c_{sqz}}_{c_{squeeze}}\right) \tag{4.36}$$

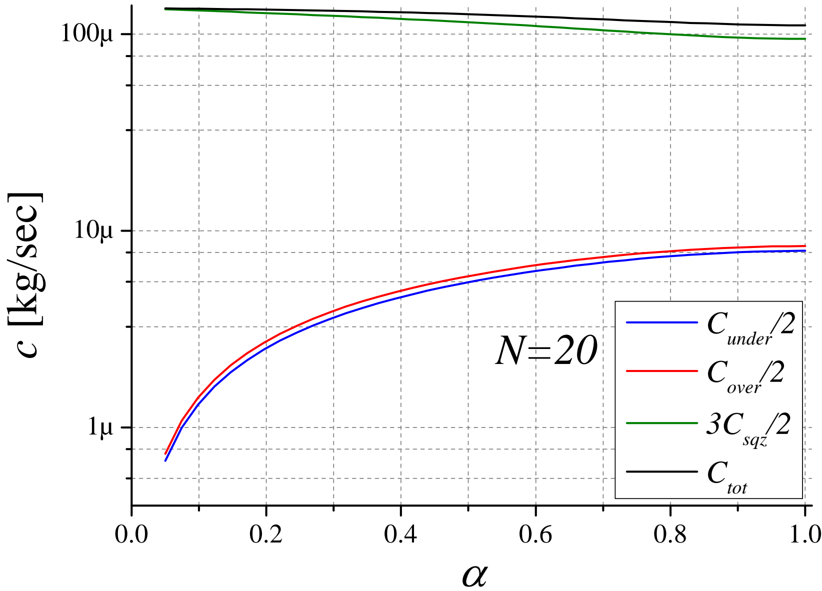

Figure 4.15: Contributions to the total modal damping c_{tot} for $N = 20$.

where A_{slide} is the surface where the slide takes place, which is the same of equation (3.37) considering $Ar = 1$. In writing equation (4.36), the same assumption used in the beam case and discussed in section 2.4.3, i. e. that the slide damping is limited to the full part of the upper and lower surface has been used. The various contributions to c_{tot}, computed at the resonance frequency for the $N = 20$ are reported in figure 4.15. The other value of N are not shown since there is no substantial difference in the results. The bigger slide surface of Lamé resonators with respect to beams, as well as a bigger resonance frequency, increase the slide effect, which plays a minimum contribution to c_{tot} when the holes are small. However, dissipation is still dominated by the squeeze contribution and thus essentially constant with α. The small variation of c_{sqz} (and thus of c_{tot}) with respect to α is due to the resonance frequency change and to the squeeze film effect approaching the compressibility limit. Considering a polarization voltage $V_{DC} = 40\,\mathrm{V}$ and using the total damping shown in figure 4.15, an estimation of r_m is found:

$$r_m \approx 112\,\mathrm{M}\Omega \tag{4.37}$$

Performing the same integration used for the slide contribution to the modal damping, the modal mass can be easily found to be half of the total mass of the structure. Therefore the modal mass in presence of holes will be:

$$m = \frac{1}{2} h A_{slide} \rho \tag{4.38}$$

Using the modal mass and damping coefficients and the *equivalent model* for the res-

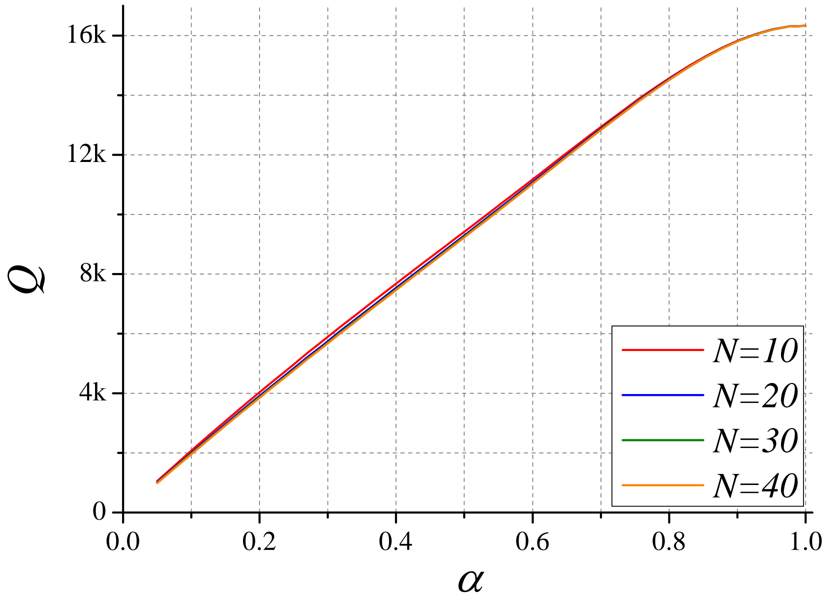

Figure 4.16: Quality factor as a function of α for $N = 10, 20, 30, 40$.

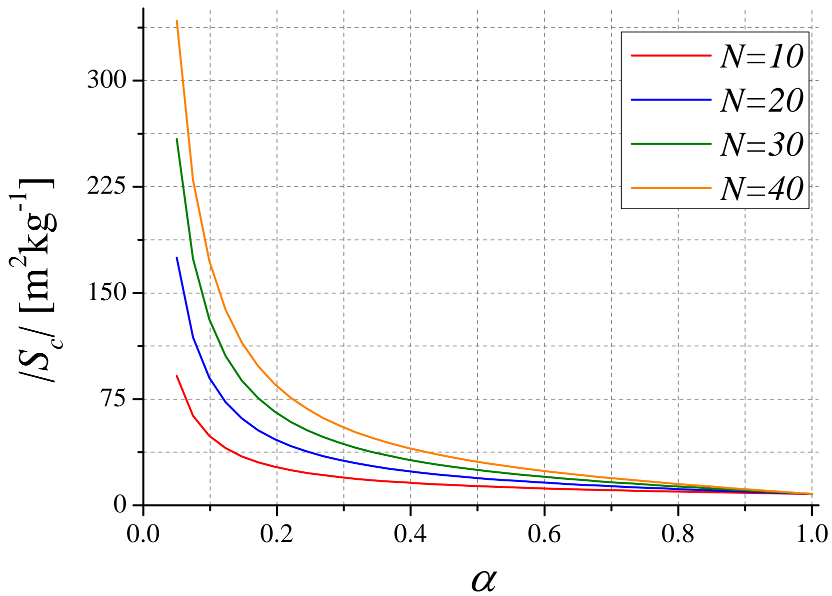

Figure 4.17: Concentration sensitivity module as a function of α for $N = 10, 20, 30, 40$.

onance pulsation, the quality factor of the Lamé resonators is estimated by using equation (2.67). The obtained values are reported in figure 4.16 for the four values of N considered. As it can be seen, Q values of the Lamé topology are about three orders of magnitude bigger than the ones reported in figure 3.19 for the beams resonators, showing a dramatic improvement. The absolute values of the concentration sensitivity, computed using equation (2.4), is shown in figure 4.17. The $|S_c|$ values obtained for the Lamé topology are smaller that the ones obtained for the beams (see figure 3.20), this is due to the aspect ratio, whose increment results in a grow of $|S_c|$. This can be seen by looking at the simplified equation (2.5) for S_{c-N}, where a proportionality relationship is shown. However, this consideration does not take into account the fact that point at very low values of α and high values of N in figure 3.20 may not be reachable due to layout rules limitation. This problem is present also in the Lamé topology, but the bigger outer dimensions mitigate it, leaving a bigger (N, α) space to be explored. This observation has a practical demonstration as the range of N and α covered by the designed Lamé resonators of tables 4.1 and 4.1, are sharply wider than the ones covered by the designed beams resonators (see tables 3.3 and 3.5). In figure 4.18, the $|QS_c|$ product is shown, the sharp improvement with respect to the beam case of figure 3.21 is clearly due to the dramatic improvement to the Q value discussed above. The other interesting fact is that, aside from the case $N = 10$, in the other cases $|QS_c|$ is always increasing with the increasing of the holes dimensions ($\alpha \to 0$). This behavior differs from the one dis-

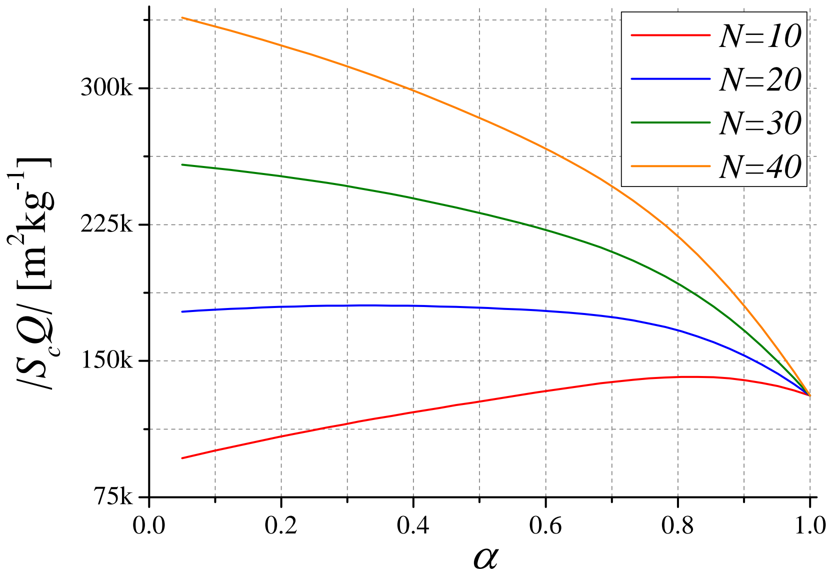

Figure 4.18: Module of the S_cQ product as a function of α and for $N = 10, 20, 30, 40$. As it has been argued in section 2.3, this quantity is related with the resonant sensor limit of detection.

played by beams, where $|QS_c|$ starts to decrease after the holes dimension have reached a limit value. In section 3.3 this detrimental effect over $|QS_c|$ has been attributed to the shear effects that affect the beam resonance frequency once that α falls below ≈ 0.3. For this reason, this effect is no more present in the Lamé topology, which exhibit a sharply more stable resonance frequency with respect to the holes size (see section 4.1.3). The section can be concluded by stating that resonant sensor exploiting the Lamé resonance mode offer several advantages with respect to the conventional flexural resonators and thus are the ones where the most of modelling and design efforts have to focused. It is also important to remark that Q estimations done with the simple models presented in this thesis have to be assumed as qualitative, therefore experimental proofs are needed in order to validate these results.

5

Phononic crystals for sensing applications

Phononic crystals (PNCs) are structures where the physical parameters affecting the propagation of vibrations, such as the mass density and the elastic moduli of a solid continuum, are periodic in one or more dimensions. As a result of this property, phononic crystals exhibit a frequency selective behavior with respect to vibration propagation. Frequency intervals, called phononic band gaps (PBGs), where the propagation of vibrations is not permitted, arise when the transmission of acoustic wave through PNCs is investigated. Inside a PBG, the acoustic wave has a wave vector with a complex part resulting in a vibration attenuation along the propagation direction. This complex component of the wave vector is not ascribable to any dissipation process experienced by the acoustic wave while traveling through the crystal. The energy is not dissipated but reflected by the crystal. Assuming to excite an acoustic wave at one side of a (finite) PNC, if the wave frequency belongs to a PBG and the crystal is long enough, no appreciable vibration will be transmitted on the opposite side, this is basically the experimental method used to evidence the presence of phononic band gaps is studied structures. The ratio of the transmitted to the incident wave, displayed as a function of the frequency, is called the transmission spectrum of the phononic crystal. The characteristic properties that phononic crystals exhibit with respect to vibration propagation can be seen as the mechanical counterpart of others well known phenomenons belonging to different physical words. Among them, probably the most important and famous is the electron propagation in solids studied by means of state solid physics. In this case, propagating electrons are described through matter waves, and the spatial periodicity of the electric potential generated by the crystal lattice, produces forbidden energy intervals (energy gaps). Another very active field of research regards photonic crystals, whose periodicity of the optical refraction index produces band gaps in the electromagnetic spectrum.
Phononic crystals are a relatively young field of research: phononic band gaps have been predicted for the first time, exploiting the above mentioned analogy with matter and electromagnetic waves, by the research group of Djafari-Rouhani [123, 124] in the early 90s. Sigalas and Economou [125, 126] also worked on this topic during the same years. In the years following these theoretical works, the experimental evidence of phononic band

gaps has been proven over several macroscopic structures. The term phononic crystal is typically used when the host material is solid, in this case, periodicity is obtained by alternating different materials, such as in [127, 128], or by drawing a pattern of empty or licquid filled holes over the structure [129, 130]. Another possible approach consists in including solid scatterers in a fluid medium, in this case the structure is somewhere named sonic crystal and its band gaps acoustic band gaps. Such structures are typically built arranging cylindrical scatterers of various materials like steel and wood in air [131, 132], but the use of water as the host medium as also been proven [133]. A review on sonic crystals can be found in [134]. The interest on these devices has steadily grown during the last years, when microfabrication and micromachining technologies allowed the realization of micro-phononic crystals, with the consequent enlargement of practical applications (see below). A review of microfabricated PNCs can be found in [135]. The standard approach to realize a PNC with micromachining techniques is to draw a pattern of holes on the structural material [136, 137, 138], however, alternative approaches, like the one reported in [139], where Tungsten scatterers are included in a Silicon oxide layer, are also possible. In all the above mentioned references spatial periodicity is typically obtained using square, triangular or honeycomb cells. The main applications of micro-fabricated PNCs are:

- *Noise and vibration reduction*. By designing phononic band gaps in the frequency range of interest, vibrations can be consistently reduced. This effect has been extensively exploited in MEMS resonators operation in vacuum, where the energy leakage from the anchors to the substrate (anchor losses) can be the loss mechanism limiting the quality factor. By designing anchors incorporating PNCs with a band gap containing the resonance frequency, anchor losses have been reduced [140, 141, 142, 143].

- *Heat conduction*. In many semiconductor materials, such as silicon, thermal energy is mainly transferred through the vibration of the adjacent atomic lattices, i. e. by phonons. Phononic crystal are thus an interesting approach for thermal conductivity manipulation of these structures [144, 145].

- *Acoustic waveguides*. Acoustic waveguides are structures capable of confining and guiding vibrations between two different point of the substate. Such structures are created by removing a line of scatterers (e. g. holes in a PNC realized trough perforations on the substrate) from a periodic structure [139, 146]. Waveguiding can be used to decouple the transmitting and receiving element in an acoustic imaging system, or to reduce the aperture size of each element of an acoustic imaging system, in order to obtain higher resolution images [135].

- *Resonant cavities*. If the defect introduced in the crystal is not a line, such as in the waveguide example above, but just a point (or a group of points surrounded by the crystal), the structure obtained is an acoustic resonant cavity [147, 148, 149]. Resonators based on these cavities are usually excited and detected through peripheral

piezoelectric couplers, with the advantage of having the low motional resistance typical of this transduction method, while non compromising the quality factor with the lossy piezoelectric and metal layers [135].

Another possible application of phononic crystals, which is the one motivating this chapter, is biosensing. As it will be clear after section 5.1, where a model for the calculation of the transmission spectra of electrostatically actuated MEMS phononic crystals will be presented, the position of the PBGs is inversely dependent from the mass density. Therefore, if the surface of the phononic crystal is fuctionalized, the mass addition due to analyte binding results in a downshift of the band gaps. The shift of a PBG can thus be used to estimate the added mass. There is no experimental proof of this sensing strategy in the MEMS world to date, if macroscopic structures are considered instead, several liquid sensors based on phononic crystals have been realized by Lucklum and his research group [150, 151, 152]. The main objective of the preliminary work described in this chapter is thus to prove the sensing capability of a phononic crystal structure realized with MEMS technology. This new sensing paradigm comes up beside the standard “resonant mode” sensing strategy and may offer advantages over the latter in some practical cases. However, a quantitative comparison, both theoretically and experimentally, has yet to be done. This chapter is organized as follows: in section 5.1 an acoustic transmission line model, capable of analytically predicting the transmission spectrum of a capacitively actuated MEMS phononic crystal, will be presented. In section 5.2 the dimensions of the designed PNCs will be listed and in 3.1.3 a comparison between the proposed model and FEM simulations will be made.

5.1 Acoustic transmission line model

In this section, an acoustic transmission line model, capable of describing the behavior of the specific phononic crystals designed in this work, will be developed. The discussion will start off with a short introduction on the analysis methods present in literature along with their advantages and drawbacks. Thereafter the specific geometry of the proposed phononic crystal will be introduced and a simple model suited for the description of this particular case will be developed.

During the last years, many methods have been used to study phononic crystals. Depending on the exploited technique, phononic crystals are characterized by means of their band structure, or by means of their transmission (or reflection) spectrum. The most used methods are the Plane Wave Expansion (PWE) [153], which allows the computation of the band structure, and Finite Difference Time Domain (FDTD) [154], which is instead used for the transmission spectrum computation. All these techniques have the advantage of being very general and powerful, allowing the description of any type of wave, without limits of polarization and propagation direction. On the other hand, they are cumbersome and often involve an heavy computational load [155, p.17-40]. These problems

arise from the complexity of the equation on motion in a solid continuum (somewhere called Lamé equation) that has to be solved. If compared to its counterparts of solid state physics and photonic crystals theory the phononic case is sharply more difficult: solid state physics deals with the Schrödinger equation which is scalar, photonic theory with Maxwell equations, which are vectorial but have the consistent advantage that electromagnetic field is transverse. Acoustic waves can be longitudinal and transverse and can only be decoupled in an homogeneous medium. In an inhomogeneous medium, such as a phononic crystal, these contributions cannot be separated, leading to a consistent increase in computational load [123]. The generality and thus the complexity of these models are unnecessary if a simple structure is studied. This is the case of the phononic crystal considered in this work: a thin rod where longitudinal waves are electrostatically excited and sensed through air gaps at the ends of the resonator. The spatial periodicity of the mechanical properties (mass density ρ and Young's modulus E), which are needed to realize a phononic crystal, are achieved through rectangular perforations on the rod. A schematic of the proposed structure is reported in figure 5.1. The structure outer dimension are the length L, the width w and the thickness h (not shown in the figure). The unit cell is described by the four parameters l_{sx}, t_{sx}, l_{sy}, t_{sy}. Others useful parameters to be defined are the number of holes N_x along the length L, and the number of holes N_y along the width w (which has been considered unitary for simplicity in figure 5.1). For the computations presented in the following of this section it is also useful to define the filling ratios along both dimensions. Exploiting the same definition (2.3) used for the holes matrix of the perforated beams and Lamé resonators, the filling ratio α_x, along the x direction, will be:

$$\alpha_x = \frac{t_{sx}}{l_{sx}} \tag{5.1}$$

Since the number of holes along y will be limited to few units, the modified relation that takes into account the finite N_y number is used for α_y:

$$\alpha_y = \frac{(N_y + 1)t_{sy}}{w} \tag{5.2}$$

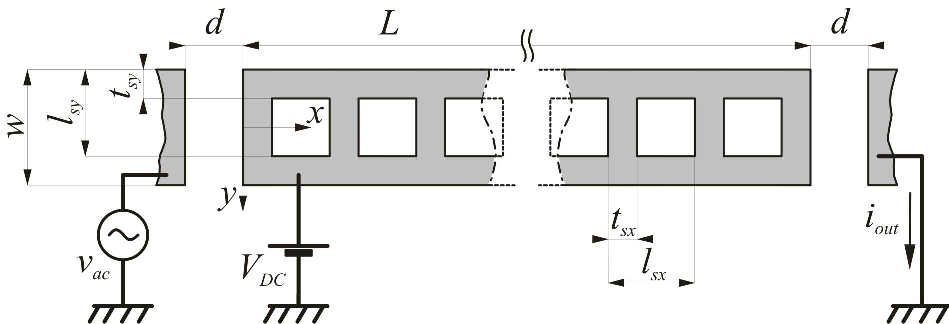

Figure 5.1: Schematic of the proposed MEMS phononic crystal with electrostic actuation and sensing.

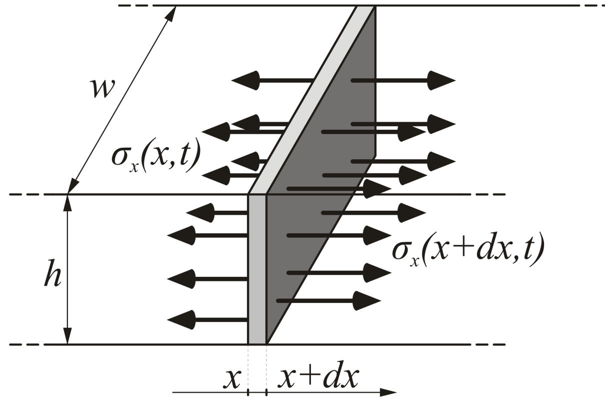

Figure 5.2: Rod section with the longitudinal stresses used to obtain the first equation in (5.3).

with this definition α_y is simply the ratio between the filled and perforated sections areas. Considering the proposed structure, if the first band gap has to be placed around few tens of megahertz, the maximum achievable dimensions in typical MEMS technologies limit also N_x to few units. However, as it will be clear once that the model will be fully developed, the crystal behavior in the x direction is exactly described for any value of N_x by considering each rod section separately. While the band structure is a lattice property, giving informations on the (ideal) infinite structure, the transmission spectrum can be computed for a (real) finite structure, thus taking into account finite crystal effects and boundary conditions. Because of the limited value of N_x, finite crystal effects cannot be neglected and the transmission spectrum is thus more suited for the description of the particular phononic crystal considered here. Computing the transmission of longitudinal waves through the finite structure of figure 5.1 simply means to give the output current i_{out} once than the geometry, the polarization voltage V_{DC} and the small signal actuation voltage v_{ac} are defined. Moreover, squeeze film damping that takes place in the actuation and detection gaps, which has been demonstrated as the limiting loss mechanism for the quality factor for both beams and Lamé resonators, as to be modeled through boundary conditions. Therefore another characteristic requested to the analytical model is a practical way to impose the boundary conditions. These results can be obtained by using a transmission matrix model, which is commonly used to describe transmission lines and Bragg structures in electrical engineering [156, p. 152,418]. In order to develop this model, the governing equations of motion for longitudinal waves along x axis of a vibrating thin rod with constant section are considered:

$$\frac{\partial \sigma_x(x,t)}{\partial x} = \rho \frac{\partial v_x(x,t)}{\partial t}$$

$$\frac{\partial v_x(x,t)}{\partial x} = \frac{1}{E}\frac{\partial \sigma_x(x,t)}{\partial t} \tag{5.3}$$

where σ_x is the stress along x and v_x the velocity of the section at x. The first equation can be derived by writing the Newton second law for the slice of infinitesimal length dx of figure 5.2. The second equation is the constitutive equation of the rod material assuming that the section dimensions w, h are much smaller than the rod length L. These equations are formally identical to the well-known telegraph equations for an electrical transmission line [156, p. 438]: the stress and the velocity are mapped to voltage and current along the line respectively, the mass density takes the place of the inductance per unit length of the line and the inverse of the Young's modulus takes the place of the capacity per unit length. Since the frequency behavior is of interest, equations (5.3) have to rewritten in phasor form:

$$\frac{d\Sigma_x(x)}{dx} = j\omega\rho V_x(x)$$

$$\frac{dV_x(x))}{dx} = \frac{j\omega}{E}\Sigma_x(x) \tag{5.4}$$

where $\Sigma_x(x)$ and $V_x(x)$ are the stress and velocity phasors respectively and ω is the pulsation. The solution of equations (5.4) expressed in the travelling-wave form is:

$$V_x(x) = V_x^+ e^{-ikx} + V_x^- e^{ikx}$$

$$\Sigma_x(x) = R_0\left(-V_x^+ e^{-ikx} + V_x^- e^{ikx}\right) \tag{5.5}$$

where the terms with negative exponentials represent progressive longitudinal waves, i. e. waves travelling in the positive direction of the x axis, while terms with positive exponential represent regressive longitudinal waves, i. e. waves travelling in the negative direction of the x axis. k is the wave number, defined as:

$$k = \omega\sqrt{\frac{\rho}{E}} \tag{5.6}$$

Going on with the already mentioned analogy with the electrical transmission lines, R_0 is the characteristic acoustic impedance of the equivalent acoustic transmission line. R_0 can be expressed as:

$$R_0 = \sqrt{\rho E} \tag{5.7}$$

The velocity and stress fields along the rod, expressed in (5.4), are defined by only the material properties ρ and E. Therefore, in order to describe the perforated rod behavior, models for these 2 quantities are needed in both the filled and perforated sections. Recalling the discussions expounded in sections 3.1 and 4.1, when dealing with perforated

beams and Lamé resonators, the *geometric model* will be used for this purpose. The rough results obtained by applying this model to both the previously studied resonator topologies are due to the holes geometry used. As it has been previously specified in the equivalent bending stiffness discussion of section 3.1, the approximation called *geometric model* is often used to study variable section beams, and good accuracy is obtained when the variation of cross-section is small in comparison with the lengths of the segments. In the phononic crystals geometries presented here, holes are rectangular instead than square. Moreover, all the realized geometries will have a cell length along x much more longer than the one along y ($l_{cx} \gg l_{cy}$). Therefore the above cited assumption is verified and the *geometric model* is expected to describe the structure with sufficient accuracy. The truthfulness of the last statement will be verified in section 5.3, where the model will be compared with FEM simulations. A straightforward application of the same considerations used for beams and Lamé resonators gives:

$$E_f = E \qquad \rho_f = \rho \qquad k_f = k \qquad R_{0f} = R_0$$

$$E_h = \alpha_y E \qquad \rho_h = \alpha_y \rho \qquad k_h = k \qquad R_{0h} = \alpha_y R_0 \tag{5.8}$$

where the quantities with the subscripts f and h are referred to the filled and perforated sections respectively. Using these equivalent parameters, the perforated sections can be modelled as filled sections made of an equivalent material with mass density ρ_h and Young's modulus E_h. Therefore the whole rod can be seen as an acoustic Bragg. From the acoustic transmission line point of view, the perforated rod can be modeled by a series of acoustic transmission lines with different characteristic impedance: R_{0f} in the sections corresponding to the filled parts of the rod and R_{0h} in the ones corresponding to the perforated rod parts. These analogies are summarized in figure 5.3. As it is common for the propagation of current and voltage waves along electric transmission lines, the propagation of velocity and stress waves along the acoustic transmission line can be described by using the transmission line approach. Transmission matrices of such a system can be divied into 2 categories: *propagation matrices* and *matching matrices*. Propagation matrices describe the wave propagation along a constant section part of the rod. By using the progressive and regressive velocity wave components as the unknown variables, the *propagation matrix* P_f of a filled section is:

$$\begin{pmatrix} V_r^+ \\ V_r^- \end{pmatrix} = \overbrace{\begin{pmatrix} e^{-k\alpha_x l_{sx}} & 0 \\ 0 & e^{k\alpha_x l_{sx}} \end{pmatrix}}^{P_f} \begin{pmatrix} V_l^+ \\ V_l^- \end{pmatrix} \tag{5.9}$$

where the subscripts r an l identify the waves at the right and left side of the filled segment respectively. With a straightforward analogy the propagation matrix P_h of the filled segments is:

$$P_h = \begin{pmatrix} e^{-k(1-\alpha_x)l_{sx}} & 0 \\ 0 & e^{k(1-\alpha_x)l_{sx}} \end{pmatrix} \tag{5.10}$$

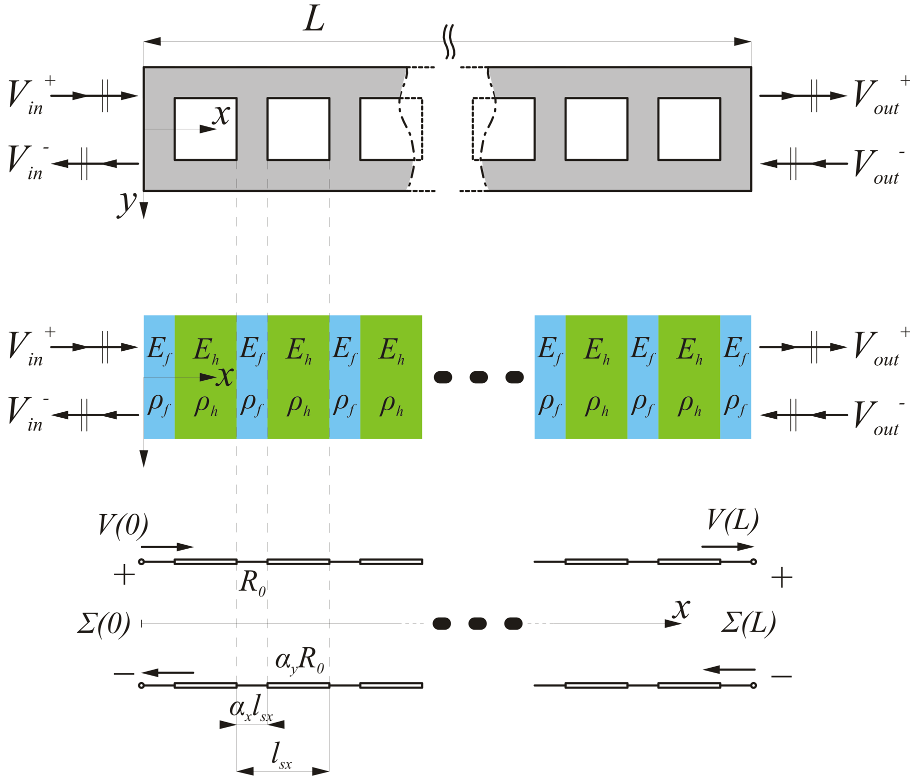

Figure 5.3: Schematic representations of the equivalent models for the perforated rod (top): acoustic Bragg (center) and the equivalent acoustic transmission line (bottom). The progressive and regressive waves at the input and output of the system are shown in the top and center schematics, while the standing waves are shown in the transmission line instead.

The *matching matrices* instead model the propagation at the interface between segments with different sections. Considering an interface (place at $x = 0$ for clarity) where filled sections are on the left and the perforated ones on the right, the continuity of velocity and stress can be written by exploiting the expressions (5.4):

$$V_l^+ + V_l^- = V_r^+ + V_r^-$$

$$R_0 \left(-V_l^+ + V_l^- \right) = \alpha_y R_0 \left(-V_r^+ + V_r^- \right) \tag{5.11}$$

By solving this system for the right side waves, and writing the found relationships in matrix form, the expression of the *matching matrix* M_{fh}, between the filled and perforated sections is found:

$$\begin{pmatrix} V_r^+ \\ V_r^- \end{pmatrix} = \overbrace{\begin{pmatrix} \frac{1+\alpha_y}{2\alpha_y} & \frac{\alpha_y-1}{2\alpha_y} \\ \frac{\alpha_y-1}{2\alpha_y} & \frac{1+\alpha_y}{2\alpha_y} \end{pmatrix}}^{M_{fh}} \begin{pmatrix} V_l^+ \\ V_l^- \end{pmatrix} \tag{5.12}$$

The last matrix, the matching matrix M_{hf} between perforated (left side) and filled (right side) sections, can be found by simply inverting M_{fh}:

$$M_{hf} = {M_{fh}}^{-1} = \begin{pmatrix} \frac{1+\alpha_y}{2} & \frac{1-\alpha_y}{2} \\ \frac{1-\alpha_y}{2} & \frac{1+\alpha_y}{2} \end{pmatrix} \tag{5.13}$$

Using the four matrices defined in equations (5.9), (5.10), (5.12), (5.13), the progressive and regressive output waves at the rod end ($x = L$) can be related to the progressive and regressive input waves at $x = 0$:

$$\begin{pmatrix} V_{out}^+ \\ V_{out}^- \end{pmatrix} = \overbrace{P_f \left(M_{hf} P_h M_{fh} P_f\right)^{Nx}}^{T_{ROD}} \begin{pmatrix} V_{in}^+ \\ V_{in}^- \end{pmatrix} \tag{5.14}$$

where the rod transmission matrix T_{ROD} has been defined. It is useful to remark that a final multiplication for P_f is needed, since the rod ends with a filled section. The system is fully determined once that the boundary conditions are imposed. On the input electrode the stress forced by the electrostatic actuation, as well as the squeeze film damping effect have to be taken in consideration. On the output electrode instead, only the squeeze contribution is present. The coupling coefficient that gives the linearized relationship between the forced stress and the small signal voltage V_{ac}, can be easily derived from the formula 2.13 for the lumped parameters electromechanical coupling coefficient, considering that the stress (instead of the force) is the variable of interest. The equations for the 2 boundaries are:

$$\frac{\epsilon_0 V_{DC}}{d^2} V_{ac} + \frac{c_{sqz}}{wh} V_x(0) = \Sigma_x(0)$$

$$\frac{c_{sqz}}{wh} V_x(L) = \Sigma_x(L) \tag{5.15}$$

where c_{sqz} is the squeeze film damping coefficient of equation (2.79). Since it is negligible, the spring softening effect has not been included in equations (5.15). These boundary conditions can be represented in the acoustic transmission line model as show in figure 5.4. With the four equations (5.14) and (5.15) the velocity (and the stress) profile along the rod can be determined. Finally, the rod transconductance Y_{ROD} can be written as:

$$Y_{ROD}(j\omega) = \frac{I_{out}(j\omega)}{V_{ac}(j\omega)} = \frac{\epsilon_0 V_{DC}}{d^2} V_x(L) \tag{5.16}$$

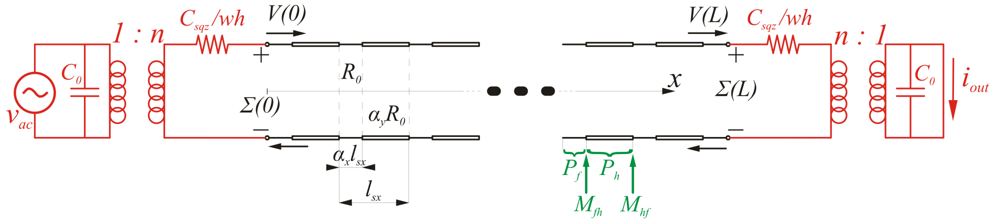

Figure 5.4: Acoustic transmission line with the boundary conditions of (5.15) reported in red. $n = \epsilon_0 V_{DC}/d^2$ is the electromechanical coupling coefficient related to the stress and $C_0 = \epsilon_0 wh/d$ is the static capacity of the actuation and detection gaps.

Losses along the crystal

The developed model allows an easy description of the proposed phononic crystal through its transconductance Y_{ROD}. A straightforward modelling of the electrostatic actuation an sensing, as well as the squeeze film damping, has been shown. In order to have a complete description of the viscous losses taking place on the phononic crystal, slide film damping have to be considered too. In the case of a full rod, this effect can be considered by taking into account the viscous damping force acting on the slice of figure 5.2:

$$\frac{\partial \sigma_x(x,t)}{\partial x} - \frac{c_{u-1s} + c_{o-1s}}{h} v_x(x,t) = \rho \frac{\partial v_x(x,t)}{\partial t} \tag{5.17}$$

where c_{u-1s} and c_{o-1s} are the slide film damping per unit surface over and under the structure (see equations 2.74 and 2.78). Equation (5.17) can be rewritten in the frequency domain as:

$$\frac{d\Sigma_x(x)}{dx} = j\omega \underbrace{\left(\rho - j\frac{c_{u-1s} + c_{o-1s}}{\omega h}\right)}_{\rho_D} V_x(x) \tag{5.18}$$

The obtained equation is formally identical to the first equation in 5.3 if the “damped density” ρ_D is substituted to the material density ρ. Therefore the slide can be taken into account by using this equivalent complex density. As the slide area in the perforated section is proportional to α_y, the models in the filled and perforated section will be again:

$$\rho_{f-D} = \rho_D \qquad\qquad \rho_{h-D} = \alpha_y \rho_D \tag{5.19}$$

5.2 Designed structures

In this section the dimensions of the designed phononic crystal rods will be summarized. The technological processes used are the same ones exploited in the beam and Lamé resonators. Details on the processes can be found in section 3.2, this section will be limited the list of the structures layout dimensions.

TRONICS

name	l_{sx} [μm]	N_x	α_x	l_{sy} [μm]	N_y	α_y
P1	170	6	0.2	26	8	0.3
P2	240	4	0.14	35	6	0.15

Table 5.1: Phononic crystals fabricated with the TRONICS process.

SiGe

name	l_{sx} [μm]	N_x	α_x	l_{sy} [μm]	N_y	α_y
P1	75	5	0.3	11.25	8	0.3
P2	75	5	0.3	15	6	0.2
P3	75	5	0.3	15.5	6	0.15
P4	75	5	0.6	11.25	8	0.3
P5	100	4	0.3	15	6	0.3
P6	100	4	0.3	18	5	0.2
P7	100	4	0.3	23	4	0.15
P8	100	4	0.5	11.5	8	0.3
P9	100	4	0.6	15	6	0.3
P10	100	4	0.6	23	4	0.15
P11	130	3	0.3	16	6	0.2
P12	130	3	0.3	13	7	0.3
P13	130	3	0.6	16	6	0.2

Table 5.2: Phononic crystals fabricated with the SiGe process.

5.3 FEM validation

In this section, in order to validate the acoustic transmission line model presented in section 5.1, a comparison with harmonic FEM simulations will be carried out. The considered geometry is the one named P1 in table 5.1, the material properties and gap dimensions are thus the ones of the TRONICS process, reported in table 3.2. The bias voltage is assumed to be $V_{DC} = 40\,\mathrm{V}$ and the simulation frequency is swept around the first band gap with steps $\Delta f = 40\,\mathrm{kHz}$. Both model and simulation show a phononinc band gap in the frequency range $\approx 18-30\,\mathrm{MHz}$, as well as several resonance peaks before and after this gap. The presence of resonance peaks in the frequency response is not surprising since the structure can be seen as a resonator with a phononic crystal embedded on it. Apart from the various spurious peaks present in the simulated response, there is a very good accordance between model and simulation on the gap and resonance peaks positions. For a better understanding of the phononic crystal behavior, the FEM plots of the amplitude of the x displacement U_x, at three meaningful frequencies, named f_a, f_b

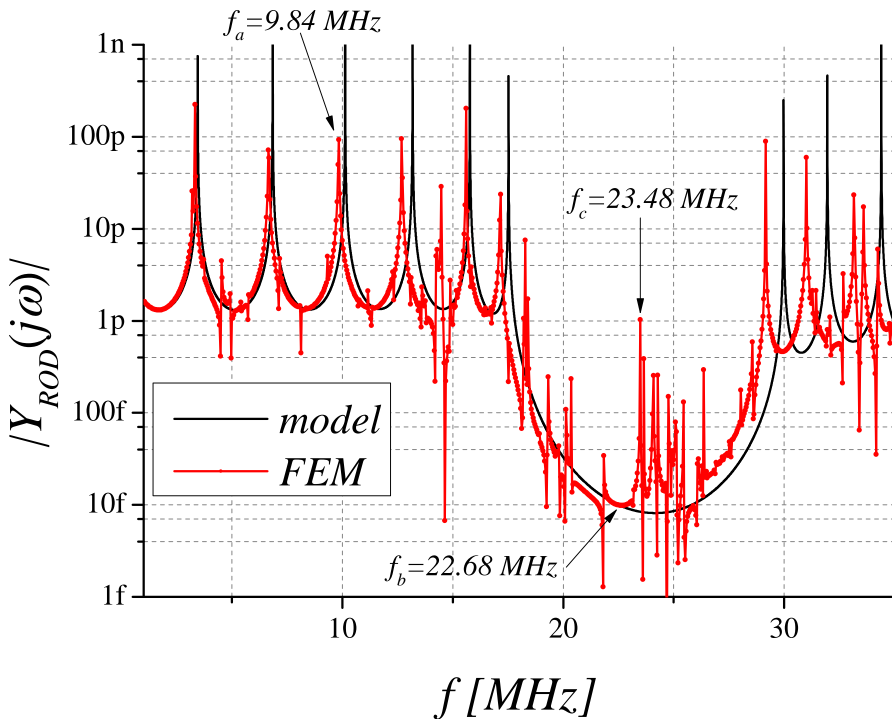

Figure 5.5: Comparison between the phononic crystal transconductance, computed with the acoustic transmission line model proposed in section 5.1, and obtained with harmonic FEM simulations. The technological process considered is TRONICS (see table 3.2) and the device dimensions are the ones of P1 in table 5.1. The bias voltage is $V_{DC} = 40\,\mathrm{V}$. The highlighted frequencies f_a, f_b and f_c will be used in the following.

and f_c in the plot of figure 5.5, will be shown in the following. f_a is the frequency where the simulation exhibits the maximum of the third resonance peak, f_b is a frequency on the bottom of the phononic band gap, and f_c is a frequency where the simulation shown a spurious (i. e. not predicted by the model) peak. The amplitude of U_x, obtained from the FEM simulation at the frequency $f_a = 9.84\,\mathrm{MHz}$, is shown in figure 5.6 and displays the typical behavior of the third resonance mode of a free-free rod. Figure 5.7 shows instead the displacement amplitude at a frequency $f_b = 22.68\,\mathrm{MHz}$ in the middle of the phononic band gap. As it can be seen, waves are present only at the input electrode where are excited by the electrostatic actuation, but are not propagating along the rod. Finally, figure 5.8 shows the displacement amplitude at $f_c = 23.48\,\mathrm{MHz}$. Even if this frequency belongs to the phononic band gap, the simulated frequency response shows a spurious peak not predicted by the model. As it can be seen by figure 5.5, spurious peaks are present over the whole simulate frequency range and thus require further investigations. By looking at the displacement plot it is clear that this unwanted effect is due to the folded anchors needed to fix the structure to the substrate. When the excitation frequency is near to one of the anchors resonance frequencies, these components are subject to high

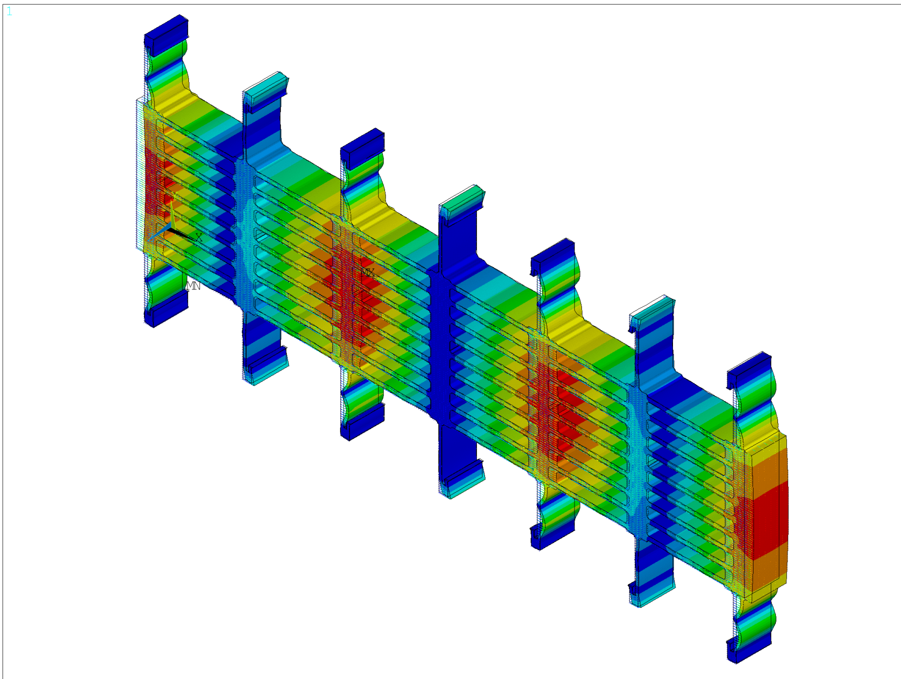

Figure 5.6: Amplitude of the x axis displacement extracted from the FEM simulation at the frequency $f_a = 9.84\,\mathrm{MHz}$ shown in figure 5.5. At this frequency the simulated response shows the maximum of the third resonance peak. As expected, the deformed shape shown corresponds to the third resonance mode of a free-free rod.

vibration amplitudes, which unavoidably couple with the output electrode, generating the spurious peaks in the frequency response. This effect, though real, is exalted by the low damping imposed on the anchors in the presented simulations, where only the slide effect on the upper and lower surfaces has been modeled. For example, squeeze film damping exist in the volume between the two beams composing the folded anchor, however, the high resonance modes excited and the complexity of the geometry, make the value of this damping very difficult to be estimated. Therefore an accurate modeling of the damping on the anchors has not been performed. Further considerations on anchors design strategies, aimed at limiting this effect, will be taken into consideration if experimental data will evidence such important presence of spurious peaks. However, the above considerations on the damping of the anchors suggest that the quantity and magnitude of the spurious peaks observed in simulated transconductance of figure 5.5 are the worst case scenario.

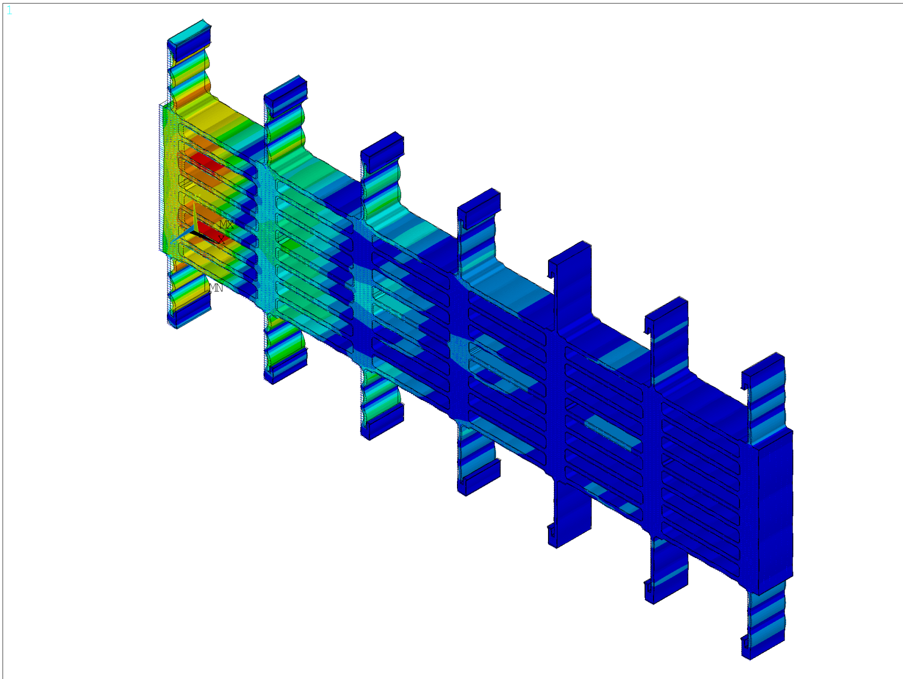

Figure 5.7: Amplitude of the x axis displacement extracted from the FEM simulation at the frequency $f_b = 22.68\,\mathrm{MHz}$ shown in figure 5.5. This frequency is in the middle of the phononic band gap. As expected waves are not propagating through the crystal.

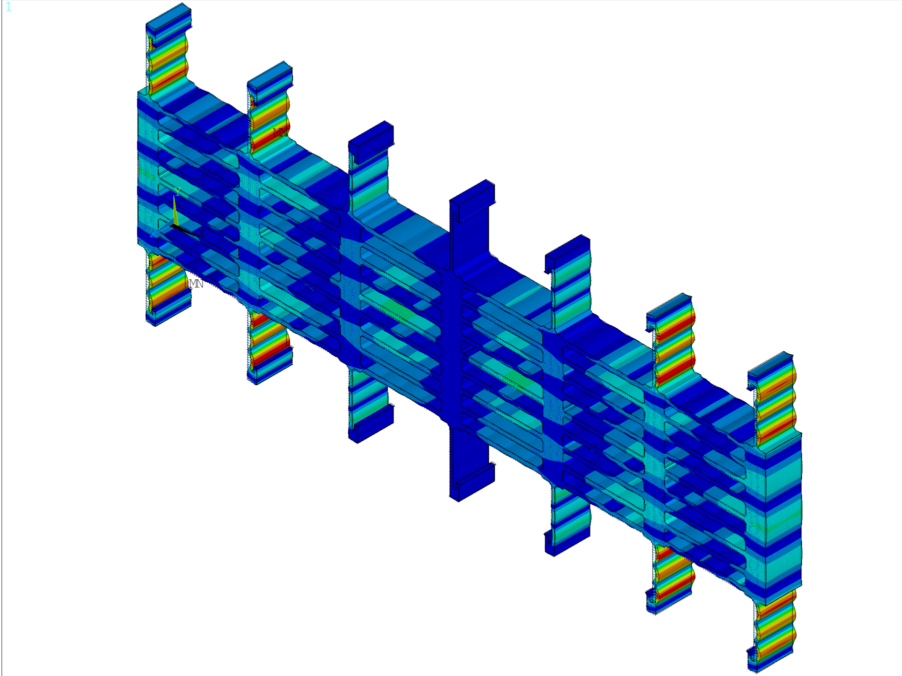

Figure 5.8: Amplitude of the x axis displacement extracted from the FEM simulation at the frequency $f_c = 23.48\,\mathrm{MHz}$ shown in figure 5.5. This frequency belongs to the phononic band gap but a spurious peak is present in the simulated response. Vibrations are localized in the anchors suggesting that these structures are in resonance. The unavoidable coupling of these vibrations with the output electrode generated the spurious peak in the frequency response.

6

Conclusions

In this work, MEMS resonant sensors fabricated with commercial MEMS technologies and exploiting the electrostatic transduction technique were presented. Such sensors are resonance structures whose resonance frequencies withstand a downshift upon immobilization of the entity to be sensed on their surface. While the commonly adopted approach to design high sensitive resonant sensors is to realize small and thin structures, the original approach proposed in this work is based on drawing a regular pattern of holes over the resonator. The holes are expected to provide an higher surface for analyte binding, thus increasing the quantity of captured entities. This concept has been proven by an accurate analysis of the resonators sensitivities in presence of perforations, and by comparing it with the standard "holes-free" approach. Established models were also introduced in order to predict the other resonance sensors performances. This analysis highlighted some trade-offs on the proposed approach, since the holes have a detrimental effect over the resonator quality factor and power handling. Compared with the standard approach used to obtain high sensitivity devices, the proposed design technique does not require any ad-hoc technological step and is thus compatible with commercially available MEMS technologies. Resonators designed using TRONICS SOI and IMEC Silicon-Germanium processes, and based on clamped-clamped beam and Lamé resonant modes, were presented. For both resonant modes, analytical models for the resonance frequency in presence of perforations were developed and compared with FEM simulations, showing good accordance. These models were thus used for the estimation of the resonant sensor performances. Lamé resonators exhibited superior performances due to their higher quality factors an a better resonance frequency stability with respect to the perforation size. For the case of clamped-clamped beams realized with TRONICS technology, a preliminary characterization, showing excellent accordance on the resonance frequency value with the proposed model and FEM simulations, were shown too. Finally, a new type of resonant sensor, based on a phononic crystal, was presented. As a first step in the development on this type of sensor, an acoustic transmission line model, suitable for the analysis and synthesis of such structures, was developed.

The research work described in this thesis will proceed with a full characterization of all the presented structures, aimed at an extensive validation of the proposed analytical models for the resonance frequencies, as well as at the study of the effect of the holes on the quality factor. Moreover, functionalization of the sensors surfaces and exposition to the analyte are needed in order to validate the better sensitivity and limit of detection expected from the holes. Regarding phononic crystals, experimental verification of the proposed transmission line model has to be considered the first objective to be achieved. Thereafter, experimental evidence of the sensing capability of such structures, as well as an analysis of this strategy, aimed at highlighting advantages and drawbacks with respect to the traditional resonance frequency strategy, are needed.

References

1. Kurt E Petersen. Silicon as a mechanical material. *Proceedings of the IEEE*, 70(5):420–457, 1982.
2. Rashid Bashir. Biomems: state-of-the-art in detection, opportunities and prospects. *Advanced drug delivery reviews*, 56(11):1565–1586, 2004.
3. AC Richards Grayson, Rebecca S Shawgo, Audrey M Johnson, Nolan T Flynn, Yawen Li, Michael J Cima, and Robert Langer. A biomems review: Mems technology for physiologically integrated devices. *Proceedings of the IEEE*, 92(1):6–21, 2004.
4. Younan Xia and George M Whitesides. Soft lithography. *Annual review of materials science*, 28(1):153–184, 1998.
5. Joel Voldman. Biomems: building with cells. *Nature materials*, 2(7):433–434, 2003.
6. Eric Nuxoll. Biomems in drug delivery. *Advanced drug delivery reviews*, 65(11):1611–1625, 2013.
7. S Sershen and J West. Implantable, polymeric systems for modulated drug delivery. *Advanced Drug Delivery Reviews*, 54(9):1225–1235, 2002.
8. Sangeeta N Bhatia and Christopher S Chen. Tissue engineering at the micro-scale. *Biomedical Microdevices*, 2(2):131–144, 1999.
9. Harri Härmä, Tero Soukka, and Timo Lövgren. Europium nanoparticles and time-resolved fluorescence for ultrasensitive detection of prostate-specific antigen. *Clinical chemistry*, 47(3):561–568, 2001.
10. Joseph L DeRisi, Vishwanath R Iyer, and Patrick O Brown. Exploring the metabolic and genetic control of gene expression on a genomic scale. *Science*, 278(5338):680–686, 1997.
11. Yung-Shin Sun, James P Landry, YY Fei, XD Zhu, JT Luo, XB Wang, and KS Lam. Effect of fluorescently labeling protein probes on kinetics of protein- ligand reactions. *Langmuir*, 24(23):13399–13405, 2008.
12. Philip S Waggoner and Harold G Craighead. Micro-and nanomechanical sensors for environmental, chemical, and biological detection. *Lab on a Chip*, 7(10):1238–1255, 2007.
13. Patrick Boisseau, Philippe Houdy, and Marcel Lahmani. *Nanoscience: Nanobiotechnology and nanobiology*. Springer, 2010.
14. J Homola, Sinclair S Yee, and Günter Gauglitz. Surface plasmon resonance sensors: review. *Sensors and Actuators B: Chemical*, 54(1):3–15, 1999.
15. XD Hoa, AG Kirk, and M Tabrizian. Towards integrated and sensitive surface plasmon resonance biosensors: a review of recent progress. *Biosensors and Bioelectronics*, 23(2):151–160, 2007.
16. Frank B Myers and Luke P Lee. Innovations in optical microfluidic technologies for point-of-care diagnostics. *Lab on a Chip*, 8(12):2015–2031, 2008.

17. C Weisbuch, M Rattier, L Martinelli, H Choumane, J-C Avarre, Y Marcy, G Cerovic, M-L Miramon, G-O Reymond, and H Benisty. Towards portable, real-time, integrated fluorescence microarray diagnostics tools. *IRBM*, 28(5):216–223, 2007.
18. J Alex Chediak, Zhongsheng Luo, Jeonggi Seo, Nathan Cheung, Luke P Lee, and Timothy D Sands. Heterogeneous integration of cds filters with gan leds for fluorescence detection microsystems. *Sensors and Actuators B: Physical*, 111(1):1–7, 2004.
19. Dmitri V Vezenov, Brian T Mayers, Richard S Conroy, George M Whitesides, Preston T Snee, Yinthai Chan, Daniel G Nocera, and Moungi G Bawendi. A low-threshold, high-efficiency microfluidic waveguide laser. *Journal of the American Chemical Society*, 127(25):8952–8953, 2005.
20. T Vo-Dinh, JP Alarie, N Isola, D Landis, Al L Wintenberg, and MN Ericson. Dna biochip using a phototransistor integrated circuit. *Analytical Chemistry*, 71(2):358–363, 1999.
21. Andrea Pais, Ansuman Banerjee, David Klotzkin, and Ian Papautsky. High-sensitivity, disposable lab-on-a-chip with thin-film organic electronics for fluorescence detection. *Lab on a Chip*, 8(5):794–800, 2008.
22. TM Chinowsky, JG Quinn, DU Bartholomew, R Kaiser, and JL Elkind. Performance of the spreeta 2000 integrated surface plasmon resonance affinity sensor. *Sensors and Actuators B: Chemical*, 91(1):266–274, 2003.
23. S Poyard, N Jaffrezic-Renault, C Martelet, S Cosnier, and P Labbe. Optimization of an inorganic/bio-organic matrix for the development of new glucose biosensor membranes. *Analytica chimica acta*, 364(1):165–172, 1998.
24. A Bratov, N Abramova, and A Ipatov. Recent trends in potentiometric sensor arrays-a review. *Analytica chimica acta*, 678(2):149–159, 2010.
25. M Waleed Shinwari, M Jamal Deen, and Dolf Landheer. Study of the electrolyte-insulator-semiconductor field-effect transistor (eisfet) with applications in biosensor design. *Microelectronics Reliability*, 47(12):2025–2057, 2007.
26. So-Jung Park, T Andrew Taton, and Chad A Mirkin. Array-based electrical detection of dna with nanoparticle probes. *Science*, 295(5559):1503–1506, 2002.
27. R Bhatia, JW Dilleen, AL Atkinson, and DM Rawson. Combined physico-chemical and biological sensing in environmental monitoring. *Biosensors and Bioelectronics*, 18(5):667–674, 2003.
28. Imants R Lauks. Microfabricated biosensors and microanalytical systems for blood analysis. *Accounts of Chemical Research*, 31(5):317–324, 1998.
29. Vladimir Gubala, Leanne F Harris, Antonio J Ricco, Ming X Tan, and David E Williams. Point of care diagnostics: status and future. *Analytical chemistry*, 84(2):487–515, 2011.
30. Yi Cui, Qingqiao Wei, Hongkun Park, and Charles M Lieber. Nanowire nanosensors for highly sensitive and selective detection of biological and chemical species. *Science*, 293(5533):1289–1292, 2001.
31. Koen Besteman, Jeong-O Lee, Frank GM Wiertz, Hendrik A Heering, and Cees Dekker. Enzyme-coated carbon nanotubes as single-molecule biosensors. *Nano letters*, 3(6):727–730, 2003.
32. Abraham J Qavi, Adam L Washburn, Ji-Yeon Byeon, and Ryan C Bailey. Label-free technologies for quantitative multiparameter biological analysis. *Analytical and bioanalytical chemistry*, 394(1):121–135, 2009.
33. Lauge Gammelgaard, Peter Andreas Rasmussen, Montserrat Calleja, P Vettiger, and Anja Boisen. Microfabricated photoplastic cantilever with integrated photoplastic/carbon based piezoresistive strain sensor. *Applied Physics Letters*, 88(11):113508–113508, 2006.
34. Rupa Mukhopadhyay, Martin Lorentzen, Jørgen Kjems, and Flemming Besenbacher. Nanomechanical sensing of dna sequences using piezoresistive cantilevers. *Langmuir*, 21(18):8400–8408, 2005.
35. Nickolay V Lavrik, Michael J Sepaniak, and Panos G Datskos. Cantilever transducers as a platform for chemical and biological sensors. *Review of scientific instruments*, 75(7):2229–2253, 2004.

36. Anja Boisen, Søren Dohn, Stephan Sylvest Keller, Silvan Schmid, and Maria Tenje. Cantilever-like micromechanical sensors. *Reports on Progress in Physics*, 74(3):036101, 2011.
37. Joseph Wafula Ndieyira, Moyu Watari, Alejandra Donoso Barrera, Dejian Zhou, Manuel Vögtli, Matthew Batchelor, Matthew A Cooper, Torsten Strunz, Mike A Horton, Chris Abell, et al. Nanomechanical detection of antibiotic–mucopeptide binding in a model for superbug drug resistance. *Nature nanotechnology*, 3(11):691–696, 2008.
38. YT Yang, Carlo Callegari, XL Feng, KL Ekinci, and ML Roukes. Zeptogram-scale nanomechanical mass sensing. *Nano letters*, 6(4):583–586, 2006.
39. Kilho Eom, Harold S Park, Dae Sung Yoon, and Taeyun Kwon. Nanomechanical resonators and their applications in biological/chemical detection: nanomechanics principles. *Physics Reports*, 503(4):115–163, 2011.
40. Najib Kacem, Sebastien Hentz, D Pinto, B Reig, and V Nguyen. Nonlinear dynamics of nanomechanical beam resonators: improving the performance of nems-based sensors. *Nanotechnology*, 20(27):275501, 2009.
41. Kevin Y Yasumura, Timothy D Stowe, Eugene M Chow, Timothy Pfafman, Thomas W Kenny, Barry C Stipe, and Daniel Rugar. Quality factors in micron-and submicron-thick cantilevers. *Microelectromechanical Systems, Journal of*, 9(1):117–125, 2000.
42. Philip S Waggoner and Harold G Craighead. The relationship between material properties, device design, and the sensitivity of resonant mechanical sensors. *Journal of Applied Physics*, 105(5):054306–054306, 2009.
43. Daniel Ramos, Javier Tamayo, Johann Mertens, Montserrat Calleja, and A Zaballos. Origin of the response of nanomechanical resonators to bacteria adsorption. *Journal of Applied Physics*, 100(10):106105–106105, 2006.
44. Philip S Waggoner, Madhukar Varshney, and Harold G Craighead. Detection of prostate specific antigen with nanomechanical resonators. *Lab on a Chip*, 9(21):3095–3099, 2009.
45. Dirk Lange, Christoph Hagleitner, Andreas Hierlemann, Oliver Brand, and Henry Baltes. Complementary metal oxide semiconductor cantilever arrays on a single chip: mass-sensitive detection of volatile organic compounds. *Analytical Chemistry*, 74(13):3084–3095, 2002.
46. Jeong Hoon Lee, Kyo Seon Hwang, Jaebum Park, Ki Hyun Yoon, Dae Sung Yoon, and Tae Song Kim. Immunoassay of prostate-specific antigen (psa) using resonant frequency shift of piezoelectric nanomechanical microcantilever. *Biosensors and Bioelectronics*, 20(10):2157–2162, 2005.
47. J Fritz, MK Baller, HP Lang, H Rothuizen, P Vettiger, E Meyer, H-J Güntherodt, Ch Gerber, and JK Gimzewski. Translating biomolecular recognition into nanomechanics. *Science*, 288(5464):316–318, 2000.
48. J Verd, A Uranga, G Abadal, JL Teva, F Torres, J Lopez, F Perez-Murano, J Esteve, and N Barniol. Monolithic cmos mems oscillator circuit for sensing in the attogram range. *IEEE electron device letters*, 29(2):146–148, 2008.
49. Wan-Thai Hsu, John R Clark, and Clark T-C Nguyen. Q-optimized lateral free-free beam micromechanical resonators. In *11th International Conference on Solid-State Sensors and Actuators, Munich, Germany*, pages 1110–1113, 2001.
50. Jan Harry Hales, Jordi Teva, Anja Boisen, and Zachary James Davis. Longitudinal bulk a coustic mass sensor. In *Solid-State Sensors, Actuators and Microsystems Conference, 2009. TRANSDUCERS 2009. International*, pages 311–314. IEEE, 2009.
51. M Ziaei-Moayyed, D Elata, EP Quévy, and RT Howe. Differential internal dielectric transduction of a lamé-mode resonator. *Journal of Micromechanics and Microengineering*, 20(11):115036, 2010.
52. Ville Kaajakari, Tomi Mattila, Aarne Oja, Jyrki Kiihamaki, Hannu Kattelus, Mika Koskenvuori, Pekka Rantakari, Ilkka Tittonen, and Heikki Seppa. Square-extensional mode single-crystal silicon micromechanical rf-resonator. In *TRANSDUCERS, Solid-State Sensors, Actuators and Microsystems, 12th International Conference on, 2003*, volume 2, pages 951–954. IEEE, 2003.

53. John R Clark, Wan-Thai Hsu, Mohamed A Abdelmoneum, and CT-C Nguyen. High-q uhf micromechanical radial-contour mode disk resonators. *Microelectromechanical Systems, Journal of*, 14(6):1298–1310, 2005.
54. Yu-Wei Lin, Sheng-Shian Li, Yuan Xie, Zeying Ren, and CT-C Nguyen. Vibrating micromechanical resonators with solid dielectric capacitive transducer gaps. In *Frequency Control Symposium and Exposition, 2005. Proceedings of the 2005 IEEE International*, pages 128–134. IEEE, 2005.
55. Gavin K Ho, Krishnakumar Sundaresan, Siavash Pourkamali, and Farrokh Ayazi. Micromechanical ibars: Tunable high-resonators for temperature-compensated reference oscillators. *Microelectromechanical Systems, Journal of*, 19(3):503–515, 2010.
56. Siavash Pourkamali, Gavin K Ho, and Farrokh Ayazi. Low-impedance vhf and uhf capacitive silicon bulk acoustic wave resonators-part i: Concept and fabrication. *Electron Devices, IEEE Transactions on*, 54(8):2017–2023, 2007.
57. James M Bustillo, Roger T Howe, and Richard S Muller. Surface micromachining for microelectromechanical systems. *Proceedings of the IEEE*, 86(8):1552–1574, 1998.
58. Niels Tas, Tonny Sonnenberg, Henri Jansen, Rob Legtenberg, and Miko Elwenspoek. Stiction in surface micromachining. *Journal of Micromechanics and Microengineering*, 6(4):385, 1996.
59. CH Mastrangelo and CH Hsu. Mechanical stability and adhesion of microstructures under capillary forces. i. basic theory. *Microelectromechanical Systems, Journal of*, 2(1):33–43, 1993.
60. CH Mastrangelo and CH Hsu. Mechanical stability and adhesion of microstructures under capillary forces. ii. experiments. *Microelectromechanical Systems, Journal of*, 2(1):44–55, 1993.
61. Vincenzo Russino. *CMOS-compatible MEMS processes and their application to the development of biosensors*. PhD thesis, University of Pisa, 2012.
62. Silvia Lenci. *Enabling technologies for CMOS-compatible MEMS biosensors*. PhD thesis, University of Pisa, 2010.
63. Harrie AC Tilmans. Equivalent circuit representation of electromechanical transducers: I. lumped-parameter systems. *Journal of Micromechanics and Microengineering*, 6(1):157, 1996.
64. Harrie AC Tilmans. Equivalent circuit representation of electromechanical transducers: Ii. distributed-parameter systems. *Journal of Micromechanics and Microengineering*, 7(4):285, 1997.
65. J EY Lee, Yong Zhu, and AA Seshia. A bulk acoustic mode single-crystal silicon microresonator with a high-quality factor. *Journal of micromechanics and microengineering*, 18(6):064001, 2008.
66. P Bruschi, A Nannini, and F Pieri. Electrical measurements of the quality factor of microresonators and its dependence on the pressure. *Sensors and Actuators A: Physical*, 114(1):21–29, 2004.
67. Sunil A Bhave, Di Gao, Roya Maboudian, and Roger T Howe. Fully-differential poly-sic lame mode resonator and checkerboard filter. In *Micro Electro Mechanical Systems, 2005. MEMS 2005. 18th IEEE International Conference on*, pages 223–226. IEEE, 2005.
68. Yuanjie Xu and Joshua E-Y Lee. Single-device and on-chip feedthrough cancellation for hybrid mems resonators. *Industrial Electronics, IEEE Transactions on*, 59(12):4930–4937, 2012.
69. Julien Arcamone, Eric Colinet, Antoine Niel, and Eric Ollier. Efficient capacitive transduction of high-frequency micromechanical resonators by intrinsic cancellation of parasitic feedthrough capacitances. *Applied Physics Letters*, 97(4):043505, 2010.
70. Seon M Han, Haym Benaroya, and Timothy Wei. Dynamics of transversely vibrating beams using four engineering theories. *Journal of Sound and Vibration*, 225(5):935–988, 1999.

71. JE-Y Lee, B Bahreyni, Yong Zhu, and AA Seshia. Ultrasensitive mass balance based on a bulk acoustic mode single-crystal silicon resonator. *Applied Physics Letters*, 91(23):234103–234103, 2007.
72. Ville Kaajakari, Tomi Mattila, Aarne Oja, Jyrki Kiihamaki, and Heikki Seppa. Square-extensional mode single-crystal silicon micromechanical resonator for low-phase-noise oscillator applications. *Electron Device Letters, IEEE*, 25(4):173–175, 2004.
73. KL Ekinci, YT Yang, and ML Roukes. Ultimate limits to inertial mass sensing based upon nanoelectromechanical systems. *Journal of applied physics*, 95(5):2682–2689, 2004.
74. Angel TH Lin, Jize Yan, and Ashwin A Seshia. 2.2 mhz piezoresistive mems oscillator operating in air. *Procedia Engineering*, 5:1498–1501, 2010.
75. T Mattila, J Kiihamäki, T Lamminmäki, O Jaakkola, P Rantakari, A Oja, H Seppä, H Kattelus, and I Tittonen. A 12 mhz micromechanical bulk acoustic mode oscillator. *Sensors and Actuators A: Physical*, 101(1):1–9, 2002.
76. Krishnakumar Sundaresan, Gavin K Ho, Siavash Pourkamali, and Farrokh Ayazi. Electronically temperature compensated silicon bulk acoustic resonator reference oscillators. *Solid-State Circuits, IEEE Journal of*, 42(6):1425–1434, 2007.
77. Emad Eldin Hegazi, Jacob Rael, and Asad Abidi. *The designer's guide to high-purity oscillators*. Springer, 2006.
78. Thomas H Lee and Ali Hajimiri. Oscillator phase noise: a tutorial. *Solid-State Circuits, IEEE Journal of*, 35(3):326–336, 2000.
79. Alper Demir, Amit Mehrotra, and Jaijeet Roychowdhury. Phase noise in oscillators: a unifying theory and numerical methods for characterization. *Circuits and Systems I: Fundamental Theory and Applications, IEEE Transactions on*, 47(5):655–674, 2000.
80. WP Robins. *Phase noise in signal sources: theory and applications*, volume 9. IET, 1984.
81. David W Allan. Should the classical variance be used as a basic measure in standards metrology? *Instrumentation and Measurement, IEEE Transactions on*, 1001(2):646–654, 1987.
82. Enrico Rubiola. *Phase noise and frequency stability in oscillators*. Cambridge University Press, 2009.
83. Yu-Wei Lin, Seungbae Lee, Sheng-Shian Li, Yuan Xie, Zeying Ren, and CT-C Nguyen. Series-resonant vhf micromechanical resonator reference oscillators. *Solid-State Circuits, IEEE Journal of*, 39(12):2477–2491, 2004.
84. Ville Kaajakari, Jukka K Koskinen, and Tomi Mattila. Phase noise in capacitively coupled micromechanical oscillators. *Ultrasonics, Ferroelectrics and Frequency Control, IEEE Transactions on*, 52(12):2322–2331, 2005.
85. V Kaajakari, P Rantakari, JK Koskinen, T Mattila, J Kiihamaki, M Koskenvuori, I Tittonen, and A Oja. Low noise silicon micromechanical bulk acoustic wave oscillator. In *Ultrasonics Symposium, 2005 IEEE*, volume 2, pages 1299–1302. IEEE, 2005.
86. Arvind Raman, John Melcher, and Ryan Tung. Cantilever dynamics in atomic force microscopy. *Nano Today*, 3(1):20–27, 2008.
87. Jize Yan, Ashwin A Seshia, Kim L Phan, and Joost van Beek. Internal electrical and mechanical phase inversion for coupled resonator-array mems filters. *Sensors and Actuators A: Physical*, 158(1):18–29, 2010.
88. Siavash Pourkamali and Farrokh Ayazi. Electrically coupled mems bandpass filters: Part i: With coupling element. *Sensors and Actuators A: Physical*, 122(2):307–316, 2005.
89. Siavash Pourkamali and Farrokh Ayazi. Electrically coupled mems bandpass filters: Part ii. without coupling element. *Sensors and Actuators A: Physical*, 122(2):317–325, 2005.
90. CT-C Nguyen. Mems technology for timing and frequency control. *Ultrasonics, Ferroelectrics and Frequency Control, IEEE Transactions on*, 54(2):251–270, 2007.
91. Claudia Comi, Alberto Corigliano, Giacomo Langfelder, Antonio Longoni, Alessandro Tocchio, and Barbara Simoni. A resonant microaccelerometer with high sensitivity operating in an oscillating circuit. *Microelectromechanical Systems, Journal of*, 19(5):1140–1152, 2010.

92. KL Ekinci and ML Roukes. Nanoelectromechanical systems. *Review of scientific instruments*, 76(6):061101, 2005.
93. Ron Lifshitz and Michael L Roukes. Thermoelastic damping in micro-and nanomechanical systems. *Physical review B*, 61(8):5600, 2000.
94. Douglas M Photiadis and John A Judge. Attachment losses of high q oscillators. *Applied Physics Letters*, 85(3):482–484, 2004.
95. Kevin Y Yasumura, Timothy D Stowe, Eugene M Chow, Timothy Pfafman, Thomas W Kenny, Barry C Stipe, and Daniel Rugar. Quality factors in micron-and submicron-thick cantilevers. *Microelectromechanical Systems, Journal of*, 9(1):117–125, 2000.
96. Andrew N Cleland. *Foundations of nanomechanics: from solid-state theory to device applications*. Springer, 2002.
97. W Yi Jeong, Wan Y Shih, R Mutharasan, and Wei-Heng Shih. In situ cell detection using piezoelectric lead zirconate titanate-stainless steel cantilevers. *Journal of Applied Physics*, 93(1):619–625, 2002.
98. Frank M White and Isla Corfield. *Viscous fluid flow*, volume 2. McGraw-Hill New York, 1991.
99. Young-Ho Cho, Albert P Pisano, and Roger T Howe. Viscous damping model for laterally oscillating microstructures. *Microelectromechanical Systems, Journal of*, 3(2):81–87, 1994.
100. Minhang Bao. *Analysis and design principles of MEMS devices*. Elsevier, 2005.
101. Timo Veijola and Marek Turowski. Compact damping models for laterally moving microstructures with gas-rarefaction effects. *Microelectromechanical Systems, Journal of*, 10(2):263–273, 2001.
102. Wenjing Ye, Xin Wang, Werner Hemmert, Dennis Freeman, and Jacob White. Air damping in laterally oscillating microresonators: a numerical and experimental study. *Microelectromechanical Systems, Journal of*, 12(5):557–566, 2003.
103. Minhang Bao and Heng Yang. Squeeze film air damping in mems. *Sensors and Actuators A: Physical*, 136(1):3–27, 2007.
104. Suhas S Mohite, Venkata R Sonti, and Rudra Pratap. A compact squeeze-film model including inertia, compressibility, and rarefaction effects for perforated 3-d mems structures. *Microelectromechanical Systems, Journal of*, 17(3):709–723, 2008.
105. Giorgio De Pasquale, Timo Veijola, and Aurelio Somà. Modelling and validation of air damping in perforated gold and silicon mems plates. *Journal of Micromechanics and Microengineering*, 20(1):015010, 2010.
106. L Shao and M Palaniapan. Effect of etch holes on quality factor of bulk-mode micromechanical resonators. *Electronics Letters*, 44(15):938–940, 2008.
107. Cheng Tu and Joshua E-Y Lee. Increased dissipation from distributed etch holes in a lateral breathing mode silicon micromechanical resonator. *Applied Physics Letters*, 101(2):023504–023504, 2012.
108. Vladimir L Rabinovich, Raj K Gupta, and Stephen D Senturia. The effect of release-etch holes on the electromechanical behaviour of mems structures. In *Solid State Sensors and Actuators, 1997. TRANSDUCERS'97 Chicago., 1997 International Conference on*, volume 2, pages 1125–1128. IEEE, 1997.
109. Stein A Berggren, Dag Lukkassen, Annette Meidell, and Leon Simula. Some methods for calculating stiffness properties of periodic structures. *Applications of Mathematics*, 48(2):97–110, 2003.
110. Kyeong-Hoon Jeong and Marco Amabili. Bending vibration of perforated beams in contact with a liquid. *Journal of sound and vibration*, 298(1):404–419, 2006.
111. A-J Wang and DL McDowell. In-plane stiffness and yield strength of periodic metal honeycombs. *Journal of engineering materials and technology*, 126(2):137–156, 2004.
112. M Pedersen, W Olthuis, and P Bergveld. On the mechanical behaviour of thin perforated plates and their application in silicon condenser microphones. *Sensors and Actuators A: Physical*, 54(1):499–504, 1996.

113. Jize Yan and Ashwin A Seshia. Effects of etch holes in microelectromechanical resonators. In *Proc. the 8th Int. Conf. on Modeling and Simulation of Microsystems, Annaheim, USA*, 2005.
114. AL Herrera-May, PJ García-Ramírez, LA Aguilera-Cortés, H Plascencia-Mora, L García-González, E Manjarrez, M Narducci, and E Figueras. Analytical modeling for the bending resonant frequency of sensors based on micro and nanoresonators with complex structural geometry. *Sensors Journal, IEEE*, 11(6):1361–1374, 2011.
115. Y Civet, F Casset, JF Carpentier, and S Basrour. Numerical and analytical modelling of holed mems resonators. *Sensors and Actuators A: Physical*, 186:230–235, 2012.
116. Stephen Timoshenko. *Strength of materials*, volume 1. Van Nostrand, New York, second edition, 1940.
117. Matthew A Hopcroft, William D Nix, and Thomas W Kenny. What is the young's modulus of silicon? *Microelectromechanical Systems, Journal of*, 19(2):229–238, 2010.
118. Bruno Figeys, Roelof Jansen, Bart Nauwelaers, HAC Tilmans, and Xavier Rottenberg. Process tolerant design of baw resonators via hole engineering. In *Solid-State Sensors, Actuators and Microsystems (TRANSDUCERS & EUROSENSORS XXVII), 2013 Transducers & Eurosensors XXVII: The 17th International Conference on*, pages 2300–2303. IEEE, 2013.
119. X Rottenberg, R Jansen, V Cherman, A Witvrouw, HAC Tilmans, M Zanaty, A Khaled, and M Abbas. Meta-materials approach to sensitivity enhancement of mems baw resonant sensors. In *Sensors, 2013 IEEE*, pages 1–4. IEEE, 2013.
120. Raymond David Mindlin, Jiashi Yang, Raymond David Mindlin, and Raymond David Mindlin. *An introduction to the mathematical theory of vibrations of elastic plates*. World Scientific, 2006.
121. Lorna J Gibson and Michael F Ashby. *Cellular solids: structure and properties*. Cambridge university press, 1999.
122. Martin H Sadd. *Elasticity: theory, applications, and numerics*. Academic Press, 2009.
123. Manvir S Kushwaha, P Halevi, L Dobrzynski, and B Djafari-Rouhani. Acoustic band structure of periodic elastic composites. *Physical Review Letters*, 71(13):2022, 1993.
124. MS Kushwaha, P Halevi, G Martinez, L Dobrzynski, and B Djafari-Rouhani. Theory of acoustic band structure of periodic elastic composites. *Physical Review B*, 49(4):2313, 1994.
125. M Sigalas and EN Economou. Elastic and acoustic wave band structure. *Journal of Sound and Vibration*, 158(2):377–382, 1992.
126. M Sigalas and EN Economou. Band structure of elastic waves in two dimensional systems. *Solid state communications*, 86(3):141–143, 1993.
127. Degang Zhao, Wengang Wang, Zhengyou Liu, Jing Shi, and Weijia Wen. Peculiar transmission property of acoustic waves in a one-dimensional layered phononic crystal. *Physica B: Condensed Matter*, 390(1):159–166, 2007.
128. JO Vasseur, PA Deymier, B Chenni, B Djafari-Rouhani, L Dobrzynski, and D Prevost. Experimental and theoretical evidence for the existence of absolute acoustic band gaps in two-dimensional solid phononic crystals. *Physical Review Letters*, 86(14):3012, 2001.
129. FR Montero de Espinosa, E Jimenez, and M Torres. Ultrasonic band gap in a periodic two-dimensional composite. *Physical review letters*, 80(6):1208, 1998.
130. D Garcia-Pablos, M Sigalas, FR Montero De Espinosa, M Torres, M Kafesaki, and N Garcia. Theory and experiments on elastic band gaps. *Physical review letters*, 84(19):4349, 2000.
131. R Martinezsala, J Sancho, JV Sanchez, V Gómez, J Llinares, and F Meseguer. Sound-attenuation by sculpture. *nature*, 378(6554):241–241, 1995.
132. JV Sánchez-Pérez, D Caballero, R Martinez-Sala, C Rubio, J Sánchez-Dehesa, F Meseguer, J Llinares, and F Gálvez. Sound attenuation by a two-dimensional array of rigid cylinders. *Physical Review Letters*, 80(24):5325, 1998.
133. Fu-Li Hsiao, Abdelkrim Khelif, Hanane Moubchir, Abdelkrim Choujaa, Chii-Chang Chen, and Vincent Laude. Complete band gaps and deaf bands of triangular and honeycomb water-steel phononic crystals. *Journal of applied physics*, 101(4):044903, 2007.

134. Toyokatsu Miyashita. Sonic crystals and sonic wave-guides. *Measurement Science and Technology*, 16(5):R47, 2005.
135. RH Olsson Iii and I El-Kady. Microfabricated phononic crystal devices and applications. *Measurement Science and Technology*, 20(1):012002, 2009.
136. Tsung-Tsong Wu, Liang-Chen Wu, and Zi-Gui Huang. Frequency band-gap measurement of two-dimensional air/silicon phononic crystals using layered slanted finger interdigital transducers. *Journal of applied physics*, 97(9):094916, 2005.
137. Sarah Benchabane, Abdelkrim Khelif, J-Y Rauch, Laurent Robert, and Vincent Laude. Evidence for complete surface wave band gap in a piezoelectric phononic crystal. *Physical Review E*, 73(6):065601, 2006.
138. Saeed Mohammadi, Ali Asghar Eftekhar, Abdelkrim Khelif, William D Hunt, and Ali Adibi. Evidence of large high frequency complete phononic band gaps in silicon phononic crystal plates. *Applied Physics Letters*, 92(22):221905, 2008.
139. Roy H Olsson III, Ihab F El-Kady, Mehmet F Su, Melanie R Tuck, and James G Fleming. Microfabricated vhf acoustic crystals and waveguides. *Sensors and Actuators A: Physical*, 145:87–93, 2008.
140. Jin-Chen Hsu, Feng-Chia Hsu, and Pin Chang. Phononic crystal strips for engineering micromechanical resonators. In *SPIE OPTO*, pages 826912–826912. International Society for Optics and Photonics, 2012.
141. Feng-Chia Hsu, Jin-Chen Hsu, Tsun-Che Huang, Chin-Hung Wang, and Pin Chang. Reducing support loss in micromechanical ring resonators using phononic band-gap structures. *Journal of Physics D: Applied Physics*, 44(37):375101, 2011.
142. L Sorenson, JL Fu, and F Ayazi. One-dimensional linear acoustic bandgap structures for performance enhancement of aln-on-silicon micromechanical resonators. In *Solid-State Sensors, Actuators and Microsystems Conference (TRANSDUCERS), 2011 16th International*, pages 918–921. IEEE, 2011.
143. Duan Feng, Dehui Xu, Guoqiang Wu, Bin Xiong, and Yuelin Wang. Phononic crystal strip based anchors for reducing anchor loss of micromechanical resonators. *Journal of Applied Physics*, 115(2):024503, 2014.
144. Bongsang Kim, Janet Nguyen, Peggy J Clews, Charles M Reinke, Drew Goettler, Zayd C Leseman, Ihab El-Kady, and RH Olsson. Thermal conductivity manipulation in single crystal silicon via lithographycally defined phononic crystals. In *Micro Electro Mechanical Systems (MEMS), 2012 IEEE 25th International Conference on*, pages 176–179. IEEE, 2012.
145. Patrick E Hopkins, Charles M Reinke, Mehmet F Su, Roy H Olsson III, Eric A Shaner, Zayd C Leseman, Justin R Serrano, Leslie M Phinney, and Ihab El-Kady. Reduction in the thermal conductivity of single crystalline silicon by phononic crystal patterning. *Nano letters*, 11(1):107–112, 2010.
146. Saeed Mohammadi and Ali Adibi. On chip complex signal processing devices using coupled phononic crystal slab resonators and waveguides. *AIP Advances*, 1(4):041903, 2011.
147. Saeed Mohammadi and Ali Adibi. Waveguide-based phononic crystal micro/nanomechanical high-resonators. *Microelectromechanical Systems, Journal of*, 21(2):379–384, 2012.
148. M Ziaei-Moayyed, MF Su, C Reinke, IF El-Kady, and RH Olsson. Silicon carbide phononic crystal cavities for micromechanical resonators. In *Micro Electro Mechanical Systems (MEMS), 2011 IEEE 24th International Conference on*, pages 1377–1381. IEEE, 2011.
149. Nan Wang, JM-L Tsai, Fu-Li Hsiao, Bo Woon Soon, Dim-Lee Kwong, Moorthi Palaniapan, and Chengkuo Lee. Micromechanical resonators based on silicon two-dimensional phononic crystals of square lattice. *Microelectromechanical Systems, Journal of*, 21(4):801–810, 2012.
150. R Lucklum and J Li. Phononic crystals for liquid sensor applications. *Measurement Science and Technology*, 20(12):124014, 2009.
151. Ralf Lucklum, Manzhu Ke, and Mikhail Zubtsov. Two-dimensional phononic crystal sensor based on a cavity mode. *Sensors and Actuators B: Chemical*, 171:271–277, 2012.

152. Ralf Lucklum, Mikhail Zubtsov, and Manzhu Ke. Liquid sensor utilizing a regular phononic crystal with normal incidence of sound. *Ultrasonics, Ferroelectrics and Frequency Control, IEEE Transactions on*, 59(3):463–471, 2012.
153. Mikael Wilm, Sylvain Ballandras, Vincent Laude, and Thomas Pastureaud. A full 3d plane-wave-expansion model for 1-3 piezoelectric composite structures. *The Journal of the Acoustical Society of America*, 112(3):943–952, 2002.
154. MM Sigalas and N Garcıa. Theoretical study of three dimensional elastic band gaps with the finite-difference time-domain method. *Journal of Applied Physics*, 87(6):3122–3125, 2000.
155. Saeed Mohammadi. *Phononic Band Gap Micro/Nano-Mechanical Structures for Communications and Sensing Applications*. PhD thesis, Georgia Institute of Technology, august 2010.
156. Sophocles J Orfanidis. *Electromagnetic waves and antennas*. Rutgers University, 2002.